THESIS APPROVAL

GRADUATE SCHOOL, KASETSART UNIVERSITY

Master of Science (Chemistry)
DEGREE

Chemistry   Chemistry
FIELD   **DEPARTMENT**

TITLE: Preparation of $LaCoO_3$ Perovskite for CO Gas Sensor

NAME: Ms. Saengdoen Daungdaw

THIS THESIS HAS BEEN ACCEPTED BY

_____ **THESIS ADVISOR**
(Miss Pinsuda Viravathana, Ph.D.   )

_____ **THESIS CO-ADVISOR**
(Associate Professor Atchana Wongchaisuwat, M.S.   )

_____ **THESIS CO-ADVISOR**
(Mrs. Chutima Eamchotchawalit, Ph.D.   )

_____ **DEPARTMENT HEAD**
(Assistant Professor Noojaree Prasitpan, Ph.D.   )

APPROVED BY THE GRADUATE SCHOOL ON _____

_____ **DEAN**
(Associate Professor Gunjana Theeragool, D.Agr.)

THESIS

PREPARATION OF LaCoO$_3$ PEROVSKITE
FOR CO GAS SENSOR

SAENGDOEN DAUNGDAW

A Thesis Submitted in Partial Fulfillment of
the Requirements for the Degree of
Master of Science (Chemistry)
Graduate School, Kasetsart University
2009

Saengdoen Daungdaw 2009: Preparation of LaCoO$_3$ Perovskite for CO Gas Sensor. Master of Science (Chemistry), Major Field: Chemistry, Department of Chemistry. Thesis Advisor: Ms. Pinsuda Viravathana, Ph.D. 141 pages.

The LaCoO$_3$-ss (1:1, 1:5 (high Co), and 5:1 (high La)) perovskites were prepared by solid state reaction method. All LaCoO$_3$ samples were prepared and characterized by X-ray diffraction (XRD), X-ray absorption near-edge structure (XANES), BET surface area, and scanning electron microscopy (SEM). Their properties were compared with those of the samples prepared by co-precipitation (LaCoO$_3$-cp) and modified wet powder dispersion (LaCoO$_3$-wd) methods. The main crystalline phase of all prepared LaCoO$_3$ was a rhombohedral perovskite structure. The crystallite sizes of LaCoO$_3$-ss (1:1, high Co, and high La) at 850°C were 122, 42, and 73 nm and the crystallite sizes at 700°C of LaCoO$_3$-wd and LaCoO$_3$-cp were 28.5 and 28.2 nm, respectively. The surface areas were 1.6, 3.9, and 5.2 m^{2}g^{-1} for LaCoO$_3$-ss (1:1, high Co, and high La), respectively. From co-precipitation and modified wet powder dispersion methods, the surface areas were 11.8 and 11.7 m^{2}g^{-1}, respectively. From XANES spectra, the average Co oxidation state of the LaCoO$_3$-ss (1:1 and high La) could be $\approx$ 3 and the average oxidation state of LaCoO$_3$-ss (high Co) was from 2 to 8/3. Moreover, SEM images showed the difference in morphology which strongly depended on the preparation methods. At the voltages of 7.5 volts, corresponded to temperature of 133°C measured at the LaCoO$_3$ surface, the resistance of prepared LaCoO$_3$ was lowest (highest conductivity). The fabricated sensors had been tested as CO gas sensors with the CO concentration of 1.98-19.84%v/v, 0.39-99.2%v/v, and 0.006-0.039%v/v at 7.5 volts. The LaCoO$_3$-ss (1:1) sensor performed the highest CO sensing capability compared to LaCoO$_3$-cp and LaCoO$_3$-ss (high Co). The detection limits of LaCoO$_3$-ss (1:1) and LaCoO$_3$-cp on CO sensing were of 0.006% (60 ppm) for CO concentration with the sensitivity of 1.007 and 1.013, respectively.

Student's signature	Thesis Advisor's signature	_____/_____/_____

ACKNOWLEDGEMENTS

TABLE OF CONTENTS

Page

LIST OF TABLES

LIST OF FIGURES

LIST OF FIGURES (Continued)

LIST OF FIGURES (Continued)

Figure   **Page**

34   SEM image of LaCoO$_3$-wd particle calcined at 700°C
         (Prangsri-aroon 2008).   69

35   Diagram for LaCoO$_3$ CO sensing.   70

36   The resistances with time of the LaCoO$_3$-ss (1:1) at 850°C with
         0-7.5 volts applied.   71

37   The resistances with time of the LaCoO$_3$-ss (1:1) calcined at 700,
         800, 850 and 900°C with the applied voltage of 7.5 volts.   72

38   The resistance with time of LaCoO$_3$-ss (high Co) calcined at
         700, 800, 850 and 900°C with the applied voltage of 7.5 volts.   73

39   The resistance with time of LaCoO$_3$-ss (high La) calcined at 700,
         800, 850 and 900°C with the applied voltage of 7.5 volts.   75

40   The sensitivity (R/R$_0$) of LaCoO$_3$-ss (1:1) with time on exposing
         to CO concentrations of 1.98-19.84% v/v.   77

41   The sensitivity (R/R$_0$) of LaCoO$_3$-ss (high Co) with time on
         exposing to CO centrations of 1.98-19.84% v/v.   79

42   The sensitivity and the CO concentrations of LaCoO$_3$-ss (1:1 and
         high Co) to 19.84% v/v at 20s.   81

43   The sensitivity with the CO concentrations of LaCoO$_3$-ss (1:1)
         0.39- 99.20% v/v at 20s. The inset represented the enlargement of the
         sensitivity with the low CO concentrations
         of 0.39-3.96% v/v at 20s.   84

44   The sensitivity (R/R$_0$) of LaCoO$_3$-ss (1:1) with the 0.004-0.039 %
         v/v CO concentrations at 20s.   86

45   LaCoO$_3$-cp and LaCoO$_3$-wd resistance with time.   88

46   LaCoO$_3$-cp sensor response with time on exposing to CO
         concentration of 1.98-19.84% v/v.   89

LIST OF FIGURES (Continued)

LIST OF FIGURES (Continued)

LIST OF ABBREVIATIONS

Ω	=	Ohm
BDDT	=	Brunauer, Deming, Deming and Teller
BET	=	Brunauer-Emmett-Teller
DTA	=	Different thermal analysis
EDX	=	Energy dispersive x-ray spectroscopy
EXAFS	=	Extended x-ray absorption fine structure
FWHM	=	Full width at half maximum intensity
g	=	gram
HRTEM	=	High reaction transmission electron microscopy
JCPDS	=	Joint committee on powder diffraction standards
K	=	Kelvin
LRS	=	Laser raman spectroscopy
$M\Omega$	=	Mega ohm
M.W.	=	Molecular weight
POM	=	Partial oxidation of methane
ppm	=	Part per million
rpm	=	Round per minute
SEM	=	Scanning electron microscope
TEM	=	Transmission electron microscope
TG	=	Thermogravimetry
TM-XANES	=	Transmission mode x-ray absorption near-edge structure
XANES	=	X-ray absorption near-edge structure
XRD	=	X-ray diffraction

PREPARATION OF LaCoO$_3$ PEROVSKITE
FOR CO GAS SENSOR

INTRODUCTION

Although gas sensors have been developed for some applications fields, there are a variety of potential markets which will be substantiated for the newly innovated gas sensors. The materials design in innovating gas sensors is by introducing semiconductor gas sensors and solid electrolyte gas sensors as examples. In addition, the importance for further advancements of gas sensor technology attempts to make the sensor devices more intelligent and more quantitative, (Yamazoe, 2005).

Gas sensors are increasingly needed for industrial health and safety, environmental monitoring, and process control. The research into new sensors is underway; there are efforts to enhance the performance of traditional devices, such as resistive metal oxide sensors, through nanoengineering. Metal oxide materials for gas sensors have been used for several decades for low-cost detection of combustible and toxic gases. The sensitivity, selectivity, and stability have limited their use, often in favor of more expensive approaches. Nanomaterials provide the opportunity to dramatically increase the response of these materials, as their performance is directly related to exposed surface volume (Hooker, 2002).

The mechanism for gas sensor in these materials is based, on reactions that occur at the sensor surface, resulting in a change in the concentration of adsorbed oxygen. Oxygen ions adsorb onto the material's surface, removing electrons from the bulk and creating a potential barrier that limits electron movement and conductivity. When reactive gases combine with this oxygen, the height of the barrier is reduced, increasing conductivity. This change in conductivity is directly related to the amount of a specific gas present in the environment, resulting in a quantitative determination

of gas presence and concentration. These gas-sensor reactions typically occur at elevated temperatures (150-600°C), requiring the sensors to be internally heated for maximum response. The operating temperature must be optimized for both the sensor material and the gas being detected (Hooker, 2002).

Gas sensor has been used in several fields such as in industrial processes, the emission control for automobiles, and gas leakage detection at home, etc. The research into gas sensors based on semiconducting metal oxides has made several kinds of gas such as CO, H_2, NH_3, alcohol, hydrocarbons, NO_2, SO_2, and CO_2 (Kida, 2008).

Carbon monoxide (CO) is an odorless, colorless and toxic gas. Because it is impossible to see, taste or smell the toxic fumes, CO can kill people before ones are aware it is in their home. At lower levels, CO causes mild effects that are often mistaken for the flu. These symptoms include headaches, dizziness, disorientation, nausea, and fatigue. The effects of CO exposure can vary greatly from person to person depending on age, health, and the concentration of exposure. Carbon monoxide is found in the following, gas space heaters; leaking chimneys and furnaces; gas water heaters, wood stoves, and fireplaces; gas stoves; generators and other gasoline powered equipment; automobile exhaust; and tobacco smoke. Incomplete oxidation during combustion in gas ranges and unvented gas or kerosene heaters may cause high concentrations of CO in indoor air. Worn or poorly adjusted and maintained combustion devices can be significant sources, or if the flue is improperly sized, blocked, disconnected, or is leaking. Truck, or bus exhaust from attached garages, nearby roads, or parking areas can also be a source. Due to the importance of CO detection for health and safety, this studies are focused on CO sensing.

The sensing materials, the metal oxide semiconductors as SnO_2, ZnO, In_2O_3, WO_3, TiO_2, α-Fe_2O_3, HfO_2, $BaSnO_3$, $LaMnO_3$, $LaNiO_3$, and $LaSrCoO_4$ have been studied for response of CO gas sensor. $LaCoO_3$ is a native p-type semiconductor,

having high electrical conductivity and exhibiting good oxidation-reduction characteristics at high temperature. $LaCoO_3$ can be prepared by solid-state reaction, sol-gel, co-precipitation, the decomposition of precipitate precursors, polymeric gel and solution combustion method. The applications of $LaCoO_3$ materials are for catalysts, oxygen sensor, gas sensor in automobiles, electrolyte in solid oxide fuel cell (SOFC) and oxygen separation membranes (Haung, 2007). Since $LaCoO_3$ has a variety of uses and good matched properties for sensing, the studies choose $LaCoO_3$ as sensing material.

In this research, $LaCoO_3$ was prepared by solid-state reaction; the optimum conditions for $LaCoO_3$ synthesis were investigated and the characterization was performed. The prepared perovskite was fabricated as a gas sensor and the response of the perovskite to CO gas was studied. Moreover, the sensing capability of $LaCoO_3$ obtained from the other two methods of co-precipitation and modified wet powder dispersion was also presented.

OBJECTIVES

1. To synthesize and characterize the $LaCoO_3$ from the solid state reaction method.

2. To study the CO gas sensing response of $LaCoO_3$.

3. To compare the sensing capability of the $LaCoO_3$ perovskites from the solid state reaction, co-precipitation, and modified wet powder dispersion methods.

LITERATURE REVIEW

1. Gas sensor

Currently, several types of gas sensor had been created for the necessities of modern living reflected in industry, research, health and safety, and care for the environment. These needs could be simply classified into: quality, safety, efficiency and environment. The physical and chemical properties of gas sensors using various methods and technologies were studied for utilization in gas response. (Kocache, 1994).

1.1 Semiconductor gas sensor

In a semiconductor gas sensor, there were two electrodes buried into a semiconductor material. The presence of gas changed the material resistance. The change in resistance, directly to the gas concentration, was measured through sensor corresponding electronic circuitry. The sensor was kept at a specific operating temperature by applying "heater" to it. The selection of heater voltage was critical to the response characteristics of the sensor. Toxic and explosive gases could be detected by varying this voltage and by using different materials and processing techniques. Sensors was fabricated to be sensitive to one gas or group of gases and less sensitive to others. The advantage of semiconductor gas sensor was its long life operation.

The gas sensors worked on the principle that the electrical conductivity of a semiconductor material chances when it was exposed to a gas. The gas adsorbed on the surface of the material and surface conductivity, or chances the "defect chemistry" of the material and the resistance was changed. Tin oxide was probably the most used metal oxide material. The selection was dependent on the gas of interest. A heater coil and detection coil were buried in a sinter of mostly tin oxide. The heater coil was

energized and the change in resistance between the heater and the detection coil is monitored. Sensors of this type were mostly used as alarms at the home for gas leaks. They were also used as personal or area alarms. They were simple, low cost and detection limit for toxic or flammable gases in air. A great deal of work had been going on investigating many families of metal oxides, organic semiconductors and polymers for their gas sensitive properties. There was also work being done on the sensor itself such as the inclusion of heaters and use of thick films. Another rate was the use of a number of sensors each mainly sensitive to a different gas, to create an "electronic nose" in conjunction with neural network analysis; this gave to a qualitative rather than quantitative type of response (Kocache, 1994).

Table 1 Types of gas sensor.

Type	Classification	Materials	Gases
Gas adsorption	Semiconductor	SnO_2, ZnO	LPG, CO
		y-Fe_2O_3, V_2O_5	Alcohol
		TiO_2, CoO, MgO-CoO	O_2
	Surface potential	Pd-TiO_2, Ag_2O	H_2, CO
Gas reaction	Catalytic combustion	Pt wire, Pt, Pd+Al_2O_3	Flamable gases
	Potentisotatic	Gas electrode	CO, NO, NO_2, S_2
	Galvanic cell	Nobie cathode (Pt, Au)& base anode (Pb)	O_2
Selective membrane	Solid electrolyte	ZrO_2-CaO, ThO_2-Y_2O_3, $PbCl_2$, $PbBr_2$, K_2SO_4	O_2

Elisabetta *et al*., (2000) studied solid-state ceramic NO_x sensors based on interfacing an ionic conductor (NASICON) with semiconducting oxides. The NASICON pellets were prepared and sintered at 1270°C in air. A uniform Au/Pd coating, permeable to oxygen but not to NOx, was sputtered for 40 min on the sensor external surface to allow the exposure of both electrodes to the gas atmosphere without using reference air. Energy-dispersive spectroscopy (EDS) was used to evaluate the chemical composition of the Au-Pd layer before and after the sensing tests. Sodalite powder as an auxiliary phase was tightly packed into the NASICON thimbles with a Pt lead, as the electrical contact. $LaFeO_3$, $SmFeO_3$, $NdFeO_3$, and $LaCoO_3$ powders prepared by the thermal decomposition of the corresponding hexacyanocomplexes, were also used in the electrochemical cells. The microstructure of the materials tested was evaluated using scanning electron microscopy (SEM). The NO_2 sensing properties of the prototype sensors were investigated at controlled temperature (in the range 300-600°C) by measuring the electromotive force (EMF) at different NO_2 concentrations (in the range of 2-2000 ppm in air). Some measurements were done at various NO concentrations diluted with Ar. The results showed a promising NO_2 sensing performance when ferrites were used. The perovskite-type oxides were much used as auxiliary phase than sodalite because the stability of the electrochemical sensor performances was increased.

Brosha *et al*., (2000) had showed a new type of mixed potential, zirconia-based sensor. For sensor, dense and thin films of either La–Sr–Co–O or La–Co–O perovskite transition metal oxide vs. an Au counter electrode were used to generate an EMF that was proportional to the concentration of oxidizable gas species, carbon monoxide (CO), C_3H_6, and C_3H_8, in a gas stream containing oxygen. The instruments reported in this work were tested at 600°C and 700°C and in gas mixtures containing 0.1% to 20% O_2 concentrations. The material for sensors showed an improvement in operating temperature and level stability at high temperatures compared to Au–zirconia–Pt mixed potential devices reported in the literature. For Au–zirconia–Pt devices, the response behavior reproducibility was dependent on the Au morphology, which could vary significantly between samples under same thermal histories. The

changing in Au morphology on both the Au counter electrode and the Au current collector on the metal oxide electrode were responsible for sensor aging and changed in device response over time. No change in the crystal structure of the perovskite thin film could be seen from XRD. The Au counter electrode was replaced with a second metal oxide thin film, doped $LaMnO_3$, and the operation of a mixed potential sensor based on dual metal oxide electrodes was exhibited.

1.2 Carbon monoxide (CO) gas sensor

There were attempts to propose the reaction mechanism on the surface. From the well known Langmuir-Hinshelwood mechanism, the reactant species CO and oxygen would be adsorbed on the surface to facilitate the reaction. Usually, O_2 adsorbs dissociatively on the surface as atomic oxygen species and these atomic oxygen species were more reactive than molecular species. It was well known that CO was a reducing agent and reacts with adsorbed oxygen to form CO_2. The reaction rate would be controlled by the rate of CO_2 desorption from the surface. The simplified reaction scheme could be written as below

$$S_{(s)} + \frac{1}{2} O_{2\,(g)} \rightarrow S \ldots \frac{1}{2} O_{2\,(ad)} \tag{1}$$

$$S \ldots \frac{1}{2} O_{2\,(ad)} \rightarrow S \ldots O^-_{(ad)} \tag{2}$$

$$S_{(s')} + CO_{(g)} \rightarrow S \ldots CO^+_{(ad)} \tag{3}$$

$$S \ldots O^-_{(ad)} + S \ldots CO^+_{(ad)} \rightarrow S \ldots CO_{2\,(ad)} + S_{(s)} \tag{4}$$

$$S \ldots CO_{2\,(ad)} \rightarrow S_{(s')} + CO_{2\,(g)} \tag{5}$$
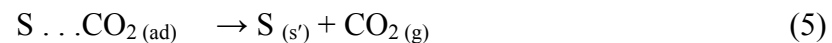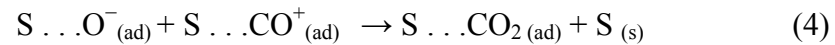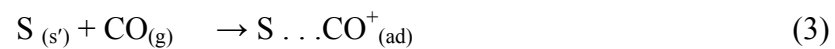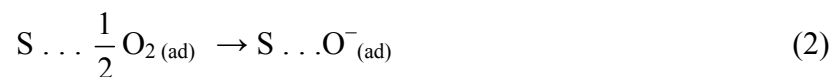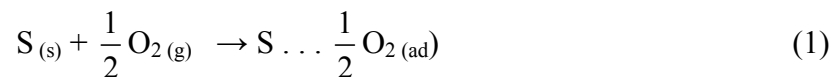
Here, (s) and (s') represent active sites on the surface for oxygen and CO adsorption, respectively, (g) and (ad) were gas and adsorbed form. The active sites (s) and (s') may or may not be the same, depending on the type of materials. When the sensor response measurement was carried out at higher temperatures, the adsorbed species of oxygen and CO reacts on the surface which requires low

activation energy. This was because the adsorption was exothermic process and the reaction activation energy becomes lowered. The reaction was possible at lower temperatures. Another mechanism was also possible as CO being a reducing gas and it had a tendency to take lattice oxygen from the surface. First, CO had to adsorb on the surface and then it will react with the lattice oxygen to form CO_2. The reaction scheme could be written as follows:

$$M-O_{(s)} + CO_{(g)} \rightarrow M-O...CO^+_{(ad)} \tag{6}$$

$$M-O...CO^+_{(ad)} \rightarrow M^+...O\,CO_{(ad)} \tag{7}$$

$$M^+...O\,CO_{(ad)} \rightarrow M-[\ ]^+ + CO_{2(g)} \tag{8}$$

$$M-[\ ]^+ + \frac{1}{2}O_{2(g)} \rightarrow M-[\ ]^+...O^-_{(ad)} \tag{9}$$

$$M-[\ ]^+...O^-_{(ad)} \rightarrow M-O_{(s)} \tag{10}$$
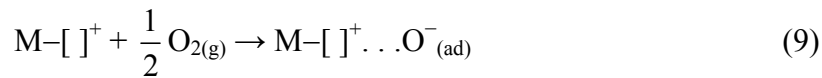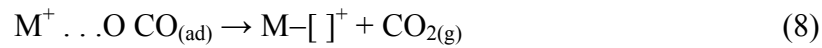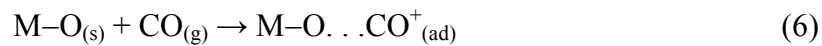
Here, (s) represents an active site on the metal oxide surface, $M-[\ ]^+$ as a reduced metal oxide site on the surface, (g) and (ad) were gas and adsorbed form species. Eq. (6) represents the adsorption of CO on the active site of the metal oxide and it would react with surface lattice oxygen (Eq. (7)). Adsorbed CO_2 would get desorbed as shown in Eq. (8) and reduced active site will get regenerated by taking oxygen from air as shown in Eqs. (9) and (10) to continue the adsorption and desorption cycle. The rate of the reaction was controlled by active site reduction process (Salker., 2005).

1.3 A low-level carbon monoxide sensor

Figure 1 showed the effect on the human body of several levels of carbon monoxide in the atmosphere. When carbon monoxide was breathed into the body, it was taken up by blood in preference to oxygen, forming carboxylhemoglobin. This causes progressively more severe symptoms as its concentration increases, causing to death. The early symptoms were not often recognized by the sufferer, so

rendering the danger even greater. Below 10% carboxylhemoglobin, the physiological effect was negligible, and this is shown by the curve "I" in Figure 1. The time of exposure was also a factor. For example, 10% carboxylhemoglobin level in the blood of an average adult was touched when exposing at 400 ppm for 15 minutes. Hence, a monitor which alarms within 15 minutes at 400 ppm can stimulate personnel department long before any danger was happened.
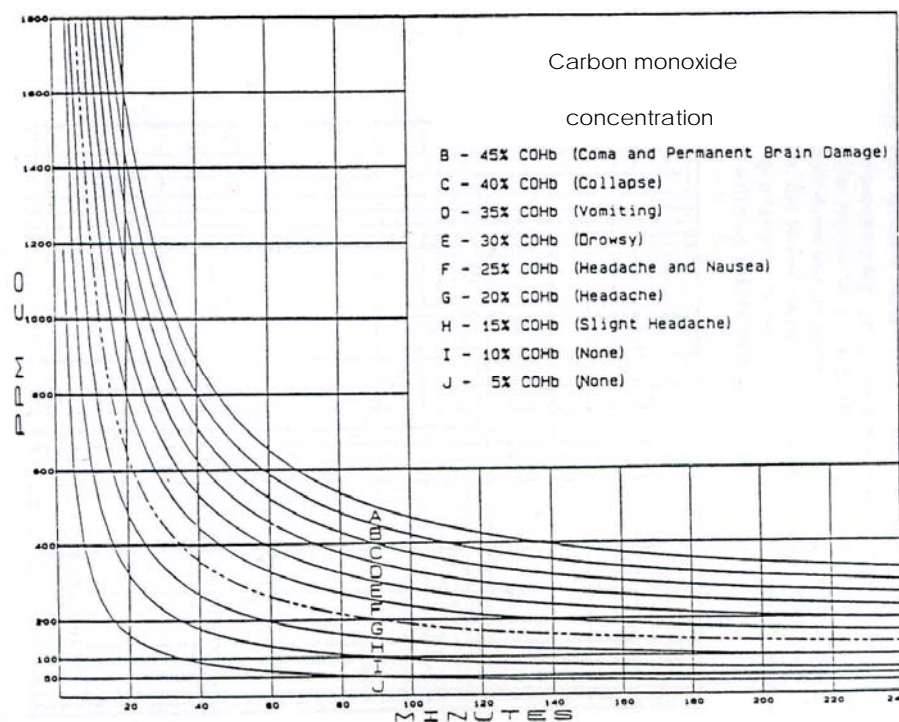
Figure 1 The relationship between atmospheric carbon monoxide concentration and exposure time leading to carboxylhemoglobin (COHb) concentration in blood.

Source: Adapted from Ihokura (1994)

Salker *et al.*, (2005) developed perovskite based $LaCoO_3$ as a thermal and toxic gas sensor such as carbon monoxide (CO). Metal oxides such as In_2O_3, Bi_2O_3 and PdO were prepared with 2% by weight of metal in $LaCoO_3$. The results showed that $LaCoO_3$-PdO gave higher sensing response than the others. These devices had

been tested as CO gas sensors in the CO concentration range of 10-40 ppm at temperatures between 150 and 300°C and showed good sensor response as well as good recovery. $LaCoO_3$-PdO gave high CO sensor response but reduced drastically in the thermal sensing property.

Ajami *et al*., (2006) used $LaCoO_3$ perovskite as an active filter to control the sensitivity of the Pt/SnO_2 sensor to CO and C_2H_5OH. By sol–gel method, SnO_2 fine powder was prepared using hexachloroplatinic acid to get 1.0 wt% Pt on SnO_2. $LaCoO_3$ perovskite fine powder was prepared by citrate method using nitrate precursors of La and Co. $LaCoO_3$ was an effective catalyst for oxidation of both carbon monoxide and ethanol at temperatures lower than 250°C. The catalyst did not convert methane at temperature as high as 400°C. The perovskite filter eliminated the sensitivity of the sensor to CO and C_2H_5OH, making the sensor highly selective to methane in the presence of CO and ethanol in air.

LaCoO$_3$ has a perovskite-type structure, with general formula of ABO$_3$ as shown in Figure 2, which presents the large cation A in dodecahedral co-ordination and the small cation B in octahedral co-ordination (Well, 1995). The transition metal ion B has several oxidation states that can be reduced and reoxidized.
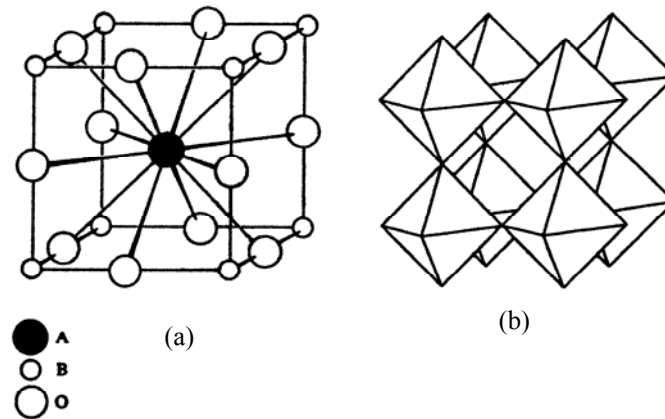
Figure 2 Bulk structure of perovskite. (a) atomic positions of the unit cell and (b) structure representing BO$_6$ octahedral.

Source: Adapted from Well (1995)

A stoichiometric ABO$_3$ compounds, combination of A^{n+} and B^{m+}, are given by n+m = 6, such as LaCoO$_3$, CaTiO$_3$, LaMnO$_3$, etc. The possible combination of A and B ions are controlled by the requirement that in the oxide framework the radii A and B ions should be more than 0.90 Å and 0.51 Å, respectively (Voorhoeve, 1977). In addition the perovskite is formed if the tolerance, t , is in the range of 0.8-1.0, $t = \dfrac{(R_A + R_0)}{\sqrt{2}(R_B + R_0)}$, where R$_A$, R$_B$ and R$_0$ are the ionic radii for A, B, and O, respectively. For example, the radii of La^{3+}, Co^{3+} and O^{2-} are 1.32, 0.61, and 1.40 Å, respectively, therefore the tolerance of LaCoO$_3$ is 0.96 corresponded to perovskite structure (Tejuca and Fierro, 1993).
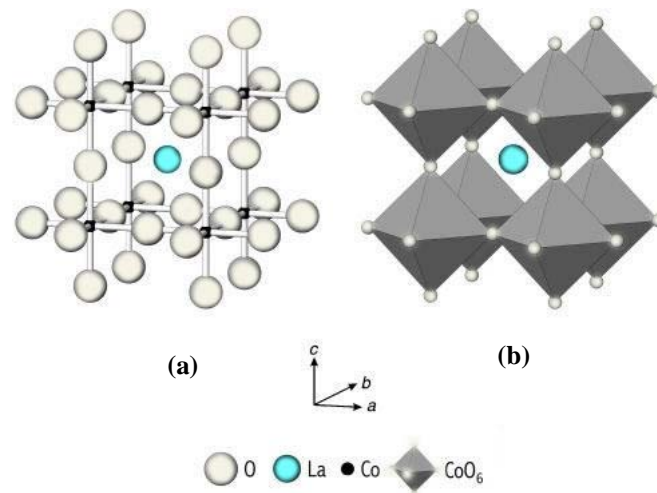
Figure 3 A crystal structure of $LaCoO_3$ (a) atomic positions of the unit cell and (b) a structure depicting CoO_6 corner-sharing octahedral, with the cations A occupying the central interstice, and the cations B residing in the centre of the octahedral.

Source: Adapted from Read Mark *et al*. (2002)

The ideal cubic perovskite structure appears in a few case for t-valve very close to unity and at high temperature (Peña and Fierro, 2001). In most case, different distortions of perovskite structure appear as shown in Table 2. The distorted structure may exist at low temperature but it transforms to the cubic structure at high temperature. This transition may occur in several steps through intermediate distorted phases. For example, the structure of $BaTiO_3$ is orthorhombic in temperature range of 193-268 K, it is tetragonal in temperature range of 268-393 K and it transforms to cubic at 1733 K (Well, 1995).

Table 2 Compounds with the perovskite type of structure.

Ideal structure	Perovskite
Ideal cubic structure	$SrTiO_3$, $SrZrO_3$, $SrHfO_3$, $SrSnO_3$, $SrFeO_3$, $BaZrO_3$, $BaHfO_3$, $BaSnO_3$, $EuTiO_3$, $LaMnO_3$
At least one form with distorted small cell (a ≈ 4 Å)	$BaTiO_3$ (T, C, O, R)
Cubic (C)	$KNbO_3$ (T, C, O, R)
Tetragonal (T)	$KTaO_3$ (C)
Orthorhombic (O)	$RbTaO_3$ (C, T)
Rhombohedral (R)	$PbTiO_3$, $LaCoO_3$ (C, T)
Distorted multiple cells	$CaTiO_3$, $GdFeO_3$, $NaNbO_3$, $PbHfO_3$, $LaCrO_3$

Source: Adapted from Wells (1995)

2. Preparation of perovskite-type oxides

2.1 Solid state reaction

Solid state reaction, namely ceramic process in which both starting materials and products were solid, offers convenient methods to prepare several industrial gas sensors. This method used the starting materials such as metal-carbonate, hydroxide and oxides, instead of starting with the individual components (Smart and Moor, 1995). It may be advisable to begin with prereacted powders. The prereacted phases facilitate initial homogeneity leading to reduce diffusion paths during the formation of products. Huang *et al*., (2007) prepared $LaCoO_3$ by reactive grinding solid-solid solution which gave smaller particle size as well as higher specific surface area than one prepared by citrate method. $LaCoO_3$ prepared by

reactive grinding showed a better stability of perovskite structure under a reducing atmosphere.

Kaliaguine *et al*., (2001) prepared $LaCoO_3$ and $LaCoFeO_3$ from component oxides using mechanochemical synthesis, by a new method of preparation designated as reactive grinding. Additives were added during grinding; the perovskites generated by this process were of unprecedently high specific surface area (>100 m^2/g) and their surface chemical properties were of particular interest.

Yao *et al*., (2000) had reported that the methods for forming films from aqueous solutions at ambient temperature and pressure were advantageous because no vacuum, no high temperature and no expensive devices were needed and substrates even with wide areas and complicated shapes were available. Solid solutions of (La,Sr) MeO (Me = Cr, Mn, Fe, Co) were appropriate materials for solid oxide fuel cells and high-temperature steam electrolyzers. (La,Sr)MeO_3 solid solutions prepared by solid state reaction were dissolved in hydrofluoric acid and the solutions of fluorocomplexes were obtained. Boric acid was added to the solution, the fluoride ions were used in the formation of BF^{4+}, and then the fluorocomplexes were hydrolyzed to (La,Sr)MeO_3 leading to the increases of fluoride ions. The high crystallinity of the solid solutions was showed by sharp and strong X-ray diffraction peaks. The particles of (La,Sr)MeO_3 solid solutions were observed on the substrates by scanning electron microscope.

Ito *et al*., (2004) prepared two different processes for synthesizing fine $LaCoO_3$ powder. One was a direct synthesis process, which was to grind a mixture of La_2O_3 and Co_2O_3 powders using a high-energy mill. Grinding causes mechanical reaction between the two compounds, leading to synthesize $LaCoO_3$ and the reaction was facilitated with an increase in milling time. $LaCoO_3$ agglomerates giving its specific surface area of about 3.5 m^2/g. Another process was composed of three steps: the first step was to grind a mixture of $LaCl_3$, $CoCl_2$ and NaOH, stimulating a solid-state reaction to form $La(OH)_3$, $Co(OH)_2$ and NaCl. The second step was to calcine at

873 K to change the hydroxides into complex oxide ($LaCoO_3$), and the final step was to wash out NaCl from the heated mixture. The product forms agglomerates, and its specific surface area was about 10 m^2/g. It was concluded that the indirect synthesis process was superior to the direct process $LaCoO_3$ powder.

Ivanova *et al*., (2007) suggested two methods for the preparation of $LaCoO_3$. The $LaCoO_3$ prepared by freeze-drying the solution and by a solid state reaction. For assignment of the electron paramagnetic resonance spectroscopy EPR signals, $La_{1-x}Sr_xCoO_3$ samples were used as EPR references. The $LaCoO_3$ oxides prepared from citrates and by a solid state reaction showed the difference in respect of the mean oxidation state of the cobalt ions, the specific surface area and the particle morphology. EPR spectroscopy showed for $LaCoO_3$ ferromagnetic Co^{3+} and Co^{4+} coupled ions. For $LaCoO_3$ samples acquired by a solid state reaction, EPR allowed to detect Co_3O_4 impurities.

The milling had shown to be an important step of preparation. Rougier *et al*., (2002) investigated the influence of grinding on the properties of $La_{0.8}Sr_{0.2}MnO_{3\pm\lambda}$ perovskite. The samples prepared by solid state reaction and by the Pechini method. The two methods were followed by a ball-milling. The XRD pattern showed increasing grinding time, the degree of lattice was increased and the crystallite size was decreased. This phenomenon tended to the sol-gel process rather than the ceramic process. BET surface area increased in the process sample from 1 to 6 m^2/g for ungrounded one and 5 h for grounded one at 1273 K, respectively. The decrease in surface area of the sol-gel process might be resulted from the agglomeration of small particles that are formed when the morphology was broken. Therefore, milling was a good step for specific method.

Zhang and Saito.,(2000) synthesized $LaMnO_3$ perovskite powders by milling the mixture of La_2O_3 and Mn_2O_3 powder using a high energy ball mill at room temperature. The planetary mill was used to grind the starting mixtures at

approximately 700 rpm. The LaMnO$_3$ powder was a form of aggregates composing of the fine grains with less than 100 nm in size as investigated by SEM. The sample surface area was approximately 10 m^2/g.

2.2 Co-precipitation method

The preparation of mixed metal by co-precipitation was technically important because this technique can be used for simultaneous precipitation of more than one component.
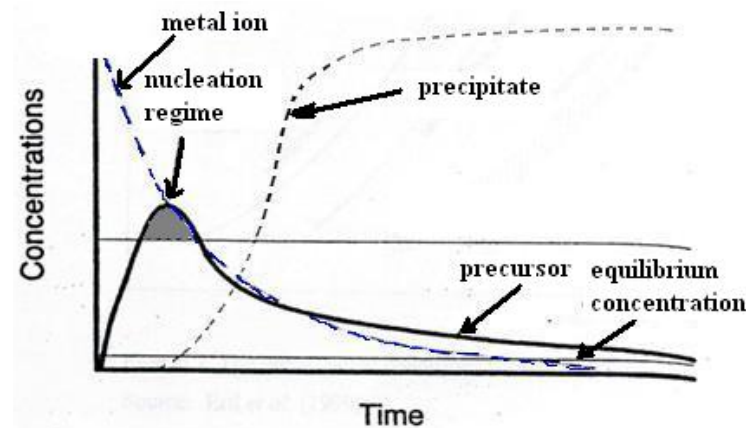
Figure 4 The formation of a solid product from solution.

Source: Adapted from Ertl *et al*. (1999)

The formation of a solid from solution could be explained by Figure 4. Ther are two main steps in precipitation: nucleation and growth. The metal ions in solution could be produced from precursors by hydrolysis or raising the pH. Only if the precursor concentration exceeds a critical threshold, a nucleus would be formed and the precipitation begins. New nuclei were only formed in the shaded area. The nucleus was smallest solid-phase aggregate of atoms, molecules or ions, and the process was called nucleation. The concentration of precursor species falls below the

critical concentration due to consumption of precursors by nucleation or by the growth process, the latter was preferred. The size of particles resulting from a precipitation process would be dependent on the area of the shaded section between the nucleation curve and nucleation threshold. The larger the area, the more particles nucleate and the smaller the resulting particles formed Ertl *et al*, (1999).

The homogeneity was possible to increase by taking advantage of the difference of the form of nucleation and growth of precipitated crystallites. According to the conditions, this growth step was mainly controlled by interface or diffusion phenomena. The first case generally corresponds to the formation of complicated solid structures. The second was more common in the precipitation processes used in catalyst preparation. Only more general statements could be given Ertl *et al*, (1999).

For nucleation:

- The higher the supersaturation was the higher will be the
nucleation rate;
- Any interface may play the role of a heterogeneous nucleus
by lowering the surface free-energy of the new phase, and thus increase the rate of nucleation;
- In general, higher temperatures lower the nucleation rate by
increasing the critical size of the nuclei-upper left boundary of the homogeneous nucleation band reflects this trend.

For growth:

- The higher the supersaturation was the higher growth rate, but it is rapidly limited by diffusion processes;

- Increasing of temperature, the diffusion rates was enhanced and

the higher would be the growth rate of the new phase.

Combining above, some general rules for obtaining a fine precipitation could be formulated:

- A vigorous stirring of the solution while adding the precipitant was beneficial in two ways: first, each elementary volume of solution reaches rapidly the highest degree of supersaturation; second, it comes into contact several times with the agitator and the walls of vessel, thereby promoting heterogeneous nucleation also.

- A rapid addition of the precipitating agent ensures a rapid reaching of the highest degree of supersaturation in the whole volume of the solution, hence a maximum nucleation rate was obtained. For the same reason, the best precipitating agent is the one giving the precipitate with the lowest solubility product.

- Although the situation may be very different from case to case, precipitation is often advantageously made at the lowest practical temperature, as this often favors nucleation over growth.

Citrate precursor was investigated by Zhang *et al*., (1987). The decomposition mechanism of these precursors was studied during the course of producing $LaCo_{0.4}Fe_{0.6}O_3$. By using thermogravimetry (TG), X-ray diffraction (XRD) and infrared (IR), it was found that citrate precursors undergo several decomposition steps before the perovskite structure was obtained. These steps correspond to the breakup of the citrate complexes, and the elimination of residual CO_3^{2-} and NO_3^- ions. The perovskite framework was detected by IR but was not observable by XRD, indicating that the perovskite was still lacking of extended crystallinity. When the temperature was raised to 823 or 873 K, the diffractions due to perovskite were observed. The calcination temperature of citrate precursors was about 473 to 573 K lower than the acetate preparation for the same compositions. The resulting surface areas of both preparations were measured. Because of the lower

calcination temperature, citrate preparations had a surface area increased by a factor between 3 and 7. It was proposed that the citrate complexes at the precursor stage have localized the metal ions more effectively, resulting in a more homogeneous dispersion at a lower calcination temperature. Spinicci *et al.*, (2001) prepared the $LaMO_3$ (M = Mn, Fe, Co) by the citrate precursors at 800°C. The catalytic behavior was studied in the hexane total oxidation. The activity scale was put in the order of $LaFeO_3 > LaCoO_3 > LaMnO_3$. The three $LaMO_3$ catalysts were single phase with rhombohedral structure. Specific surface values were 22, 15, and 3 m^2g^{-1} for $LaMnO_3$, $LaCoO_3$, and $LaFeO_3$, respectively. Barbero *et al.*, (2006) studied the $La_{1-x}Ca_xFeO_3$ as catalysts for oxidation of volatile organic compounds. The $La_{1-x}Ca_xFeO_3$ was prepared by the citrate method. The catalysts were single perovskite phases with a slight surface enrichment in lanthanum and calcium.

Natile *et al.*, (2007) studied the effect of synthesis conditions on properties and reactivity of $LaCoO_3$. Two nanostructured bulk $LaCoO_3$ were prepared by co-precipitation and with the citrate gel method and compared with the two nanocomposites obtained from depositing, by wet impregnation of cobalt oxide on the La_2O_3 surface. XRD patterns showed that only the citrate gel method provides a single phase $LaCoO_3$ powder having a rhombohedral perovskite structure. Hexagonal lanthanum hydroxide phase was also evident in the sample obtained by co-precipitation and in the nanocomposite with $[Co/La]_{nominal} = 1.0$. Perovskite phase does not form when the amount of cobalt is too low ($[Co/La]_{nominal} = 0.055$).

Alifanti *et al.*, (2007) prepared the $LaCoO_3$ perovskites with 10 and 20 wt% by wet impregnation of $Ce_{1-x}Zr_xO_2$ (x = 0-0.3) supports with a solution prepared from La and Co nitrates, and citric acid. Supports were also prepared using the ''citrate method''. All materials were calcined at 700°C for 6 h and investigated by BET measurement, XRD and XPS. XRD patterns and XPS measurements showed the formation of a pure perovskite phase, preferentially accumulated at the outer surface. These materials were examined in benzene and toluene oxidation in the temperature range of 100-500°C. All catalysts showed a lower T_{50} than the corresponding Ce_{1-x}

Zr_xO_2 supports. Twenty weight percent $LaCoO_3$ catalysts presented lower T_{50} than bulk $LaCoO_3$. The reaction rates per mass unit of perovskite calculated at $300^\circ C$, two facts could be notified as (i) the activity order was more than 10 times higher for toluene and (ii) the reverse variation with the loading as a function of the reactant, a better activity being observed for low loadings in the case of benzene. For the same loading, the support composition showed drastically the oxidative abilities of $LaCoO_3$ by the surface area and the oxygen mobility.

Taguchi *et al.*, (2002) prepared $LaCoO_3$ by citrate method. Gel was preparation by adding citric acid into the aqueous solution of $La(NO_3)_3.6H_2O$ and $Co(NO_3)_2.6H_2O$. The infrared spectrum showed that the gel prepared with 0.007 mol of citric acid was the mixture of $LaCo(C_6H_5O_7)(NO_3)_3$, lanthanum nitrate and cobalt nitrate while the gel prepared with 0.011 mol of citric acid was $LaCo(C_6H_5O_7)_2$. $LaCoO_3$ was formed by firing the gel above $600^\circ C$. The $LaCoO_3$ surface was characterized by XPS and with respect to the catalytic of CO oxidation.

2.3 Modified wet powder dispersion

In the preparation of perovskite, there were two precursors, one was powder which was insoluble or scarcely soluble in water or alcohol (fine particle of oxide having submicron order particle size), the other was aqueous solution or alcoholic solution (including alkoxide solution). Mixing these precursors introduced dispersing liquid for powder with precipitate forming liquid (e.g. NH_3) or mixing successively in multistage to prepare intimate precipitate. The precipitate was calcined at $400\text{-}1,300^\circ C$ after drying (Shinichi *et al.*, 1986).

2.4 Other methods

2.4.1 Thermal treatment by combustion

A novel combustion process for the synthesis of $YBa_2Cu_3O_7$ superconductor involved ignition of a metal nitrates organic salts mixture and resulted in an intimate mixture of partially reaction oxides (Tejuca and Fierro, 1993). Another modification used a nitrate-urea mixture. The other combustion with NH_4NO_3 and urea was followed by subsequent heat treatment and oxygenation. This produced a single phase superconducting $YBa_2Cu_3O_7$ powder (Varma *et al.*, 1990).

Pokhrel *et al.*, (2007) prepared $LaCr_{1-x}Ti_xO_3$ ($x \leq 0.4$) by citrate combustion method. XRD patterns showed an orthorhombic structure for all the products. From SEM the sensors heated at $850^{\circ}C$ showed the isolate grain size on the surface in the range of 200–340 nm, which was further evidenced by the range of 210–333 nm calculated by Scherrer equation. The ac impedance measurement was a tool to study the conduction process in the temperature range of 400–600$^{\circ}C$, showed by the activation energy (E_a) determination, found to be in the range of 0.05–0.32 eV. The sensors responded with in 19–45 s, whereas the recovery time was in the range of 60–200 s. The gas response could be from the surface catalytic reaction of alcohol vapors with $O_{(ads)-}$ at the operating temperature of $400^{\circ}C$.

Wang *et al.*, (2006) prepared orthorhombic structure $LaFeO_3$ with size of 59 nm by glycine combustion method. The as-prepared $LaFeO_3$ nanocrystals were characterized by X-ray diffraction (XRD), transmission electron microscopy (TEM), high reaction transmission electron microscopy (HRTEM), energy dispersive X-ray spectrometer (EDS), scanning electron microscope (SEM), UV–Visible absorption spectroscopy, Laser Raman Spectroscopy (LRS) and Brunauer–Emmett–Teller (BET) nitrogen adsorption. The preparation process can be also applied to the synthesis of other complex oxides such as $NdFeO_3$, $LaCoO_3$ and $LaNiO_3$.

Wang *et al*., (2006) prepared the $LaMO_3$ (M = Fe, Co, Ni) by a glycine combustion method using $La(NO_3)_3.6H_2O$ and $Fe(NO_3)_3.9H_2O$, $Co(NO_3)_2.6H_2O$, and $Ni(NO_3)_2.6H_2O$ as the raw materials, respectively, and $C_2H_5NO_2$ as gelating agent. The products were characterized by XRD, TEM, HRTEM, SEM and BET. DTA and TG were the tools to investigate the thermal decomposition of NH_4ClO_4 (AP) catalyst by $LaMO_3$ (M = Fe, Co, Ni). The heating rate of the propellant modified by obtained $LaCoO_3$ was measured by strand burner method. The experimental showed that the obtained products can play a catalytic role in the thermal decomposition of AP and combustion of AP-based propellant. The catalytic performance of obtained products on AP thermal decomposition was $LaCoO_3$ > $LaNiO_3 \approx LaFeO_3$. Adding 2% of $LaCoO_3$ nanocrystals to AP, the decomposition temperature decreased to 134°C and the heat of decomposition increased by 0.8 kJ g^{-1}. After modifying by 1% $LaCoO_3$ nanocrystals, the heating rate of propellant increased around 8%.

The $Ce_{1-x}Ni_xO_y$ (x = 0.05-0.6) catalysts were prepared by citric acid complexation-combustion method (Shan *et al*., 2006). The $Ce_{1-x}Ni_xO_y$ was used as catalysts for partial oxidation of methane (POM) in the temperature range of 500-900°C. The $Ce_{1-x}Ni_xO_y$ indicated good catalytic activity and stability for the synthesis gas production from POM. The several characterization techniques were used for the catalysts prepared before and after use in the temperature range of 500-900°C. From The $Ce_{1-x}Ni_xO_y$ catalysts had a low BET surface about 10-20 m^2g^{-1}. The surface area of the used samples are lower than the fresh ones due to the sintering effect during the reaction at high temperature.

2.4.2 Sol-gel method

Sol-gel process used the mixing of various components into solution to prepare the multicomponent oxides including perovskite compounds. Advantages of sol-gel process were high purity, compositional homogeneity at a molecular level, and low temperature preparation. The gel formation had been investigated by several researchers. Yang *et al.,* (2004) investigated functional groups of $La_{0.67}Sr_{0.33}MnO_3$ polymerizable complex precursors using FTIR. FTIR spectrum showed sharp absorption bands appeared at 1725 and 1190 cm^{-1} which could be attributed to the monodentate ligand of metal ion with a carbonyl group. The absorption bands indicated at 1380 and 1600 cm^{-1} was due to symmetric and asymmetric vibration of the carbonyl group. A strong absorption band indicated at 1180 cm^{-1}, attributed to the C-O structure from ethylene glycol in the polymerization process. The resin calcined at 823 K showed a pure phase of perovskite. Kao and Yang, (1996) studied the gel precursor of $SrTiO_3$ prepared by polymerizable complex method using infrared spectroscopy. The precursor using acetic acid as a chelating ligand was observed bands at 1420 cm^{-1} and 1560 cm^{-1} corresponding to symmetric and asymmetric vibrations of C-H and C=O of acetate, respectively. The infrared spectra exhibited the acetate chelated with a titanium forming titanyl acylate whether it was chelating or bridging. The infrared spectroscopy of gel precursor $LaNiO_3$ prepared by polymerizable complex method carried out at 573 K in air (Fernandes *et al.,* 2002) was observed at 3700-3000 cm^{-1} and could be attributed to the O-H stretching of the citrate. Vibrations at 1538-1394 cm^{-1} were related to C=O of the carboxylic group coordinated to Ni^{3+} cation in the form of a bidentate complex. The polymerized gel was calcined to form the perovskite phase at low temperature relative to that prepared from the co-precipitation. Popa *et al.,* (2002) prepared $LaMeO_3$ (Me: Mn, Fe and Co) perovskites, obtained by polymerizable complex method at 900°C for 6 h with the grain size of 80 nm and the products were characterized by XRD, scanning electron microscopy (SEM), and Raman spectroscopy. The Raman active phonons in perovskites crystallized in rhombohedral symmetry $LaMnO_{3.15}$, $LaCoO_3$, and orthorhombic symmetry $LaFeO_3$ were reported. Raman spectra were excited using

Ar^+ laser (wavelength 514.5 nm) with various laser beam powers between 10 and 450 µW on a sample at room temperature. Raman bands were compared to those reported for other similar systems with the orthorhombic and rhombohedral Pb nm structure. Raman spectra obtained for the studied systems are related to many factors as the laser irradiation and the structure of $LaMnO_{3.15}$, $LaFeO_3$ and $LaCoO_3$ which greatly depended on the method of preparation, particle size, oxygen content, symmetry, temperature or the oxygen partial pressure.

3. Perovskite characterization

3.1 X-ray diffraction (XRD)

X-ray diffraction spectroscopy is a well-known and the most frequently applied technique in perovskite characterization. This technique is a versatile, nondestructive analytical technique for identification and quantitative determination of the various crystalline forms, known as phase, of compounds present in powder and solid samples. Identification is achieved by comparing x-ray diffraction pattern (diffractogram) obtained from an unknown sample with an internationally recognized database containing reference patterns. A crystal lattice is a regular three dimensional distribution, cubic, fluorite, etc, of atom in space. These are arranged so that they form a series of parallel planes separated from one another by a distance d, which varies according to the nature of the material. For any crystals, plane exists in a number of different orientations, each with its own specific d-spacing. X-ray diffraction is the elastic scattering of x-ray photons by atom in a periodic lattice. The scattered monochromatic x-rays that are in phase give constructive interference (Niemantsverdriet, 1995). Figure 5 illustrates how diffraction of x-rays by crystal planes allows one to derive lattice spacing by using the Bragg's equation:

$$n\lambda = 2d\sin\theta \qquad (11)$$

where λ is the wavelength of the x-rays;

d is the distance between two lattice planes;

θ is the angle between the incoming x-rays and the normal to the reflecting lattice plane;

n is the integer called of the reflection.

The primary use of the Bragg's law is in the determination of the spacing (d) between two planes (h k l) in the lattice.
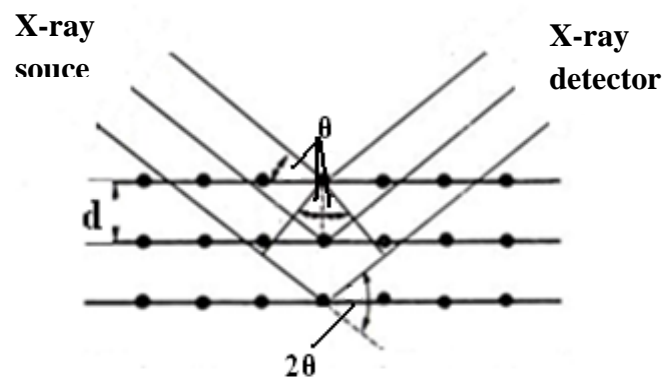
Figure 5 Derivation of Bragg's law for x-ray diffraction.

Source: Adapted from Smart and Moore (1995)
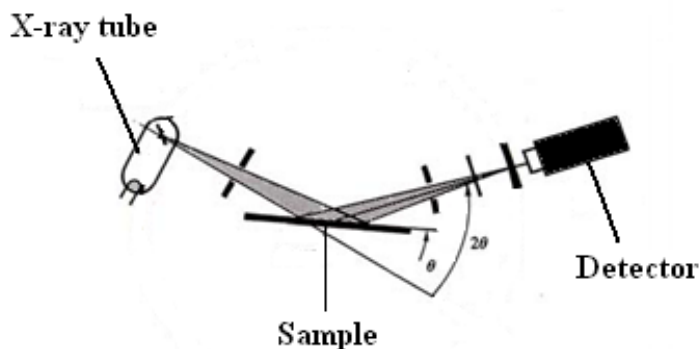
Figure 6 Diagram of a powder x-ray diffractometer.

Source: Adapted from Smart and Moore (1995)

The x-ray spectrometer is shown in Figure 6. X-ray from the x-ray source is incident on a sample which is placed on a powder specimen. The diffracted x-ray passes through a slit to a detector. The sample is positioned so that its diffracting planes make some particular angle θ with the incident beam and the detector is set at the corresponding angle 2θ. The detector records the intensity of the diffracted beams and these can be plotted out as function of 2θ. Each crystalline substance has its own characteristic powder diffraction pattern which may be used for its identification. Standard patterns are given in the powder diffraction file (known as the JCPDS file).

For standard $LaCoO_3$ file No. 25-1060 shown in Figure 7, the characterization used Cu K_α as the x-ray source, of which the wavelength is 1.540 Å.

28
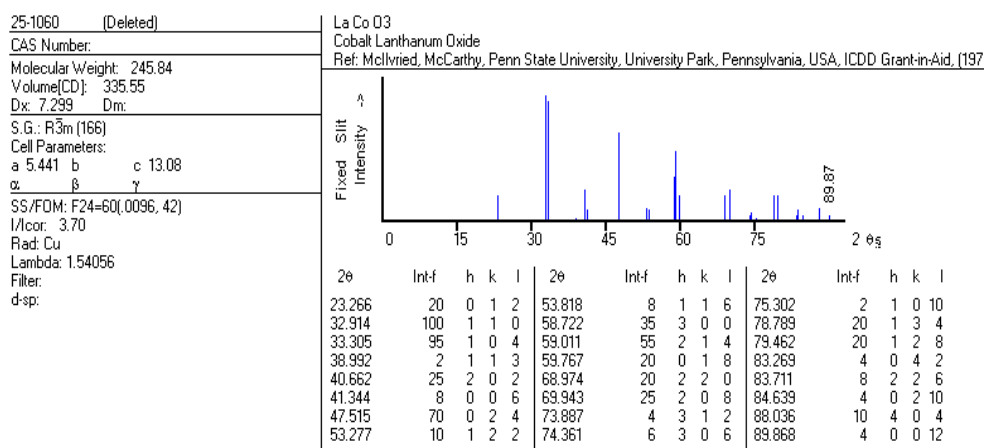
Figure 7 Powder diffraction files (JCPDS) No. 25-1060 of LaCoO₃.

The perovskite structure of LaCoO$_3$ has crystal unit cells as cubic, rhombohedral, and hexagonal cells. The d spacing and the h k l indices correlate with the unit cell parameters shown in Table 3.

Table 3 Unit cell parameters of crystal structures.

Crystal Structure	Unit cell shape	Formula
Cubic	$a = b = c$ $\alpha = \beta = \gamma = 90°$	$\dfrac{1}{d^2} = \dfrac{h^2 + k^2 + l^2}{a^2}$
Tetragonal	$a = b \neq c$ $\alpha = \beta = \gamma = 90°$	$\dfrac{1}{d^2} = \dfrac{h^2 + k^2}{a^2} + \dfrac{l^2}{c^2}$
Orthorhombic	$a \neq b \neq c$ $\alpha = \beta = \gamma = 90°$	$\dfrac{1}{d^2} = \dfrac{h^2}{a^2} + \dfrac{k^2}{b^2} + \dfrac{l^2}{c^2}$
Hexagonal	$a = b \neq c$ $\alpha = \beta = 90°,$ $\gamma = 120°$	$\dfrac{1}{d^2} = \dfrac{4}{3}\left(\dfrac{h^2 + hk + k^2}{a^2}\right) + \dfrac{l^2}{c^2}$
Rhombohedral	$a = b = c$ $\alpha = \beta = \gamma \neq 90°$	$\dfrac{1}{d^2} = \dfrac{\left(h^2 + k^2 + l^2\right)\sin^2\alpha + 2\left(hk + kl + hl\right)\left(\cos^2\alpha - \cos\alpha\right)}{a^2\left(1 - 3\cos^2\alpha + 2\cos^3\alpha\right)}$

Source: Adaped from Cullity and Stock (2001)

Determination of crystallite size

Crystallite size can be obtained from the XRD technique by measuring the diffraction line broadening. At the simplest level, the application of the Scherrer's formula led to an estimate of the mean crystallite size. The breadth of an x-ray reflection on the lattice planes of crystallites (small single crystals) depend upon the characteristics of crystallites (size and defects in the lattice) and instrumental factors. Considering an x-ray reflection, Scherrer first showed that the mean dimension in micrometer, D, of the crystallites composing a powder is related to the pure x-ray diffraction broadening or the full width at half maximum intensity (FWHM) in radians, β, by the Eq. (12) (Klung and Alexander, 1954).

$$D \; = \; \frac{K\lambda}{\beta cos\theta} \qquad\qquad (12)$$

where K is a constant

λ is the wavelength of the x-ray radiation employed

β is the full width at half maximum intensity (FWHM), often written as $\beta_{1/2}$, expresses in radians

θ is the angular position of the peak maximum

The constant K depended on the definitions of crystallite size and broadening, the shape of crystallites, and the reflection being examined. When $\beta_{1/2}$ is used, the value of K should be taken at 0.9.

The Scherrer's formula assumed that small crystallite size is the sole source of broadening of the diffraction profile. In fact, there is always a broadening due to the various instrumental factors such as slit width, sample size, penetration of the x-ray beam into the specimen, imperfect focusing, or misalignment of the diffraction. By measuring experimental and reference lines, the true peak breadth which one use in Eq. (12) can be calculated by the Warren formula (Equation 13);

$$\beta^2 \; = \; \beta_m^2 \; - \; \beta_s^2 \qquad\qquad (13)$$

where β_m is the full width at half maximum intensity (FWHM) of measured sample peak in radians. β_s is the full width at half maximum intensity (FWHM) of standard peak or instrument broadening in radians, which is obtained from diffraction pattern of standard.

Single-phase crystallization of pure perovskite LaMeO$_3$ (Me = Co, Mn, Fe) phases were studied by Popa *et al.*, (2002). LaMnO$_{3.15}$ had a rhombohedral symmetry after thermal treatment at 973 K (JCPDS 32-484), LaCoO$_3$ had a rhombohedral symmetry after thermal treatment at 923 K (JCPDS 25-1060) and LaFeO$_3$ had an orthorhombic symmetry after thermal treatment at 823 K (JCPDS 37-1493). Crystallite sizes of samples were calculated based on the FWHM of a diffraction peak using the Scherrer equation. Taguchi *et al.*, (2002) prepared LaCoO$_3$ by citrate method. The crystallite sizes of LaCoO$_3$ synthesized at 873, 973, 1073, and 1173 K were 12.2, 16.4, 18.9, and 21.0 nm, respectively, which increased with increased synthetic temperature. Krupicka *et al.*, (2002) studied the crystallite sizes of citrate precursors of LaCoO$_3$ calcined at 873 and 1073 K. The crystallite sizes were 9.7-10.7 nm and 13.5-15.4 nm, respectively. The LaFeO$_3$ perovskite was prepared by polymerizable citrate complex method. The average size under the calcinations temperature of 873 K for 1 h was about 40 nm (Zhao *et al.*, 2000).

3.2 X-ray absorption near- edge structure (XANES)

When the x-rays hit a sample, the oscillating electric field of the electromagnetic radiation interacts with the electrons bound in an atom. Either the radiation will be scattered by these electrons, or absorbed and excite the electrons shown in Figure 8.
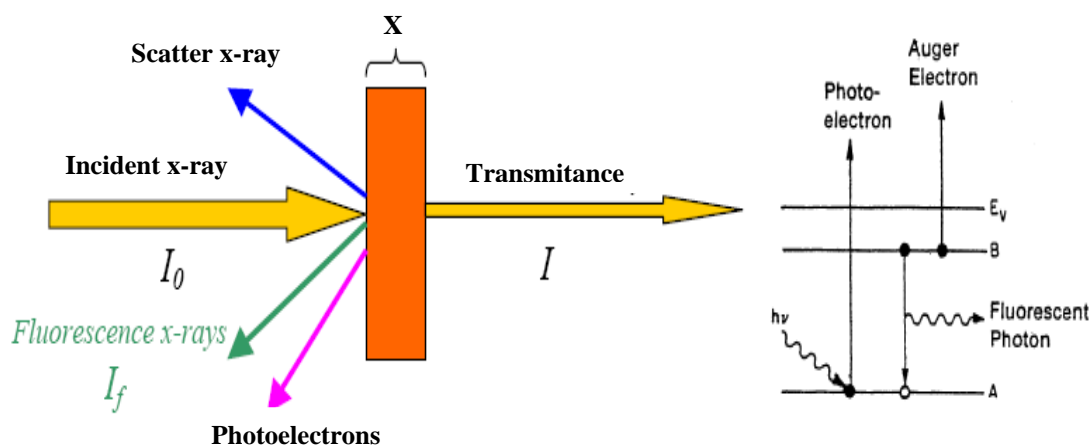
Figure 8 Photoionization process occurred in XANES.

Source: Adaped from Farideh (2001)

A narrow parallel monochromatic x-ray beam of intensity I_0 passing through a sample of thickness x will get a reduced intensity I according to the expression:

$$\ln (I_0 /I) = \mu \, x \qquad\qquad (14)$$

where μ is the linear absorption coefficient, which depends on the types of atoms and the density ρ of the material. At certain energies where the absorption increases drastically, and gives rise to an absorption edge. Each such edge occurs when the energy of the incident photons is just sufficient to cause excitation of a core electron of the absorbing atom to a continuum state, i.e. to produce a photoelectron. Thus, the energies of the absorbed radiation at these edges correspond to the binding energies of electrons in the K, L, M, etc, shells of the absorbing elements. The absorption edges are labeled in the order of increasing energy, K, L_I, L_{II}, L_{III}, M_I,...., corresponding to the excitation of an electron from the 1s ($^2S_{1/2}$), 2s ($^2S_{1/2}$), 2p ($^2P_{1/2}$), 2p ($^2P_{3/2}$), 3s ($^2S_{1/2}$), ... orbitals (states), respectively. An x-ray absorption spectrum is generally divided into 4 sections: 1) pre-edge ($E < E_0$); 2) x-ray absorption near edge structure (XANES), where the energy of the incident x-ray beam is $E = E_0 \pm 10$ eV; 3) near edge x-ray absorption fine structure (NEXAFS), in the region between 10 eV up to 50 eV above the edge; and 4) extended x-ray absorption fine structure (EXAFS), which starts approximately from 50 eV and continues up to 1000 eV above the edge.

3.3 Scanning electron microspore (SEM)

The scanning electron microscope (SEM) is a type of electron microscope that uses electrons instead of light to form an image. SEM uses a highly focused electron beam to strike and interact with a sample which is contained in a high vacuum environment to form a high resolution image. The images formed by the scanning electron microscope are from secondary electrons, backscattered electrons, characteristic x-ray, Auger electrons, and others that are emitted by the sample. The scanning electron microscope has many advantages over traditional microscopes. The SEM has a large depth of field, which allows more of a specimen to be in focus at one time. The SEM also has much higher resolution, so closely spaced specimens can be magnified at much higher levels.

Advantages of SEM
- high depth of focus/field
- direct observation of the external form of real objects at high magnifications
- wide range of magnifications (below 50,000x to over 100,000x)

Disadvantages of SEM
- high vacuum environment of the specimen
- inability to show internal detail
- inability to obtain highest resolution
- some samples need to be coated with a conductive layer

Applications of SEM

There are countless applications of SEM. Some of these applications include:
- analyzing biological samples (diseases, bacteria)
- materials sciences, looking for fracture and cracks in/on materials such as polymers, metals, ceramics, etc.
- inspecting medical devices with attached tissue
- forensic science (causes of failure, modes of failure, etc.)
- microelectronics failures (printed circuit boards, microship pins and

wiring)

Taguchi *et al*. (2002) synthesized $LaCoO_3$; gel was prepared by adding citric acid to the aqueous solution of $La(NO_3)_3.6H_2O$ and $Co(NO_3)_2.6H_2O$. To obtain $LaCoO_3$, the gel with 0.007 mol of citric acid was fired at 600°C. Both large (> 20 µm) and small (≈1 µm) particles can be observed. From SEM results, the large particle consists of many small particles. The nanostructures of $LaCoO_3$ powders were prepared by co-precipitation and with the citrate gel method (Natile *et al*., 2007). From SEM results, nanoscaled spherical particles which are clustered together formed a highly porous microstructure composed by sheet-like fragments. However, the aggregate's diameters ranged from about 60-80 nm. The large difference between the Scherrer value and the particle size determined by SEM can be explained considering that the SEM images showed a polycrystalline particle composed of many crystallites. Moreover, the SEM images revealed a more uniform grain size distribution and homogeneous microstructure. But the sample prepared by co-precipitation, in contrast, showed a greater in homogeneity.

3.4 The Brunauer Emmett Teller method

Adsorption measurements have a variety of uses and applications. For example; powder materials, sinter frits, filters, ceramics, washcoats, catalysts, polymers, and coat tape etc. The most important one is determining surface area of perovskites. The principle method of measuring total surface area of perovskite is by adsorption of particular molecular species from gas or liquid onto the surface. If the condition under which a complete adsorption layer, averaging one molecule thick, can be established and the area covered per molecule is known, then the quantity of adsorbed material gives directly the total surface area of the perovskite. The most common method of measuring surface area is calculated by the Brunauer, Emmett, and Teller (BET) equation (Satterfield, 1980).

The bonding in physisorbed system is weak, Van der Waals interaction, tends to be reversible, in the sense that the surface layer is always in equilibrium with the molecules of the gas phase. The relation at constant temperature between the quantity of gas adsorbed and the pressure with which it is in equilibrium is termed an adsorption isotherm. Most physical adsorption isotherms may be grouped into five types, which are frequently referred to as the Brunauer, Deming, Deming and Teller (BDDT) classification in Figure 9 (Satterfield, 1980).
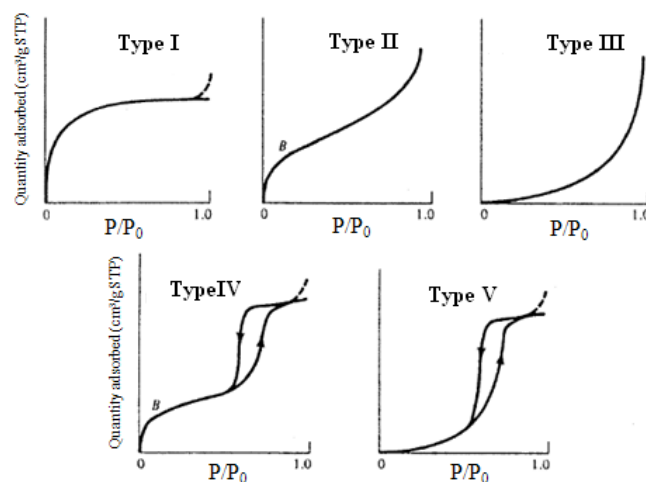
Figure 9 The five types of adsorption isotherms as classified by Brunauer.

Source: Adapted from Satterfield (1991)

Type I is frequently called Langmuir type. However, it also corresponds to filling of micropores within the solid rather than monolayer adsorption. Type II, sometimes termed the sigmoid or S-shaped isotherm, is commonly encountered on nonporous or macroporous materials. Point B occurs as a knee and is the stage at which monolayer coverage is complete and multilayer adsorption begins. Type III is relatively rare and the forces of adsorption are weak. The characteristic hysteresis loop of type IV systems is indicative of the presence of narrow pore (mesopores 2-50 nm). A hysteresis effect involves the capillary condensation within the pores. Type V is similar to type III, but with pore condensation taking place at higher values of

P/Po. It is also relatively rare. The specific surface area S of the adsorbent is calculated from V_m by the equation:

$$S\,(m^2/g) \;=\; \frac{V_m \sigma N_A}{m V_0} \qquad\qquad (15)$$

where S = the specific surface area of adsorbent (m^2/g)

V_m = volume of gas adsorbed in monolayer (cm^3)

σ   = the area of surface occupied by a single adsorbed gas molecule $(16.2 \times 10^{-20}\ m^2/molecule$ in the case of nitrogen)

N_A = the Avogadro constant $(6.023 \times 10^{23}$ molecules/mol)

m = the mass of the adsorbing sample (g)

V_0 = the molar volume of the gas $(22.414\ cm^3/mol)$

The range of linearity is always restricted to a limited part of the isotherm. Complexities associated with the realities of multilayer adsorption or pore condensation increase deviation.

MATERIALS AND METHODS

Materials

1. Reagents

- Lanthanum oxide (La_2O_3, >99.99%, Fluka)
- Cobalt oxide (Co_3O_4, >99.95%, Fluka)
- Lanthanum nitrate hexahydrate [$La(NO_3)_3.6H_2O$, 99%, Fisher Chemicals]
- Cobalt nitrate hexahydrate [$Co(NO_3)_2.6H_2O$, 99%, Univar]
- Lanthanum (III) hydroxide [$La(OH)_3$, 99.9%, Aldrich]
- Cobalt (II) hydroxide [$Co(OH)_2$, 95%, Aldrich]
- Acetone (C_3H_6O, 99.8%, CARLO ERBA)
- Ammonia solution [NH_4OH, 29.3%, Baker]
- Nitric acid [HNO_3, 65%, Merk]
- Chromosorb G/AW-DMCS 80-100 mesh ASTM (0.15-0.18 mm) [Fluka]
- Ethanol (C_2H_5OH, 99.8 %, CARLO ERBA)
- Oxygen gas (99.995%)
- Carbon monoxide gas (CO, 99.2%)

2. Instruments

- pH measurements were performed on Consort C830 pH meter.

- Solid state reaction ($LaCoO_3$-ss) perovskites were calcined in a Eurotherm furnace using an alumina crucible.

- Co-precipitation ($LaCoO_3$-cp) and modified wet powder dispersion ($LaCoO_3$-wd) perovskites were calcined in a Thermolyne 2100 tube furnace using a quartz tube.

- X-ray diffraction (XRD) patterns were record on a Shimadzu XRD 6000 using Cu K_α radiation (λ = 1.54 Å). The crystalline phase of sample has been indexed by comparison with the JCPDS files (Joint Committee on Powder Diffraction Standards). The experiment was carried out at Material Innovation Department, Thailand Institute of Scientific and Technological Research (TISTR).

- X-ray absorption (XAS) measurements were carried out on beam line 8 (BL8) at Siam Photon Laboratory of National Synchrotron Research Center.

- Surface area of the perovskites were measured by the Brunauer Emmett Teller (BET) method from nitrogen adsorption isotherms, recorded at liquid nitrogen temperature on a QUANTA CHROME apparatus model AUTOSORB-1.

- Samples morphology was performed on a scanning electron microscope (JEOL JSM-T330A) at 12 and 17 kV at Material Innovation Department, Thailand Institute of Scientific and Technological Research (TISTR).

- The e-corder (EDAQ) equipped with the resistant measuring cable was used for data recording at Department of Chemistry, Faculty of Science, Kasetsart University.

Methods

1. Perovskite Preparation

LaCoO$_3$-ss (1:1, 1:5 (high Co), and 5:1 (high La)) perovskites were prepared by solid state reaction and LaCoO$_3$-ss (1:1) was also prepared by co-precipitation and modified wet powder dispersion.

1.1 Solid state reaction

The LaCoO$_3$-ss (1:1, high Co, and high La) were prepared by grinding La$_2$O$_3$ and Co$_3$O$_4$. Acetone was added to the mixture of the solid substrate: acetone ratio of 1:1. The mixture was ball-milled for 16 h at 220 rpm. Then, it was filtered off, dried at 80°C for 4 h, and calcined at 700-900°C for 2 h. A flowchart of preparation steps was shown in Figure 10.
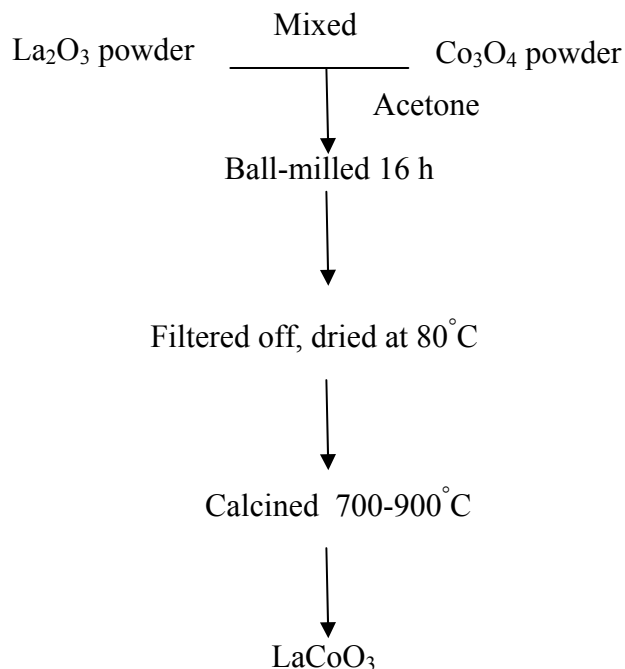
Figure 10 A flowchart of LaCoO$_3$ preparation using solid state reaction method.

The calcination steps were set as follows:

- The first step: the temperature was increased from room temperature to 300 °C and held for 1 h . The ramp rate of process was 5°C min⁻¹.

- The second step: the temperature was heated up to 700°C to 900°C and held for 2 h. The cooling rate of process was 5°C min⁻¹.
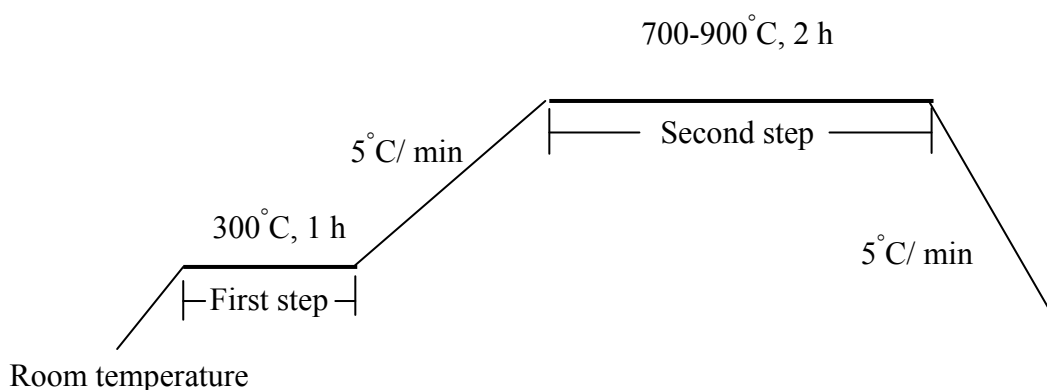
Figure 11 Calcination diagram for LaCoO₃ perovskite using solid state reaction
         method.

   1.2 Co-precipitation method

        Perovskite were prepared from La(NO₃)₃.6H₂O, Co(NO₃)₂.6H₂O with ammonium hydroxide (NH₄OH) as a precipitating agent as shown in Equation (16).

$$La(NO_3)_3 + Co(NO_3)_2 + 5OH^- \xrightarrow[\text{controlled pH}]{} La(OH)_3 + Co(OH)_2 + 5NO_3^- \qquad (16)$$
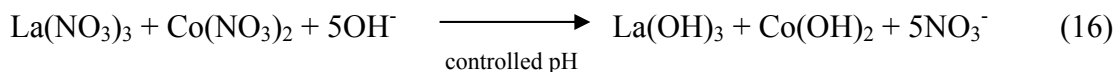
        Co-precipitation of La(OH)₃ and Co(OH)₂ for the precipitation of LaCoO₃ can be done by controlling pH of the solution which was calculated from K_{sp} of each salt.

1.2.1 Experiments

La(NO$_3$)$_3$.6H$_2$O and Co(NO$_3$)$_2$.6H$_2$O were used. Each metal salt was dissolved in distilled water to obtain 25.00 cm^3 of a solution of 0.2000 M. Both solutions were mixed and 5% NH$_4$OH as a precipitating agent was slowly added into the stirring mixture until pH 9.25 was reached (Srichaisiriwech, 2002). La(OH)$_3$ and Co(OH)$_2$ precipitates were formed. They were filtered off and dried at 110°C for 3 h. During calcinations, the hydroxide precipitates were transformed to the LaCoO$_3$ perovskite-type oxide. A flowchart of preparation steps was shown in Figure 12.

La(NO$_3$)$_3$ solution —— **Mixed** —— Co(NO$_3$)$_3$ solution

NH$_4$OH

↓

Adjusted pH, co-precipitated

↓

Filtered off, washed, dried at 110°C

↓

Calcined

↓
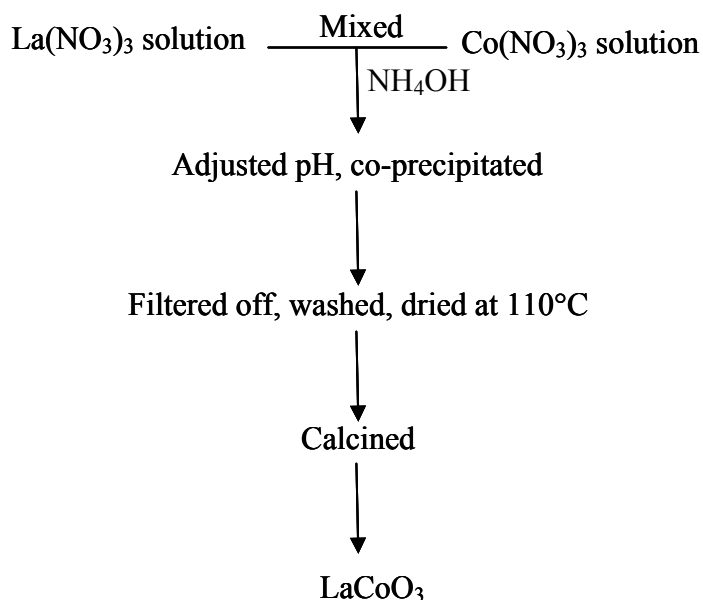
LaCoO$_3$

Figure 12 A flowchart of LaCoO$_3$ preparation using co-precipitation method.

1.3 Modified wet powder dispersion method.

From the Thailand Patent Request No. 0901000358, La(OH)$_3$ was dissolved in HNO$_3$ and Co(OH)$_2$ was dispersed in distilled water, then both solutions were mixed. The precipitates were obtained by adding NH$_4$OH as precipitating agent until pH 9.2-9.3 was reached. The precipitates were filtered off, washed, and dried at

110°C. The LaCoO$_3$ perovskite structure was formed after calcinations at 700°C for 7 h. The LaCoO$_3$ synthesis procedure by wet powder dispersion was shown in Figure 13.

Co(OH)$_2$ suspension ——— Mixed ——— La(OH)$_3$ solution

↓ NH$_4$OH

Adjusted pH, precipitated

↓

Filtered off, washed, dried at 110°C

↓

Calcined

↓
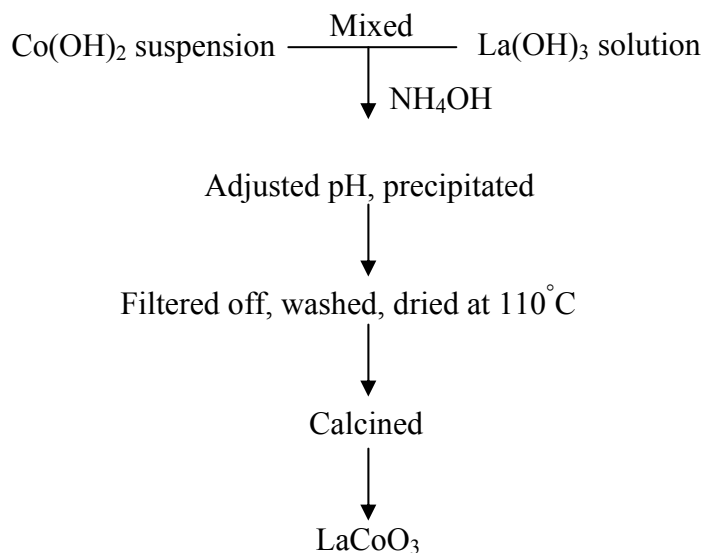
LaCoO$_3$

Figure 13 A flowchart of LaCoO$_3$ synthesis using modified wet powder dispersion method.

2. Perovskite characterization

LaCoO$_3$ perovskites were characterized. Crystallinity and crystallite size analysis were performed using powder x-ray diffraction (XRD). BET surface area of the prepared perovskites was measured by nitrogen adsorption. SEM and TEM were used to characterize the surface and phase compositions of LaCoO$_3$ perovskites.

2.1 Powder x-ray diffraction (XRD)

2.1.1   Determination of crystal structure

All calcined samples were analyzed by XRD.   The XRD experiments were performed on a Shimadzu XRD 6000 x-ray diffractometer using Cu K$_\alpha$ radiation (λ = 1.54 Å) and a curved graphite monochromator. The x-ray source

was operated at 40 kV and 40 mA. The powder x-ray diffractograms were recorded at step size 0.02° an integration time of 1.0 s. Data were collected between 20 and 80°. The diffraction patterns have been indexed by comparison with the JCPDS card (Joint Committee on Powder Diffraction Standards).

2.1.2 Determination of crystallite size

Crystallite size (D) was determined from XRD pattern using the Scherrer equation (Klung and Alexander, 1954) as previously described in literature review section. For the values of β_s, the instrument broadening was obtained using α-Al_2O_3 as the reference material, which was prepared by calcinations of Al_2O_3 at 1200°C for 4 h. under normal atmospheric pressure. The structure of α-Al_2O_3 was characterized by an x-ray diffractometer and compared with JCPDS 83-2081 (α-Al_2O_3).

2.2 X-ray absorption near- edge structure (XANES)

XANES experiments were carried out at the Siam Photon Laboratory. It was tunable by a fixed-exit double crystal monochromator (DCM) euipped with several types of crystal for covering photon energy from 1250 eV to 10000 eV and average stored current of 100 mA. The x-ray energy was monochromatized with channel-cut Ge (220) crystal monochromater. The Co K-edge XANES spectra were recorded in transmission mode, using two ionization chamber filled with argon gas as detectors. The Co K-edge XANES of $LaCoO_3$ sample and that of a 7 μm thin Co foil (for purpose of energy calibration) were measured simultaneously in transmission mode at room temperature. K-edge absorption of Magnesium up to Zinc could be studied. Other heavier atomic species could be investigated via L or M edges. Transmission mode was suitable for sample having x-ray absorbing atoms (absorbers) at high density (>5%wt). The sample must be layered to have even thickness, and no "pinhole". Optimal weight of the sample can be calculated by Optmass. Intensity of

the incident x-ray beam (I_0) and transmitted x-ray beam (I_1) were monitored by a 10-cm long ion chamber and a 40-cm long ion chamber, respectively. Absorption is defined by $\ln(I_0/I_1)$.
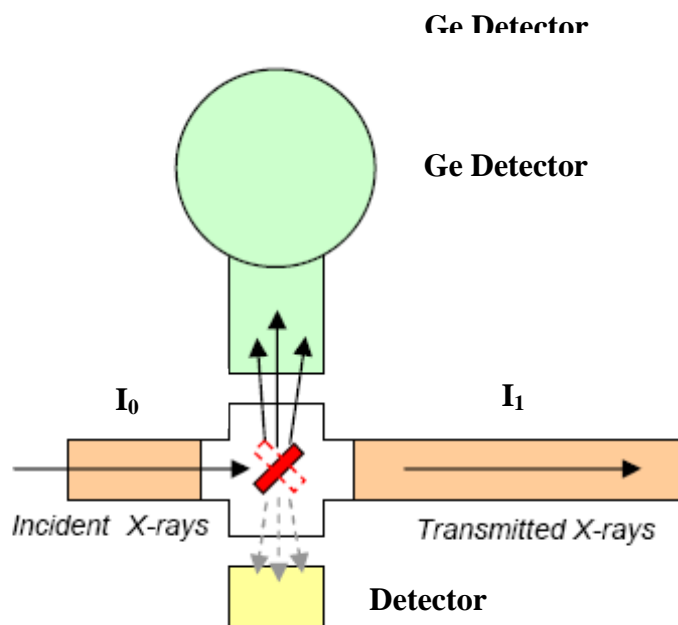
Figure 14 Experimental setup for TM-XANES.

Preparing powdered sample for TM-XANES

- Put some samples in a small agate mortar, use pestle to grind the sample into very fine powder.

- Cut a piece of hard paper or plastic sheet to make a sample frame.

- Place a piece of thin Kapton (Polyimide) tape on the frame.

- Weigh the ground sample to the right amount that equals to the optimal mass, a mass of the applied sample on a certain area which its thickness gives the absorption length of 2. Apply the sample over the sticky window area evenly and homogeneously and make sure there is no "pinhole" in the sample area.

- Cover the sample area with a Kapton tape as shown in Figure 15.

Kapton tape

Front side   Back side

Sample

Front side   Front side
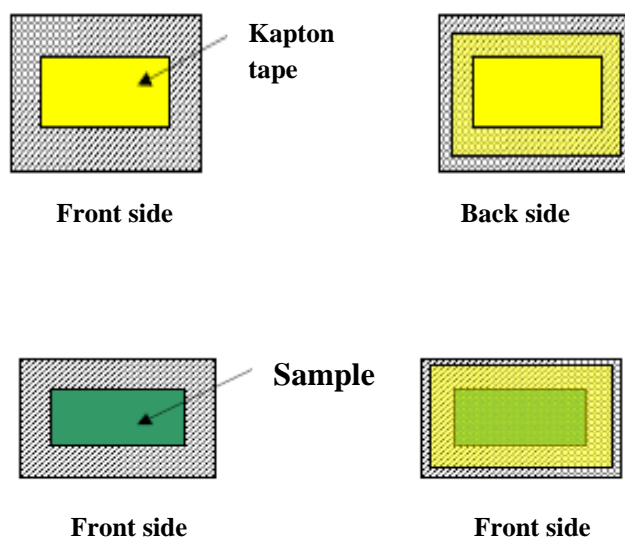
Figure 15 Preparing powdered sample for TM-XANES.

2.3   Nitrogen adsorption desorption

Surface areas of the samples were determined by nitrogen adsorption isotherm, evaluated from the BET equation. The experiment was performed on a AUTOSORB-1 instrument. Prior to each measurement, the sample was degassed for 180 min at 300°C under vacuum. The sample cell and P_0 cell were immersed into liquid nitrogen. The adsorbing gas was admitted with an increment of 1.0 cm^{3}g^{-1} STP. Adsorption isotherm was a measurement of the accumulated quantity of the adsorbed gas and the relative pressure (P/P$_0$) at a constant temperature. Similarly, desorption isotherm was a measure of the mole quantity of nitrogen gas released from the sample as the relative pressure. The surface areas were determined by the BET equation yielded a straight line between P/P$_0$ values from about 0.05 to 0.3.

2.4   Scanning electron microscope (SEM)

SEM was used to characterize the perovskite morphology. The sample powders were mixed with ethanol, then dropped on metal stub, dried at $105^{\circ}C$ for 2 h and coated Au as conductive layer for 10s by sputter coating. Then sample was placed into sample chamber and vacuumed. SEM was operated at 12 and 17 kV. The sample preparation procedure for SEM was shown in Figure 16.

sample

stub
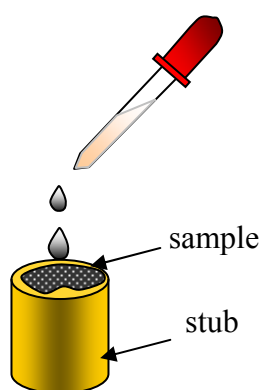
Figure 16 Sample preparation for SEM analysis.

3. Carbon monoxide (CO) sensor test

3.1 Fabrication of CO gas sensor

The prepared $LaCoO_3$ (1:1, high Co and high La), $LaCoO_3$-cp and $LaCoO_3$-wd powders were mixed in ethanol solution to form pastes. The paste was coated onto an Al_2O_3 tube on which two silver paste had been installed at each end. The Al_2O_3 tube was about 4.5 mm in length, 2 mm and 1.6 mm in external and internal diameter (Figure 17). A small alloy coil was placed through the tube as a

microheater. The heater provide operating temperatures from 29 to $133^{\circ}C$. The temperature was controlled by adjusting the heating power.
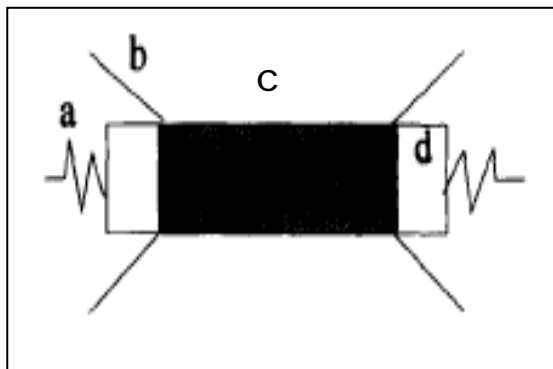
Figure 17 Structure of the gas sensor : a) microheater coil, b) silver paste, c) sensing layer, and d) Al_2O_3 tube.

3.2 Measurement of CO gas sensor

Experimental set up for CO sensor was shown in Figure 18. $LaCoO_3$ was coated on alumina tube and the silver paste was used as the electrode material. The fabricated sensor was connected to the measuring cables with four channels, two for the heater and two for the resistance/voltage measurement. The heater was connected to the voltage supply. The test gas was introduced into the closed chamber via a stopcock. Carbon monoxide gas was injected into the sensor chamber and the sensor resistance was monitored with time. The voltage supply was varied from 0.0 to 7.5 volts to obtain the optimum working voltage.
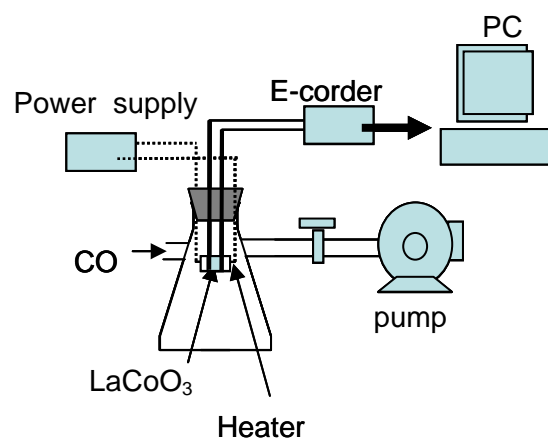
Figure 18 Experimental setup for CO gas sensor.

RESULTS AND DISCUSSION

1. Perovskite Characterization

The $LaCoO_3$ samples obtained from the solid state, co-precipitation, and modified wet powder dispersion methods were assigned as $LaCoO_3$-ss (at the La:Co molar ratio of 1:1, 1:5 (called high Co) and 5:1 (called high La)), $LaCoO_3$-cp, and $LaCoO_3$-wd, respectively. $LaCoO_3$ perovskites were characterized by XRD, XANES, BET and SEM methods.

1.1 X-ray Powder diffraction (XRD)

The x-ray diffraction patterns of $LaCoO_3$-ss (1:1) at the calcination temperature of 700, 800, 850 and $900^\circ C$ for 2 h were shown in Figure 19. As increasing the calcination temperature, the $LaCoO_3$-ss (1:1) phase was increased. At $700^\circ C$, there were the impurity peaks of La_2O_3 at 2θ of 27.32°, 27.98°, 29.97°, and the impurity peaks of Co_3O_4 at 2θ of 31.49°, 36.88°, and 65.27° as shown in Figure 19 (a). As increasing temperature, La_2O_3 and Co_3O_4 increasingly reacted and $LaCoO_3$ was formed rhombohedral structure. As increasing the calcination temperature to $900^\circ C$, the patterns showed the rhombohedral $LaCoO_3$ at 2θ of 33.33°, 47.54°, and 59.02° (JCPDS PDF No. 25-1060) and the less impurity peak of La_2O_3 and Co_3O_4 as shown in Figure 19 (b), (c), and (d). Phase identification was made by using the JCPDF data files No. 05-0602 for La_2O_3 and No. 42-1467 for Co_3O_4.
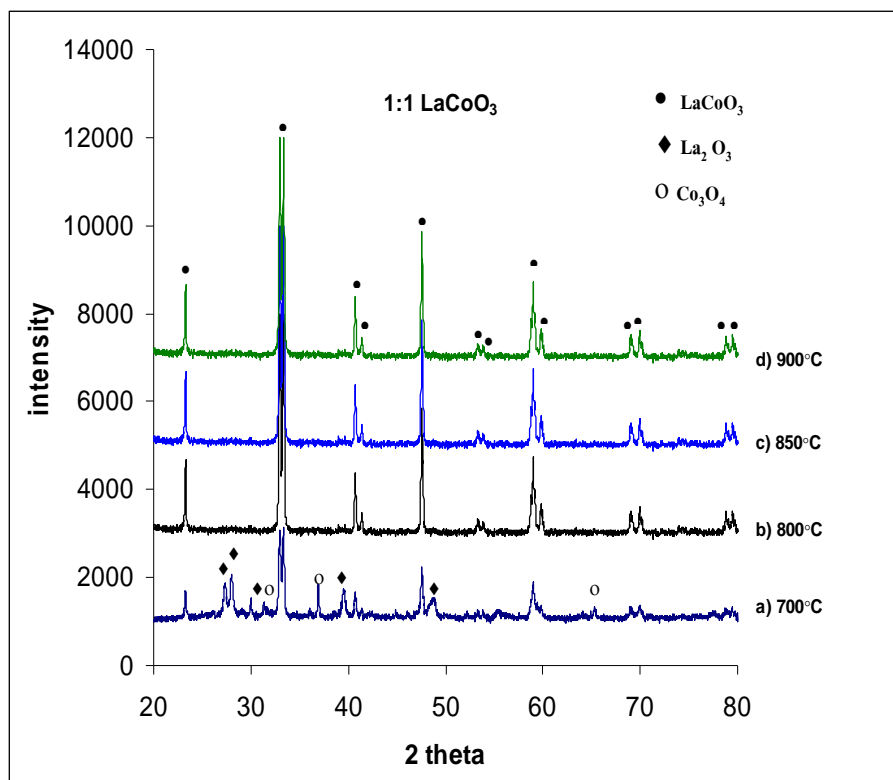
Figure 19 XRD patterns of LaCoO₃-ss (1:1) at the calcination temperatures of 700-
900°C for 2 h.

The x-ray diffraction patterns of LaCoO₃-ss (high Co) at the calcination temperature of 700, 800, 850 and 900°C for 2 h were shown in Figure 20. At 700°C, there were the impurity peaks of La_2O_3 at 2θ of 26.15°, 26.87° and Co_3O_4 at 2θ of 30.93°, 36.54°, 44.43°, and 64.99° as shown in Figure 20 (a). As increasing the calcination temperature to 900°C, there were only the impurity peaks of the excess Co_3O_4 at 2θ of 31.37°, 36.95°, 44.87°, and 65.35° as shown in Fig 20 (b-d). LaCoO₃-ss (high Co) was formed in the rhombohedral structure.
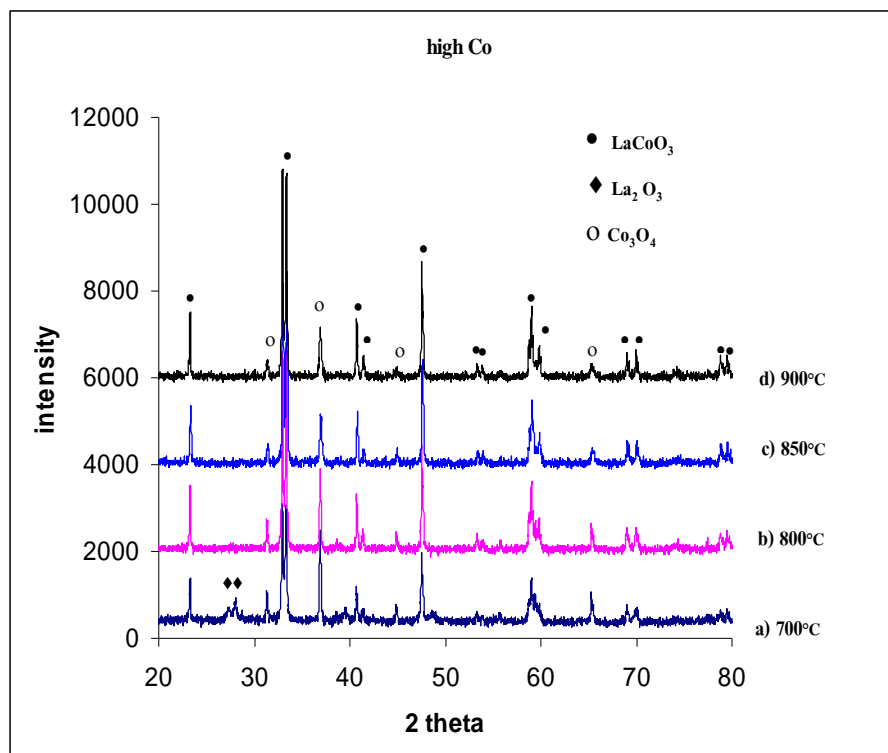
Figure 20 XRD patterns of LaCoO₃-ss (high Co) at the calcination temperatures of 700-900°C for 2 h.

The x-ray diffraction patterns of LaCoO₃-ss (high La) at the calcination temperature of 700, 800, 850 and 900°C for 2 h were shown in Figure 21. As increasing the calcination temperature, the LaCoO₃ phase was increased. At 700-900°C, there were the impurity peaks of the excess La₂O₃ at 2θ of 26.14°, 29.18°, 29.72°, 39.57°, 52.23°, 53.91°, and 55.54° as shown in Figure 21 (a-d). LaCoO₃-ss (high La) was formed in the rhombohedral structure.
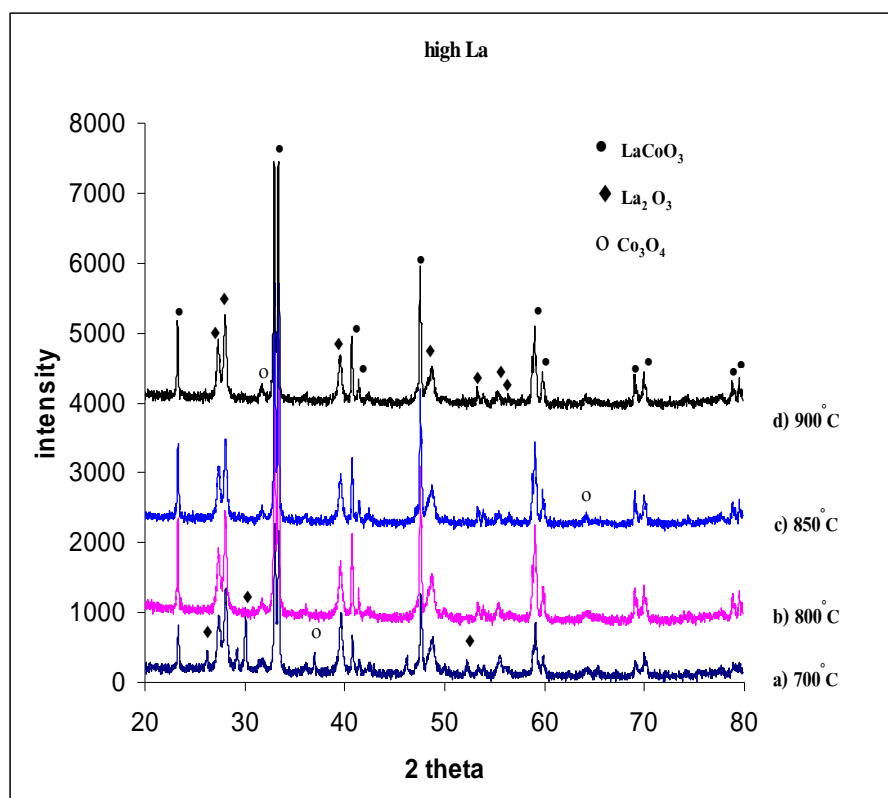
Figure 21 XRD patterns of LaCoO$_3$ -ss (high La) at the calcination temperatures of 700-900°C for 2 h.

The XRD patterns of the samples obtained from both the co-precipitation and modified wet powder dispersion methods showed the presence of rhombohedral LaCoO$_3$ as shown in Figure 22 (Prangsri-aroon 2008). The information confirmed the impurity phase of Co$_3$O$_4$ in LaCoO$_3$-cp and the trace of La(OH)$_3$ in LaCoO$_3$-wd.
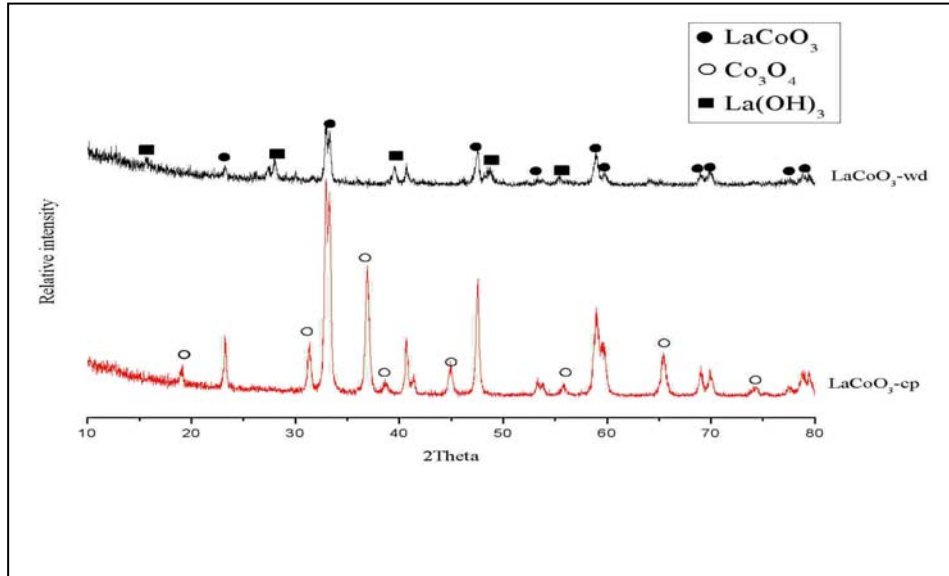
Figure 22 XRD patterns of LaCoO$_3$-cp and LaCoO$_3$-wd at pH 9.25 after calcination at 700°C.

From XRD patterns, the crystallite size of perovskite can be calculated using the Scherrer's equation as previously stated in literature review.

$$D = \frac{0.9\lambda}{\beta\cos\theta} \qquad (17)$$

β could be calculated by Warren equation:

$$\beta = \sqrt{\beta_m^2 - \beta_s^2} \qquad (18)$$

where β   is the full width at half maximum intensity (FWHM)

β$_m$ is the full width at half maximum intensity (FWHM) of measured LaCoO$_3$ peak in radians

β_s is the full width at half maximum intensity (FWHM) of measured α-Al_2O_3 standard peak

- Determination of β_s

Figure 23 showed the XRD patterns of Al_2O_3 calcined at $1200^\circ C$ which was corresponded to α-Al_2O_3 (JCPDS 83-2081).
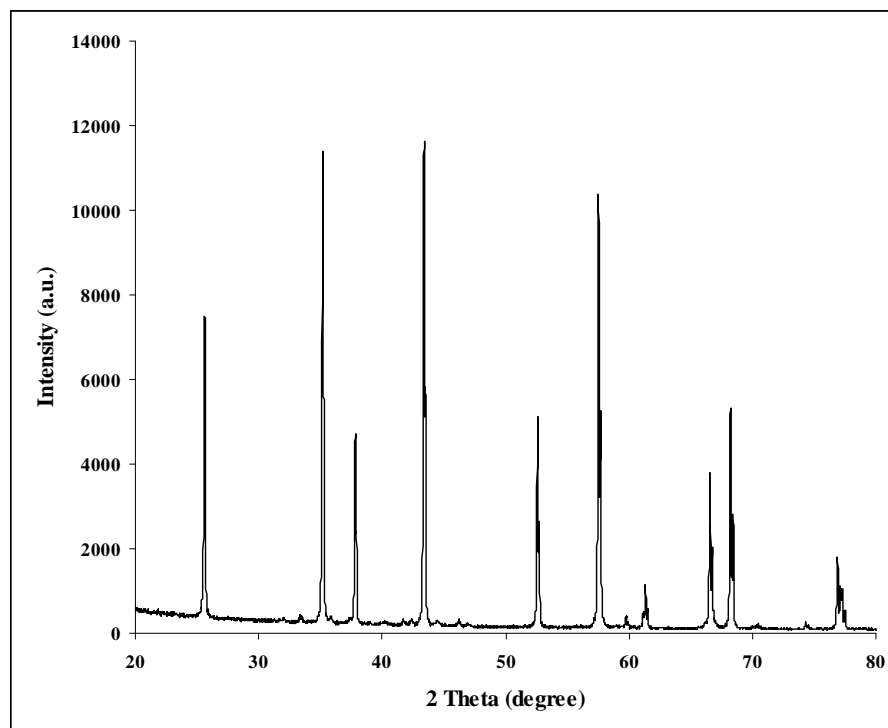
Figure 23 X-ray diffraction patterns of α-Al_2O_3 calcined at $1200^\circ C$.

To determine the full width at half maximum intensity (FWHM or β_s), the observed peaks at 2θ of 25.61°, 35.18°, 37.81°, 43.38°, 52.58°, and 57.53° have to be expanded and calculated in radian. The FWHM was plotted as a function of diffraction angle (2θ). The data of FWHM, β_s of standard Al_2O_3 at 2θ of 25.61°, 35.18°, 37.81°, 43.38°, 52.58°, and 57.53° are summarized in Table 4.

Table 4 Instrument broadening (FWHM, β_s).

2Theta	FWHM β_s (2Theta)	FWHM β_s (radian)
25.61	0.111	0.00194
35.18	0.108	0.00189
37.81	0.109	0.00190
43.38	0.110	0.00192
52.58	0.112	0.00195
57.53	0.111	0.00207
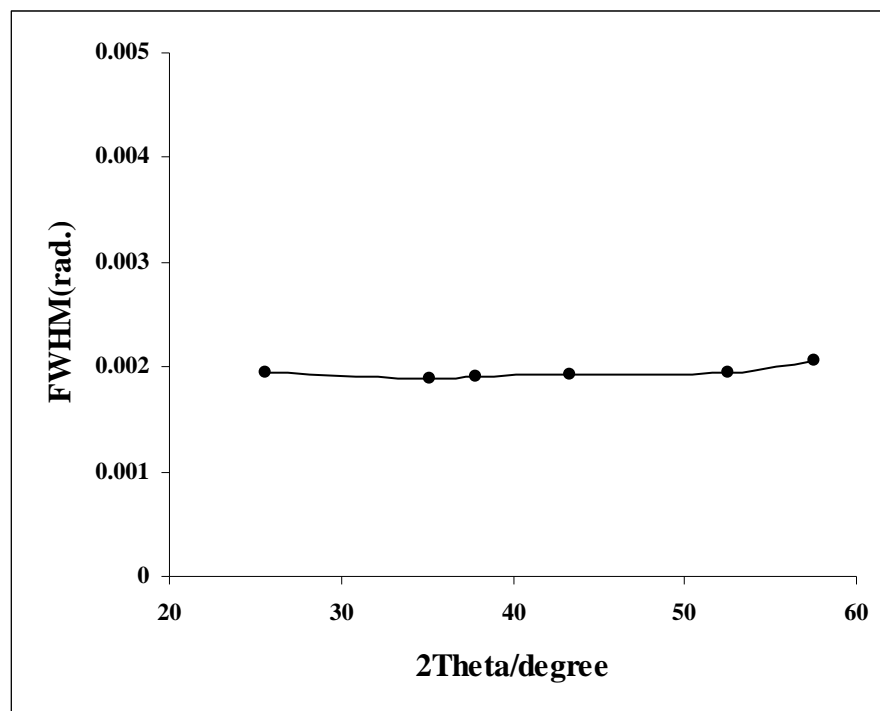
Figure 24 Calibration curve for determination of instrumental broadening.

From Figure 24, the instrumental broadening (β_s) of LaCoO$_3$-ss (1:1) was 0.0020 radian.

where $\beta_s = 0.0020e^{-0.0008 \times 2\theta}$

- Determination of β_m

        The highest intensity peak at 2θ of $32.94°$ was splitted; β_m could not determined. In this study, the characteristic peak of $LaCoO_3$-ss (1:1) at the second highest intensity diffraction peak of $47.54°$ was expanded and β_m was evaluated to be 0.0027 radian.

- Determination of β according to the Warren equation (Equation 18).

$$\beta = \sqrt{0.0073^2 - 0.0020^2}$$

$$= 0.007020 \text{ radian}$$

- Determination of particle size by substitute β of 0.001813 radian into Scherrer's equation (Equation 16).

$$D = \frac{0.9(1.54)}{0.007020[\cos(\frac{47.57 \times \pi}{2 \times 180})]}$$

$$= 197.5 \text{ Å}$$

$$= 19.7 \text{ nm}$$

        By using Scherrer's equation (Equation 17), the crystallite sizes of the calcined $LaCoO_3$-ss (1:1, high La and high Co) powders at 700, 800, 850, and $900°C$ were calculated and shown in Table 5. As increasing the calcination temperature, the crystallite size was increased from 19.7 nm to 216.6 nm and 46.2 nm to 74.7 nm for $LaCoO_3$-ss (1:1 and high La), respectively. The crystallite sizes of $LaCoO_3$-ss (high Co) were 20.2 nm, and as increasing temperature, the crystallite size was varied between 42.3 and 47.4 nm.

Table 5 Crystallite sizes of $LaCoO_3$-ss (1:1, high Co, and high La) perovskites.

Perovskite	Calcination temperature ($^{\circ}$C)	Crystallite size (nm)
$LaCoO_3$ -ss (1:1)	700	19.7
	800	76.5
	850	122.1
	900	216.6
$LaCoO_3$ -ss (high Co)	700	20.2
	800	45.5
	850	42.3
	900	47.4
$LaCoO_3$ - ss (high La)	700	46.2
	800	72.4
	850	73.2
	900	74.7

Figure 25 showed the graph of $LaCoO_3$-ss (1:1, high Co and high La). The crystallite sizes of $LaCoO_3$-ss (1:1) was increased with increasing the calcination temperature. The crystallite sizes of $LaCoO_3$-ss (high Co and high La) were slightly increased with increasing calcination temperature.
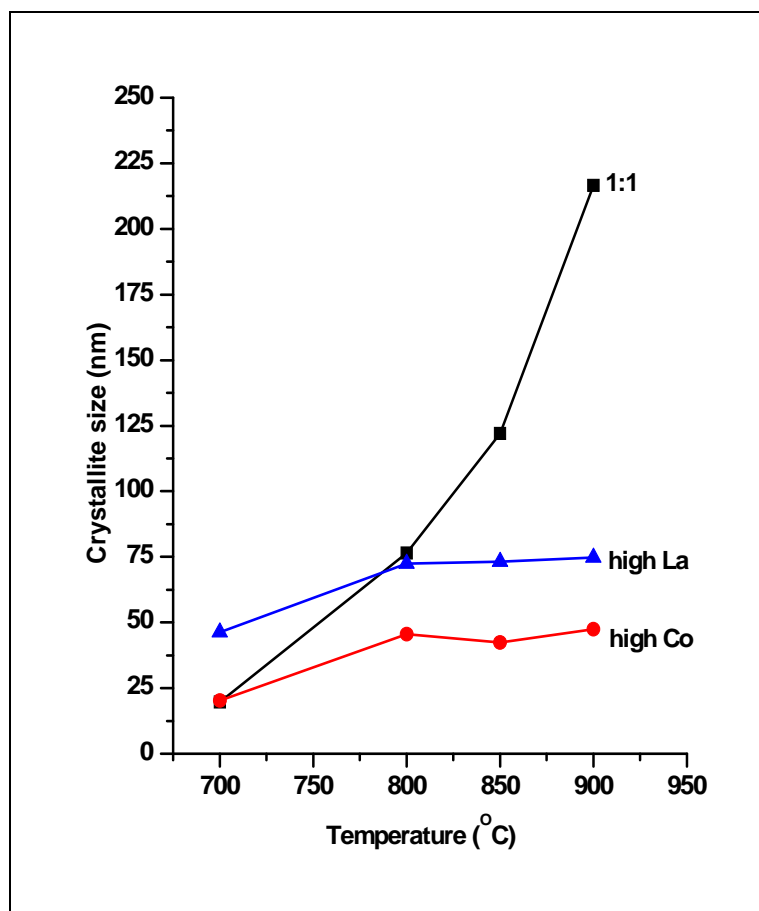
Figure 25 The LaCoO$_3$-ss (1:1, high Co, and high La) crystallite size with
temperature.

Table 6 Crystallite sizes of LaCoO$_3$-cp and LaCoO$_3$-wd perovskites.

Perovskite	Calcination temperature (°C)	Crystallite size (nm)
LaCoO$_3$-cp	700	28.2
LaCoO$_3$-wd	700	28.5

The crystallite sizes of LaCoO$_3$ perovskite from other two methods of LaCoO$_3$-cp and LaCoO$_3$-wd were shown in Table 6. The crystallite sizes of LaCoO$_3$-cp and LaCoO$_3$-wd were 28.2 and 28.5 nm, respectively, at calcination temperature of 700°C. From the results in Tables 5 and 6, the crystallite sizes of all LaCoO$_3$ perovskites were in the order of nanometer and the sizes were dependent on the calcination temperature and the method of preparation.

1.2 X-ray absorption near-edge structure (XANES)

The XANES measurement at Co K-edge were done for LaCoO$_3$-ss (1:1, high Co, and high La), LaCoO$_3$-cp and LaCoO$_3$-wd and Co-foil, CoO and Co$_3$O$_4$ as were used reference samples. The XANES data were analyzed by the ATHENA program and the spectra had been normalized to unity at 100 eV above the edge. The edge absorption occurred when the energy of the incident photons was just sufficient to cause excitation of a core electron of the absorbing atom to a continuum state, i.e. to produce a photoelectron. Thus, the energies of the absorbed radiation at these edges corresponded to the binding energies of electron in the K, L, M, etc, shells of the absorbing elements. The K-edge absorption process occurred due to transition of electron from s-symmetric state to d-symmetric unoccupied states. Thus Co K-edge absorption could be identified to the electronic transition from Co 1s to 3d states (Haas *et al*., 2004).
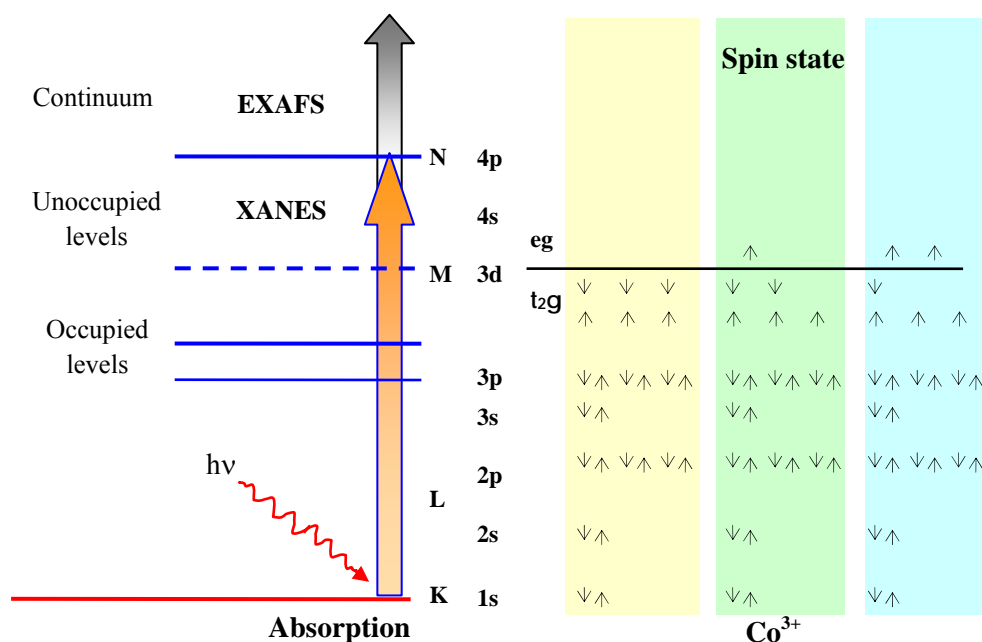
Figure 26 Molecular orbital scheme of Co(III) and possible XAS transitions.

Source: Adapted from Haas (2004)

Figure 26 showed the low-spin, intermediate-spin, and high-spin electron configuration of Co (III) schematically, together with the main K-edge, which in our energy calibrated XANES spectrum with $LaCoO_3$ showed the edge at 7724.0 eV. Octahedral oxygen coordinated Co(III) compounds normally had an undistorted cubic symmetry with a low-spin $\pi^*(t_2g^6)$ configuration, albeit that ligand-to-metal charge transfer processes might formally lead to configurations with seven electrons on the cobalt and a ligand hole $\pi^*(t_2g^6 \, eg^1)$ as well. This was especially true for strong covalent bonds between the cobalt and the ligands. As an exception to the normal case $LaCoO_3$ was either in an intermediate, $t_2g^5 \, eg^1$, or partially in a high-spin state, $t_2g^4 \, eg^2$ (Haas *et al*., 2004).
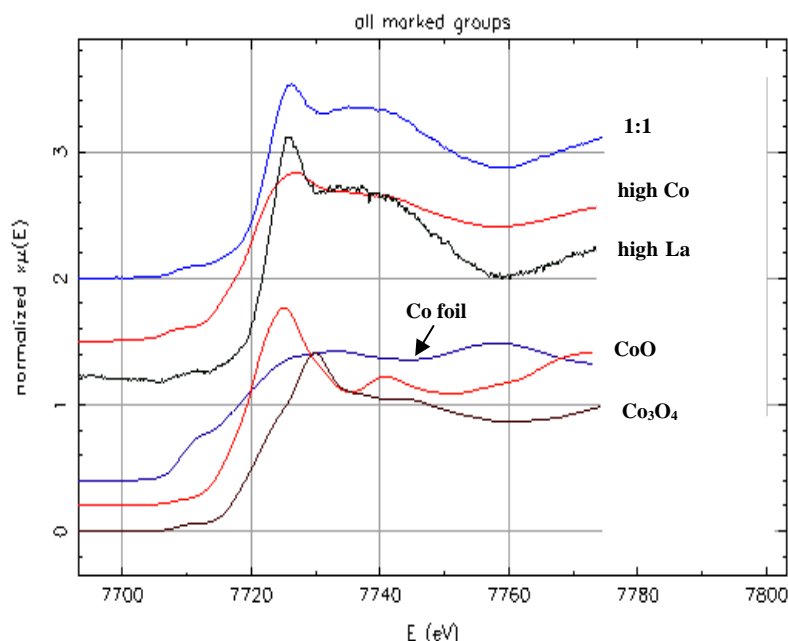
Figure 27 Normalized absorption spectra for the LaCoO$_3$-ss (1:1, high Co, and high
La) and reference sample of Co, CoO, and Co$_3$O$_4$ at Co K edge.

Figure 27 showed normalized XANES spectra of LaCoO$_3$-ss (1:1, high
Co, and high La) calcination at 850°C and XANES from standard Co-foil, CoO, and
Co$_3$O$_4$ as the references. The valence state of Co could be estimated from the location
of the edge (edge energies given in the Table 7). For the LaCoO$_3$-ss (1:1) and
LaCoO$_3$-ss (high La) having the edge position of approximately 7723 eV, the average
Co oxidation state could be $\approx$ 3, confirmed by the peak edge energy of LaCoO$_3$
7723.6 eV (Makshina *et al*., 2006). The XANES pattern of the LaCoO$_3$-ss (high Co)
having the edge energy of 7720.9 eV was between the edge energies of 7720.5 eV and
7721.5 eV from CoO and Co$_3$O$_4$, respectively, which indicated that the average
oxidation state of LaCoO$_3$-ss (high Co) was from 2 to 8/3.
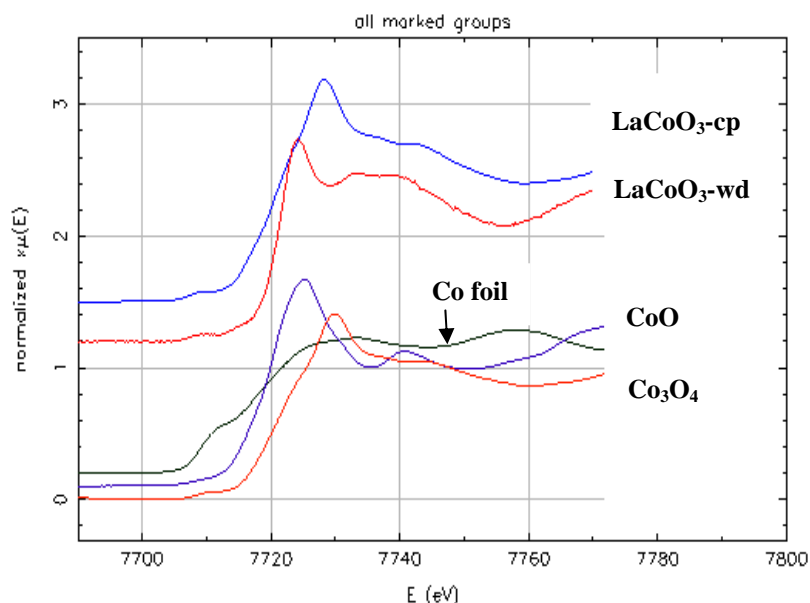
Figure 28 Normalized absorption spectra for the $LaCoO_3$-cp, $LaCoO_3$-wd, and reference sample of Co, CoO, and Co_3O_4 at Co K edge.

For the $LaCoO_3$-cp and $LaCoO_3$-wd, the XANES spectra were shown in Figure 28. The peak edge energy for $LaCoO_3$-cp was 7720.8 eV, giving an average Co oxidation state closed to 2. For the $LaCoO_3$-wd peak edge energy of 7722.0 eV, an average Co oxidation was between 2 and 3. From the XANES edge energy of all $LaCoO_3$ samples were summarized in the Table 7.

Table 7 Edge energy of LaCoO$_3$-ss (1:1, high Co, and high La), LaCoO$_3$-cp, and
LaCoO$_3$- wd perovskites.

Reference[*]	Edge energy (eV)	Sample (experiment)	Edge energy (eV)
Co-foil	7709.0	LaCoO$_3$-ss (1:1)	7723.1
CoO	7720.5	LaCoO$_3$-ss (high Co)	7720.9
Co$_3$O$_4$	7721.5	LaCoO$_3$-ss (high La)	7723.8
LaCoO$_3$	7723.6	LaCoO$_3$-cp	7720.8
		LaCoO$_3$-wd	7722.0

[*]Reference from Makshina *et al* .,(2006)

From the result of edge energy in the Table 7, the LaCoO$_3$-ss (1:1 and high La) had the higher oxidation state than ones from LaCoO$_3$-wd, LaCoO$_3$-ss (high Co), and LaCoO$_3$-cp.

1.3 BET method

Determination of surface area by BET method

Surface area of LaCoO$_3$-ss (1:1, high Co and high La) was derived from N$_2$ adsorption-desorption isotherm as shown in Table 8. In BET measurement, the samples were outgased at 300°C for 3 hours.

Table 8 Surface area of $LaCoO_3$-ss (1:1, high Co and high La) perovskite.

Calcination temperature($^\circ$C)	Surface area (m^2/g)
$LaCoO_3$-ss (1:1)	
700	14.1
800	4.0
850	1.6
900	1.3
$LaCoO_3$-ss (high Co)	
700	8.2
800	3.0
850	3.9
900	1.7
$LaCoO_3$-ss (high La)	
700	8.2
800	4.9
850	5.2
900	4.5

The surface area of $LaCoO_3$-ss (1:1) calcined at 700, 800, 850, and 900°C were 14.1, 4.0, 1.6 and 1.3 m^2/g, respectively. When the temperature of calcination increased, the surface area tended to decrease and gradually dropped at the

temperature of calcination at 900°C as shown in Figure 29. The surface area of LaCoO$_3$-ss (high Co) calcined at 700, 800, 850 and 900°C were 8.2, 3.0, 3.9, and 1.7 m^2/g, respectively. The surface area of LaCoO$_3$-ss (high La) calcined at 700, 800, 850, and 900°C were 8.2, 4.9, 5.2, and 4.5 m^2/g, respectively. The surface area of LaCoO$_3$-ss (high La and high Co) were slightly decreased with increasing calcination temperature as shown in Figure 29.
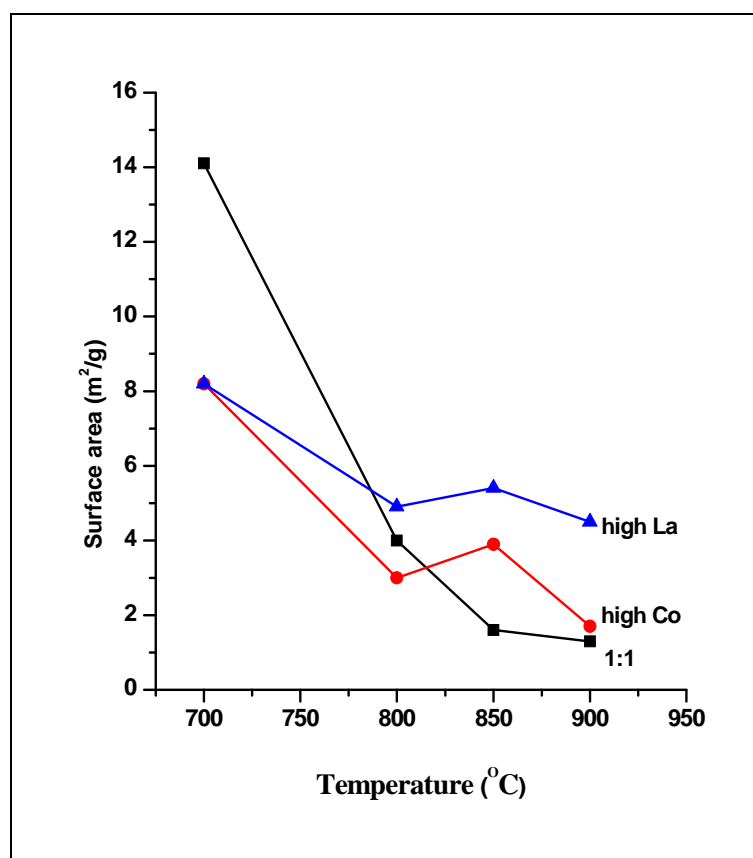
Figure 29 The LaCoO$_3$-ss (1:1, high Co, and high La) surface area with temperature.

1.4 Particles density

The particles density of LaCoO$_3$-ss (1:1, high Co and high La), LaCoO$_3$-cp, and LaCoO$_3$-wd perovskite was determined by using a gas replacement technique. The samples were weighed, put in micro cell, and analyzed by ultrapycnometer 1000

which operated at 23.5°C. The results of apparent density of LaCoO$_3$-ss, LaCoO$_3$-cp, and LaCoO$_3$-wd samples were shown in Table 9.

Table 9 The results of apparent density of LaCoO$_3$ perovskites.

Perovskite	Apparent density (g/cc)
LaCoO$_3$-ss (1:1)	7.2068
LaCoO$_3$-ss (high Co)	6.9848
LaCoO$_3$-ss (highLa)	5.8038
LaCoO$_3$-cp	7.7885
LaCoO$_3$-wd	6.4712

The LaCoO$_3$-ss (high La) showed the lowest density of 5.8038 g/cc, whereas the LaCoO$_3$-ss (1:1 and high Co), LaCoO$_3$-cp and LaCoO$_3$-wd perovskites showed the apparent densities of 7.2068, 6.9848, 7.7885, and 6.4712 g/cc, respectively.

1.5 Scanning electron microscope (SEM)

For the morphology investigation by SEM, the images of LaCoO$_3$-ss (1:1, high Co and high La) showed the aggregation of particles. From Figures 30-32, the SEM image indicated the aggregated particles of the calcined LaCoO$_3$-ss (1:1, high Co, and high La) at 850°C with the size of approximately 4.4, 0.8 and 1.2 μm, respectively.
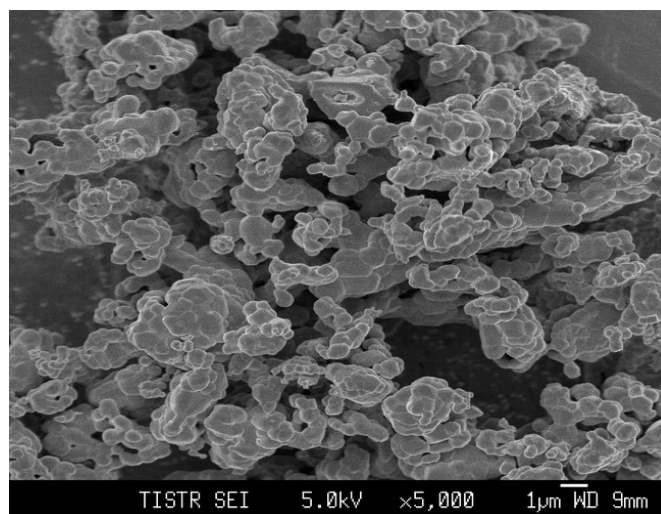
Figure 30 SEM image of LaCoO$_3$-ss (1:1) particle calcined at 850°C.
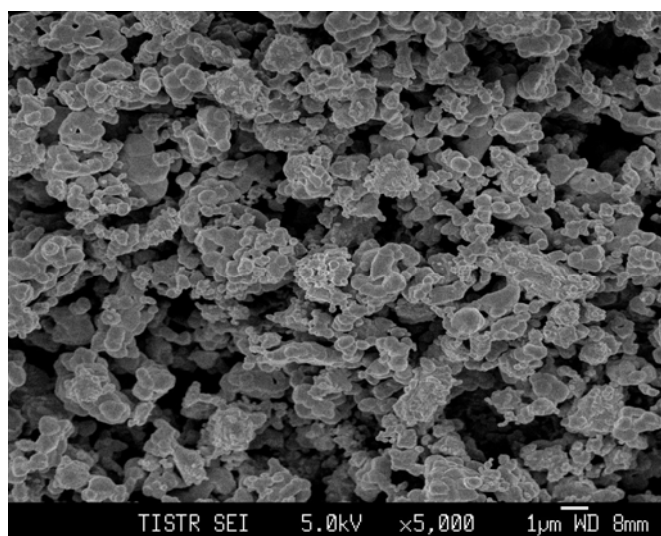
Figure 31 SEM image of LaCoO$_3$-ss (high Co) particle calcined at 850°C.
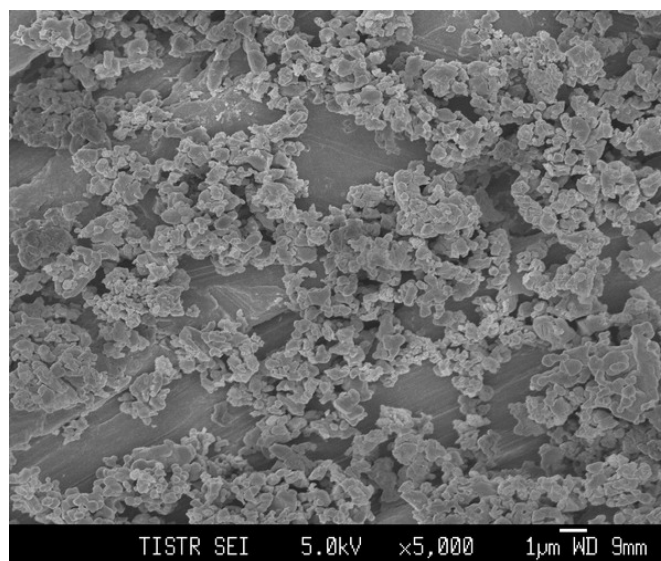
Figure 32 SEM image of LaCoO$_3$-ss (high La) particle calcined at 850°C.
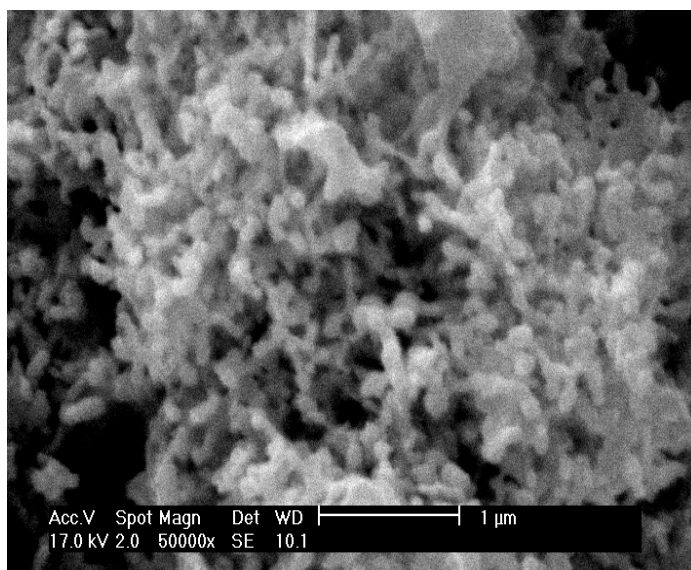
Figure 33 SEM image of LaCoO$_3$-cp particle calcined at 700°C
(Prangsri-aroon 2008).
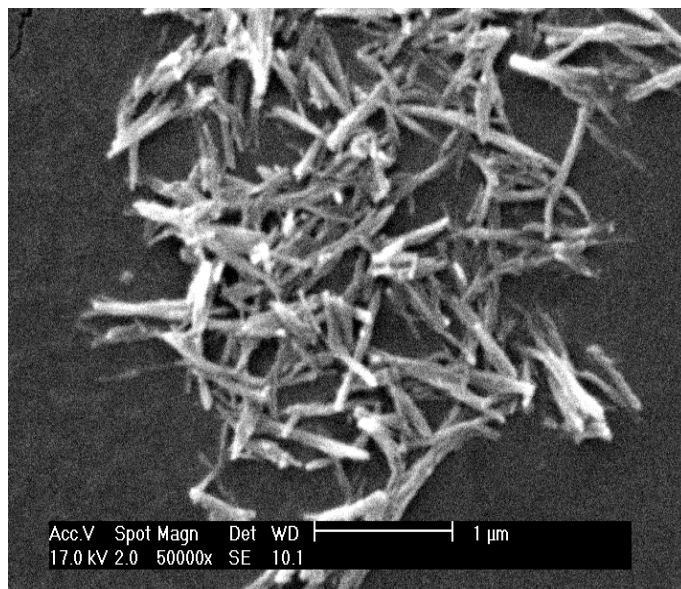
Figure 34 SEM image of LaCoO$_3$-wd particle calcined at 700°C
(Prangsri-aroon 2008).

The morphology of LaCoO$_3$-cp and LaCoO$_3$-wd before calcination was investigated by SEM as shown in Figures 33 and 34, respectively. The scanning electron micrographs revealed the aggregates of LaCoO$_3$-cp consisting of particles in the diameter in range of 90-260 nm. For LaCoO$_3$-wd, the result showed the dispersed rods with the diameter of 70-90 nm and the length of 170-440 nm. SEM images confirmed that the morphology strongly depended on the preparation method (Prangsri-aroon 2008).

2. Carbon monoxide (CO) sensor test

The studies on CO sensors prepared from solid state reaction, modified wet powder dispersion, and co-precipitation methods could be summarized as shown in the following diagram.
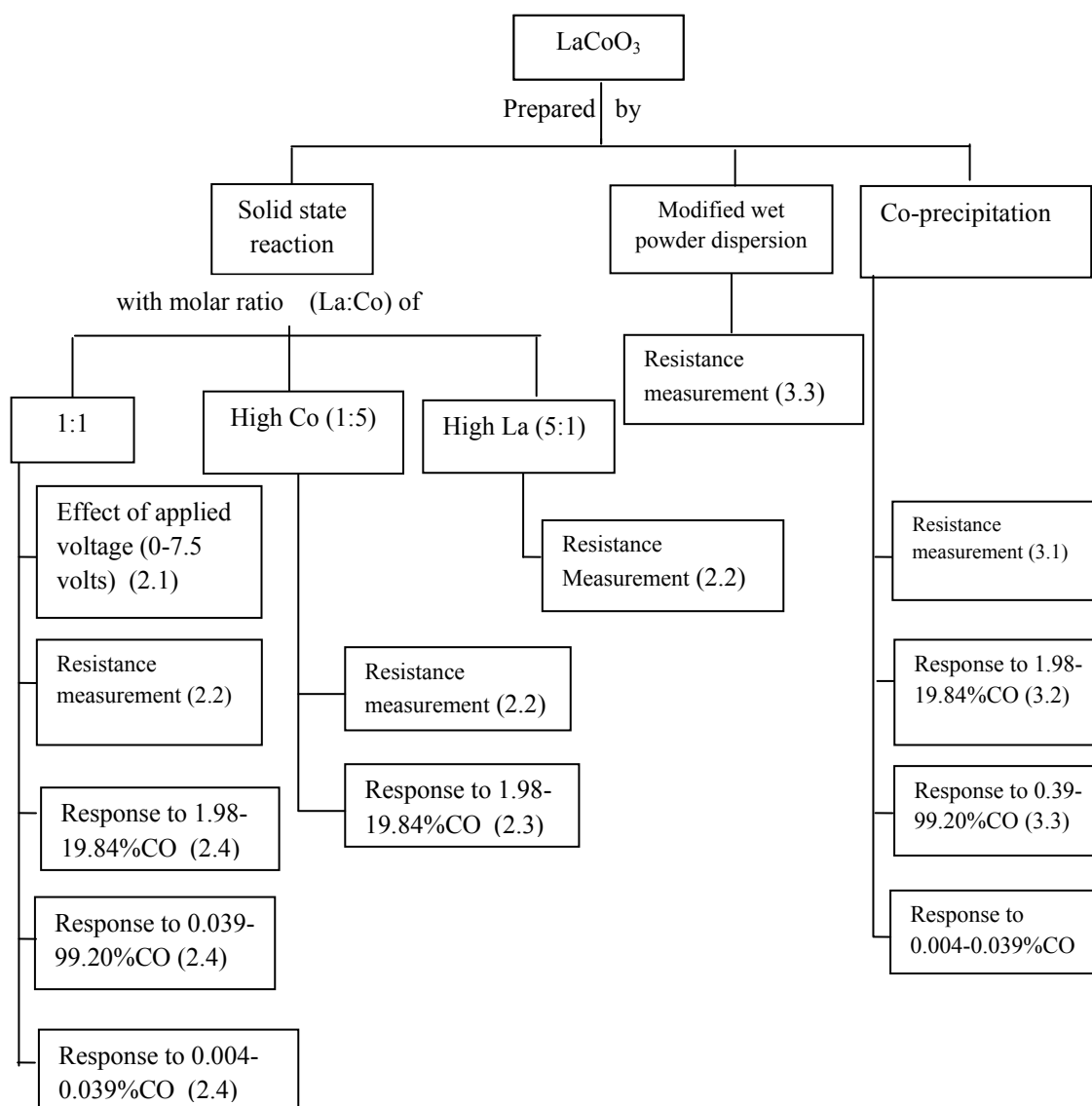
[( ) represents the corresponding section in Results and Discussion]

Figure 35 Diagram for LaCoO$_3$ CO sensing.

2.1 The effect of applied voltage on the resistance of LaCoO₃-ss (molar ratio (La:Co) of 1:1)

The voltages of 0.0 volt to 7.5 volts, corresponded to temperature of 29°C to 133°C measured at the LaCoO₃ surface, were applied to LaCoO₃ and the resistance was investigated on the change with temperature. At 7.5 volts, the resistance was lowest (highest conductivity). At temperature above 0 K (-273°C), some of the valence electrons were thermally activated and excited across the energy band gap into the conduction band; electron hole pairs were generated. The conductivities of semiconductors increased with increasing temperatures for the temperature range over which this process predominated; the quantity of thermally activated electrons in semiconductor was temperature dependent.   The amount of electrons having the sufficient thermal energy to jump to the conduction band would produce the same amount of holes in the valence band; the concentration of these electrons depended on energy band gap and temperature (William *et al*., 1990).
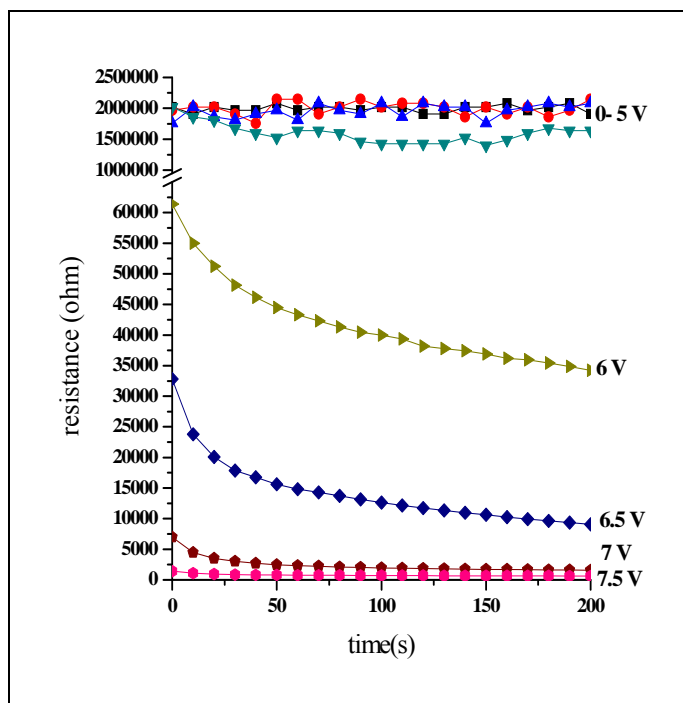
Figure 36 The resistances with time of the LaCoO₃-ss (1:1) at 850°C with 0-7.5 volts applied.

2.2 The response of different molar ratio (La:Co) sensors in oxygen atmosphere at different operating temperatures

The LaCoO$_3$ prepared from solid state reaction had the molar ratio (La:Co) of 1:1, 1:5 (high Co), and 5:1 (high La). These three sensors response to oxygen were investigated as shown in Figures 37-39.
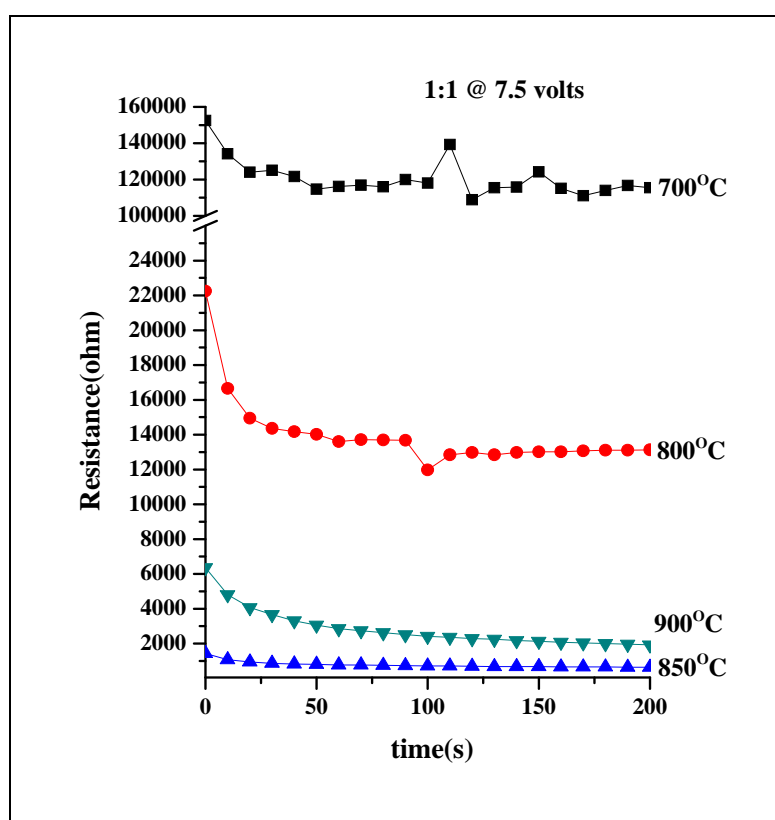
Figure 37 The resistances with time of the LaCoO$_3$-ss (1:1) calcined at 700, 800, 850, and 900°C with the applied voltage of 7.5 volts.

From Figure 37, the measured resistances with time for LaCoO$_3$-ss (1:1) of various calcination temperatures of 700, 800, 850 and 900°C were shown. The resistance for all LaCoO$_3$-ss (1:1) sensors decreased exponentially to the lowest resistance of approximate 1000 Ω for one at calcination temperature of 850°C and to the highest of 1.2 MΩ for the one at calcination temperature of 700°C. As the

calcination temperature increased, LaCoO$_3$ and Co$_3$O$_4$ reacted to form LaCoO$_3$ as shown in XRD patterns (Figure 19). The resistance decreased as the LaCoO$_3$ phase was formed during the measuring time of 200s. At the calcination temperature of 850°C, LaCoO$_3$-ss (1:1) showed the lowest resistance or highest conductivity. It implied that high number of valence electrons in the valence band were excited to the conduction band and created holes in the valence band. By looking at the structure, the prepared LaCoO$_3$-ss (1:1) after calcination at 850°C might have the approximate structure of rhombohedral for high conductivity. The result indicated that the high conductivity of LaCoO$_3$ was due to the phase of LaCoO$_3$.
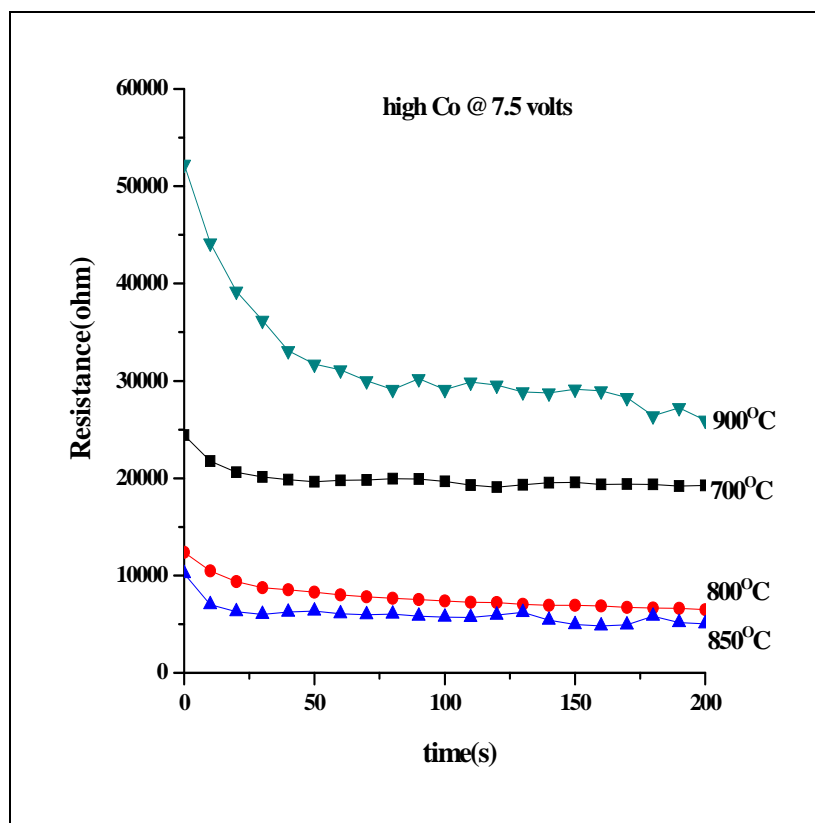
Figure 38 The resistance with time of LaCoO$_3$-ss (high Co) calcined at 700, 800, 850, and 900°C with the applied voltage of 7.5 volts.

Figure 38 showed the resistance of LaCoO$_3$-ss (high Co) calcined at 700-900°C which were approximately 30 kΩ for one calcined at 900°C and to 5000 Ω for

the one calcined at 850°C. As increasing calcination temperature from 700°C to 850°C, the resistance was decreased. However, when it was continued increasing the calcination temperature to 900°C, the resistance was highly increased.

As the calcination temperature increased to 850°C, the phase of $LaCoO_3$ in $LaCoO_3$-ss (high Co) increased, confirmed by XRD (Figure 20), leading to the decrease of resistance or the increase of conductivity. If looking at the change in Co_3O_4 phase, the results showed the decrease of the remaining Co_3O_4 as increasing the calcination temperature, which was resulted from the use of Co_3O_4 in $LaCoO_3$ formation. The Co_3O_4 could possibly undergo oxidation or reduction at the $LaCoO_3$ surface. However, the presence of Co_3O_4 with $LaCoO_3$ made the resistance decrease to approximate 5000 Ω for $LaCoO_3$-ss (high Co) at the calcination temperature of 850°C, which was higher than the resistance of 1000 Ω for $LaCoO_3$-ss (1:1) at the same calcination temperature.

As increasing the calcination temperature to 900°C, although the phase of $LaCoO_3$ was increased, the surface area was decreased by half indicating the decrease in porosity. The high resistance of $LaCoO_3$-ss (high Co) at the calcination temperature of 900°C implied that not only the presence of $LaCoO_3$ and Co_3O_4 but also the surface area/porosity had the influence on the resistance.
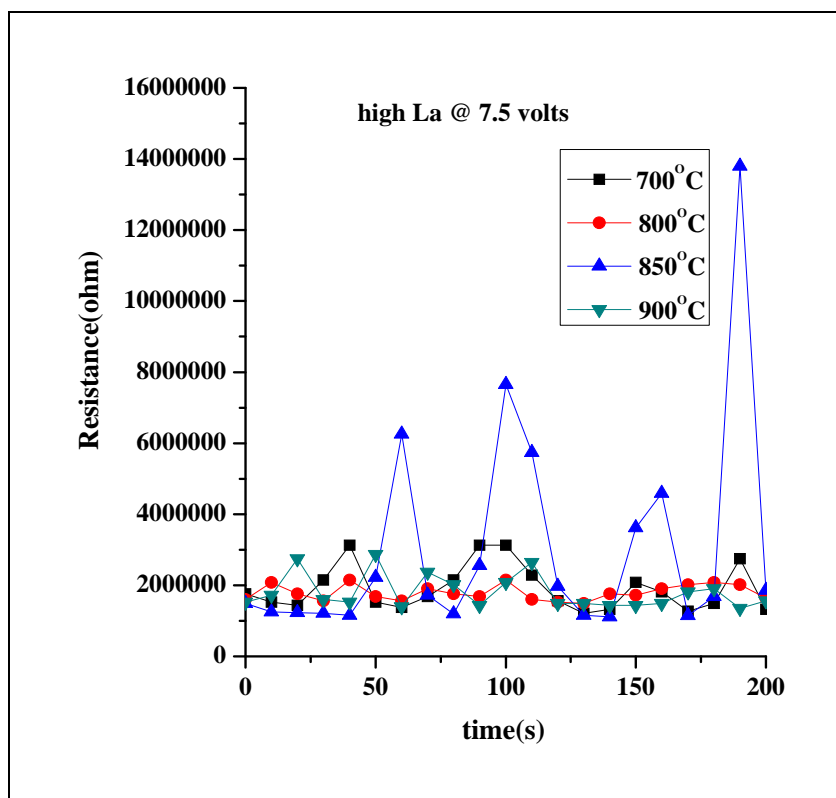
Figure 39 The resistance with time of LaCoO$_3$-ss (high La) calcined at 700, 800, 850, and 900°C with the applied voltage of 7.5 volts.

As shown in Figure 39, the measured resistance of LaCoO$_3$-ss (high La) calcined at 700, 800, 850 and 900°C was presented. LaCoO$_3$-ss of high La had highest resistance compared to those of LaCoO$_3$-ss (1:1, and high Co). As increasing the calcination temperature, the phase of Co$_3$O$_4$ and the remaining La$_2$O$_3$ were decreased due to the formation of LaCoO$_3$ phase as shown in the XRD patterns from Figure 21. Although the phase of LaCoO$_3$ was increased, the resistance of LaCoO$_3$-ss (high La) was as high as approximate 2 MΩ and fluctuated.

The electrical conductivity of materials was usually related to their morphology, the surface area, the particle size and the pore size. The micropore volume of the LaCoO$_3$ could play an important role on the resistance of LaCoO$_3$. The micropore volume of LaCoO$_3$-ss (high La) is 5×10^{-5} which was higher when compared to 0 of those LaCoO$_3$-ss (high Co and 1:1). Having micropores, the

structure consisting of smaller and deeper pores, may cause the higher resistance due to the difficulty of the ions to move or transfer (Frackwiak et al., 2001). The results implied that the presence of excess La_2O_3 might be the cause of the micropore structure and high resistance. When compared to $LaCoO_3$-ss (1:1 and high Co), $LaCoO_3$-ss (high La) showed highest resistance or lowest conductivity which indicated the inappropriate use for CO sensor in the further studies.

2.3 The response of $LaCoO_3$-ss (1:1 and high Co) to CO.

$LaCoO_3$ is a p-type semiconductor. The resistance of a sensor based on p-type semiconducting materials in air containing reducing gases was higher than that in pure air, so the sensitivity was defined as follows:

$$S \;=\; R/R_0 \tag{19}$$

Where S was the sensitivity, R and R_0 were resistance of a sensor in air containing reducing gases and in pure air, respectively, at the same temperature. The sensitivity of sensor increased with increasing operating temperature or applied voltage (Kong et $al.,$ 1996).

General speaking, semiconductor could be classified according to their electron donor or acceptor levels as follows (Ling et al., 1995).

Table 10 Resistance for semiconductor (Adapted from Ling 1995).

Semiconductor	Oxidizing condition, Oxygen added	Reducing condition, Oxygen reduced
p-type	Resistance falls	Resistance rises
n-type	Resistance rises	Resistance falls

The sensitivity (R/R_0) vs. times of the $LaCoO_3$-ss (1:1 and high Co) sensor were shown in Figures 40-41. Both sensors were tested with CO gas with the concentrations of 1.98, 5.95, 9.92, 13.89, and 19.84% v/v using the applied voltage of 7.5 volts.
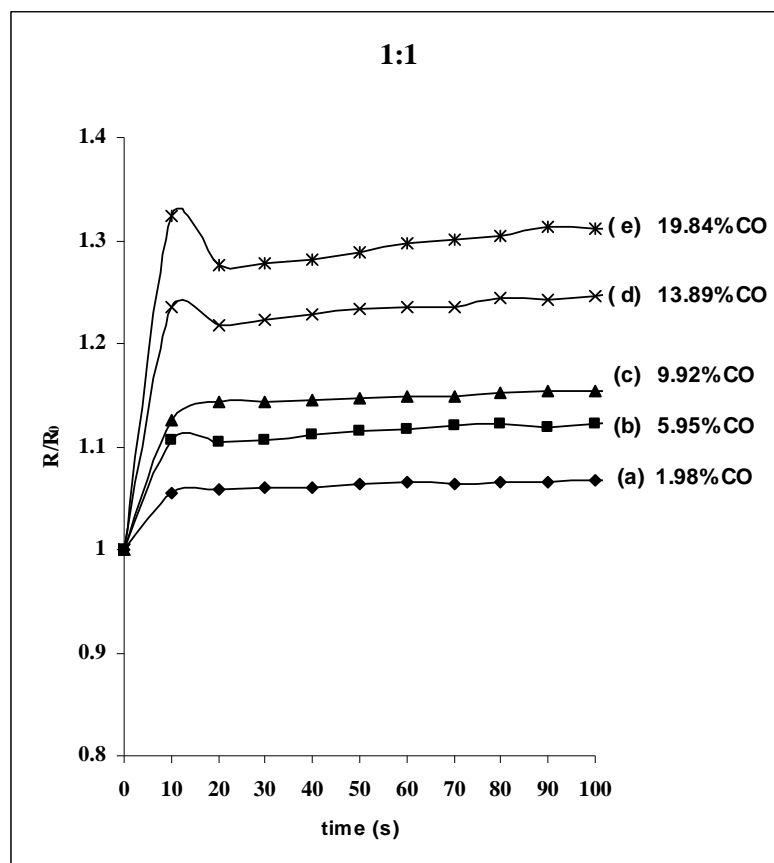
Figure 40 The sensitivity (R/R_0) of $LaCoO_3$-ss (1:1) with time on exposing to CO
concentrations of 1.98-19.84% v/v.

Figure 40 showed that the sensitivity (R/R_0) of $LaCoO_3$-ss (1:1) sensor was increased with increasing CO concentrations. The response time was about 20s when the resistance was stable due to complete CO oxidation. Oxygen gas was purged through the sensor chamber, before the gas sample was introduced, to supply the surface oxygen of the $LaCoO_3$-ss (1:1) perovskite.

It was well known that CO was a reducing agent and reacted with adsorbed oxygen to form CO_2. Here, rates of the reaction would be controlled by the rate of desorption of CO_2 from the surface. One of the simplified reaction scheme could be highlighted as below (Salker *et al.*, 2005).

$$S_{(s)} + \frac{1}{2} O_{2(g)} \longrightarrow S...O^-_{(ad)} \tag{20}$$

$$S_{(s')} + CO_{2(g)} \longrightarrow S...CO^+_{(ad)} \tag{21}$$

$$S...O^-_{(ad)} + S...CO^+_{(ad)} \longrightarrow S...CO_{2(ad)} + S_{(s)} \tag{22}$$
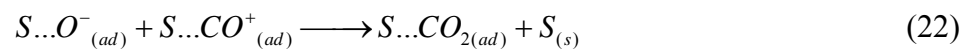
Where S was metal oxide site on the surface, (s) and (s´) represented active site on the surface for oxygen and CO adsorption, (g) and (ad) were shown as gas and adsorbed form (Isupova *et al*., 2000).

According to equations 20-22, the mechanism on active site of $LaCoO_3$ could be written as shown in equations 23-25. The active site of $LaCoO_3$ perovskite was Co^{3+}, which was capable for receiving electrons. It had been shown that cobalt on the surface was usually in the +3 oxidation state.

$$LaCoO_{3(s)} + \frac{1}{2} O_{2(g)} \longrightarrow LaCoO_3...O^-_{(ad)} \tag{23}$$

$$LaCoO_{3(s')} + CO_{2(g)} \longrightarrow LaCoO_3...CO^+_{(ad)} \tag{24}$$

$$LaCoO_3...O^-_{(ad)} + LaCoO_3...CO^+_{(ad)} \longrightarrow LaCoO_3...CO_{2(ad)} + LaCoO_{3(s)} \tag{25}$$
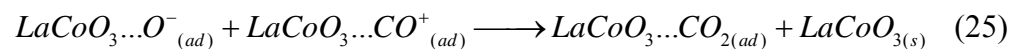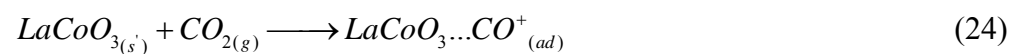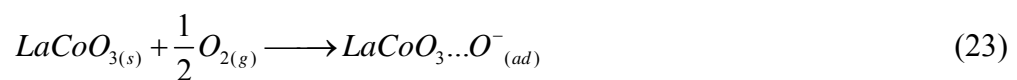
For $LaCoO_3$-ss (high Co), the sensitivity (R/R_0) was fluctuated with time after 20s of measuring time as shown in Figure 41. From the XRD pattern of $LaCoO_3$-ss (high Co), there were the impurity peaks of Co_3O_4, and the XANES pattern indicated that average oxidation state of $LaCoO_3$-ss (high Co) was from 2 to 8/3. Due to the presence of Co_3O_4, the oxidation-reduction of Co_3O_4 site along with

the surface reaction on $LaCoO_3$ site could be resulted in the fluctuation of $LaCoO_3$-ss (high Co) sensitivity.
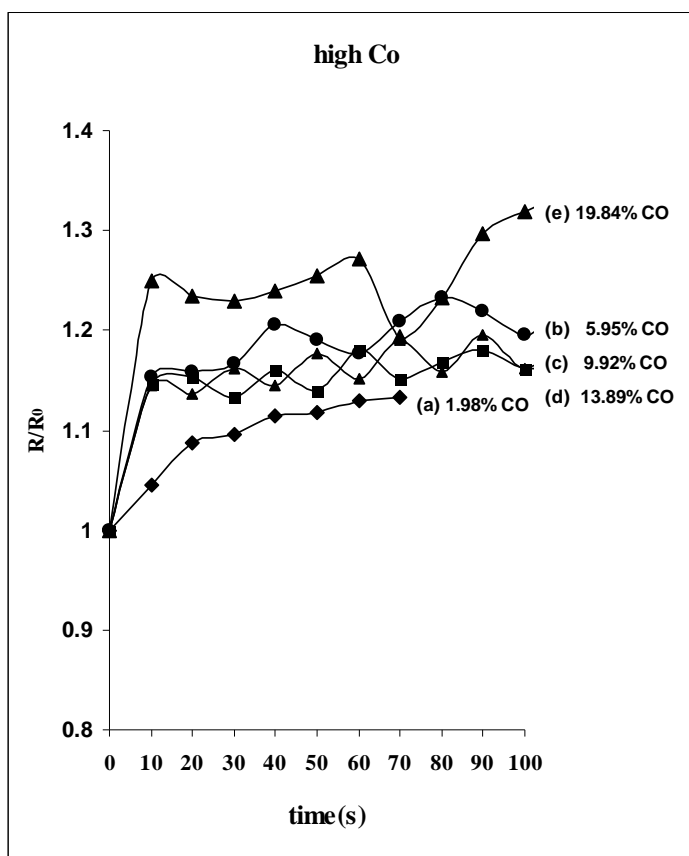
Figure 41 The sensitivity (R/R_0) of $LaCoO_3$-ss (high Co) with time on exposing to CO concentrations of 1.98-19.84% v/v.

Table 11 The sensitivity (R/R_0) of $LaCoO_3$-ss (1:1, high Co, and high La).

CO (ml)	CO (%)	R/R$_0$ 1:1	R/R$_0$ high Co	R/R$_0$ high La
1	1.98	1.06	1.09	N/A
3	5.95	1.10	1.16	N/A
5	9.92	1.14	1.13	N/A
7	13.89	1.22	1.15	N/A
10	19.84	1.28	1.23	N/A

*N/A – could not be measured

For all $LaCoO_3$-ss (1:1, high Co, and high La) samples, the R/R_0 measured for CO concentration of 1.98-19.84% were shown in Table 11. The sensitivity (R/R_0) of $LaCoO_3$-ss (1:1) was slightly increased with the increase of CO concentration. The sensitivity (R/R_0) of $LaCoO_3$-ss (high Co) was increased but fluctuated. For $LaCoO_3$-ss (high La), the resistance was too high (approximate 2 MΩ) and the sensitivity could not be measured.
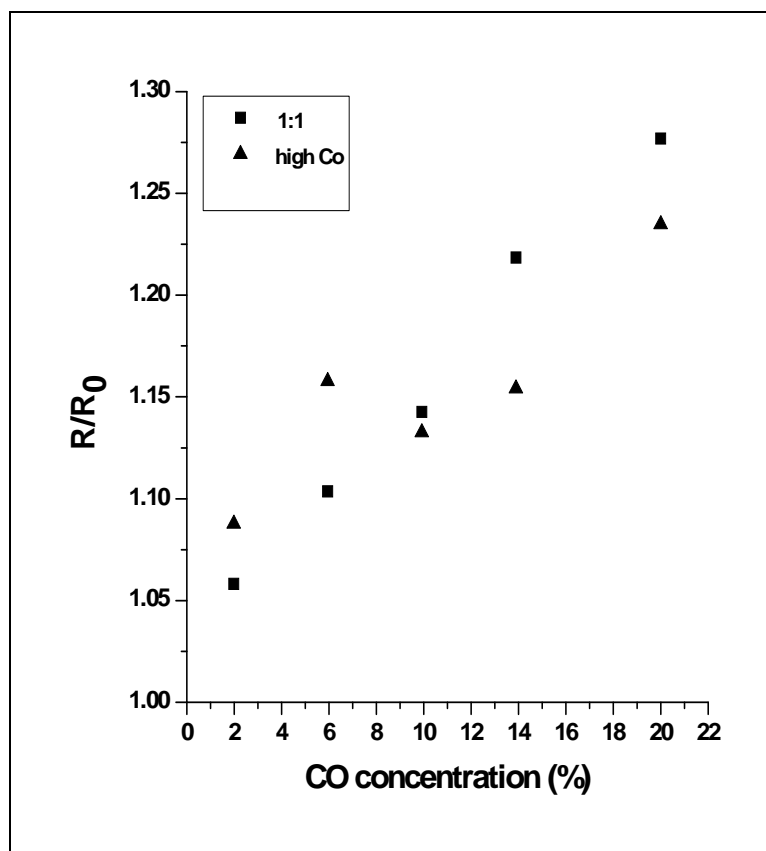
Figure 42 The sensitivity and the CO concentrations of LaCoO$_3$-ss (1:1 and high Co) to 19.84% v/v at 20s.

Figure 42 showed the sensitivity (R/R$_0$) at 20 seconds on various CO concentrations for LaCoO$_3$-ss (1:1 and high Co) sensors. From the plot, the sensitivity (R/R$_0$) of LaCoO$_3$-ss (1:1) was linearly fit to 19.84% v/v CO. For LaCoO$_3$-ss (high Co), the sensitivity (R/R$_0$) was non-linear with CO concentration resulting from the resistance fluctuation as shown in Figure 41.

2.3 Study of the quantification range of CO sensing

For the LaCoO$_3$-ss (1:1), the best operating temperature for CO gas was 133°C (at applied voltage of 7.5 volts) and the resistance corresponding to CO

concentrations of 0.39-99% v/v were measured after injecting oxygen. The mechanism of oxidation with $LaCoO_3$ p-type semiconductor was presented according to equation 23-25.

Table 12 The sensitivity (R/R_0) of $LaCoO_3$-ss (1:1) at 0.39-99.2% v/v CO.

CO (ml)	CO (%)	R/R_0
0.2	0.39	1.05
0.4	0.79	1.09
0.6	1.19	1.11
0.8	1.58	1.13
1	1.98	1.17
2	3.96	1.22
5	9.92	1.51
10	19.84	1.55
15	29.76	1.60
20	38.63	1.78
25	49.60	1.88
30	59.52	1.96
35	69.44	1.99
40	79.36	1.85
45	89.28	2.01
50	99.20	1.60

Table 12 showed the sensitivity of $LaCoO_3$-ss (1:1) after injecting CO gas at the concentration of 0.39-99.2% v/v. From Table 12, the sensitivity results of $LaCoO_3$-ss (1:1) could be plotted showing the relation between R/R_0 and %CO concentration as shown in Figure 43. Figure 43 showed the sensitivity of $LaCoO_3$-ss (1:1) with 0.39-99.20% CO v/v in air. At 0.39-3.96% CO, the sensitivity (R/R_0) were low from 1.05 to 1.22. At 9.92% CO, the sensitivity increased to 1.51. As increasing CO concentration to 69.44%, the response increased slowly with increasing CO concentration and then tented to decrease as the CO concentration went from 69.44% to 99.20%. This dramatically improved sensitivity of $LaCoO_3$-ss (1:1) for CO was due to the oxidation state of Co^{3+}. This could be stated that in the low concentration range (0.39-3.96% CO), the active site (Co^{3+}) were initially vacant, the CO gas could rapidly fill the surface. At 9.92-69.44% CO, the CO gas was also adsorbed on the surface but with competition. In the high concentration range (79.36-99.20% CO), the CO gas approached the active sites which might be fully occupied causing the decrease in sensitivity. The CO_2 product formed at higher CO concentration could be more adsorbed on the sensor surface causing the $LaCoO_3$ to be less active and the rate of the reaction would be controlled by the rate of desorption of CO_2 from the surface (Salker *et al*., 2005).
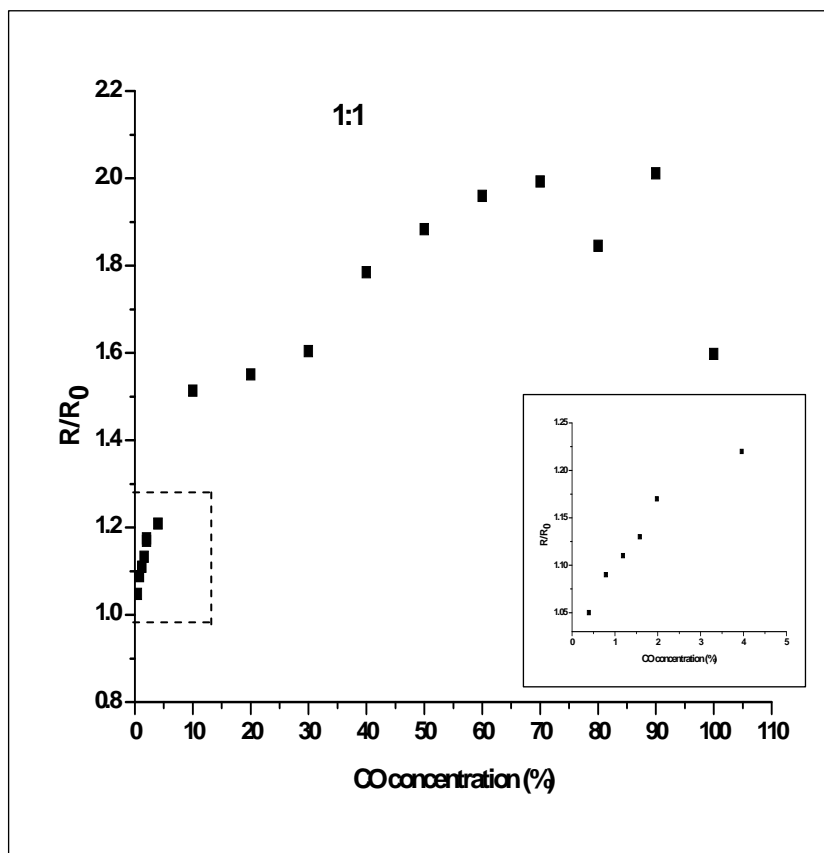
Figure 43 The sensitivity with the CO concentrations of LaCoO$_3$-ss (1:1) 0.39-
99.20% v/v at 20s. The inset represented the enlargement of the
sensitivity with the low CO concentrations of 0.39-3.96% v/v at 20s.

To study the detection limit of LaCoO$_3$-ss (1:1), the experiments were
performed using the low CO concentration of 0.004-0.039% v/v. Table 13 showed
the result of the sensitivity (R/R$_0$) of LaCoO$_3$-ss (1:1), having the sensitivity (R/R$_0$) of
0.977-1.027.

Table 13 The sensitivity (R/R_0) of $LaCoO_3$-ss (1:1) at 0.004-0.039% v/v CO.

CO (ml) (diluted 0.99% CO)	CO (%)	R/R_0
0.2	0.004	0.977
0.3	0.006	1.007
0.4	0.008	1.006
0.6	0.012	1.011
0.8	0.016	1.014
1	0.019	1.015
2	0.039	1.027

From Table 13, the sensitivity results of $LaCoO_3$-ss (1:1) could be plotted showing the relation between R/R_0 and 0.004-0.039% CO concentration at 20s as shown in Figure 44. The detection limit of $LaCoO_3$-ss (1:1) obtained from the graph was about 0.006% v/v (60 ppm). At higher CO concentration, the results showed high sensitivity which fitted to be linear with CO concentration. As increasing CO concentration to 0.039% v/v, the R/R_0 increased; it could be resulted that the active sites (Co^{3+}) were vacant and the number of vacant sites was plentiful for CO adsorption leading to the slightly increase in the sensitivity (R/R_0).
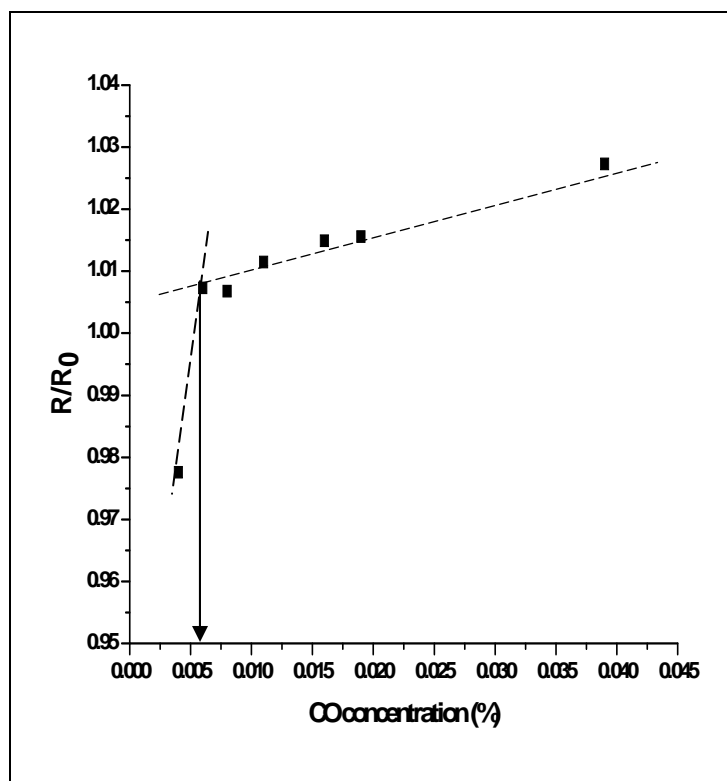
Figure 44 The sensitivity (R/R_0) of LaCoO$_3$-ss (1:1) with the 0.004-0.039 % v/v CO
concentrations at 20s.

Table 14 Chemical and physical properties and CO sensing capability of prepared
LaCoO$_3$-ss perovskite.

Perovskite	Oxidation state	Crystallite size (nm)	Grain size (μm)	Surface area (m^2/g)	Relative density[*] (%)	Density (g/cm^3)	CO sensing
1:1	+3	122.1	4.4	1.6	98.89	7.2068	Good
High Co	+2, +8/3	42.3	0.2	3.9	95.85	6.9848	Medium
High La	+3, +8/3	73.2	1.2	5.2	79.85	5.8038	N/A[**]

[*] relative density to the theoretical density of 7.287 (Appendix Figure B1)

[**] N/A – could not be measured

Table 14 showed the chemical and physical properties as well as CO sensing capability prepared from $LaCoO_3$-ss (1:1, high Co, and high La). $LaCoO_3$-ss (1:1) showed good sensing response than others due to the average Co oxidation number of +3, which was the most active site, although its crystallite and grain sizes were large and its surface area was low. The results showed its high density of 7.2068 g/cm^3 approaching the theoretical density of 7.287 g/cm^3, which indicated that the $LaCoO_3$-ss (1:1) samples were very dense. For $LaCoO_3$-ss (high Co), its sensing response was quite good due to its small crystallite and grain sizes. Because of its Co oxidation state of +2 and +8/3, the Co site was not as active as Co^{3+}. By looking at its relative density of 95.85% theoretical density, the result indicated a small deviation from theoretical density which implied that there was a small amount of Co_3O_4 (density of 6.056 g/cm^3 from Appendix Figure B3) remaining in $LaCoO_3$-ss (high Co). For $LaCoO_3$-ss (high La), the sensing capability was less compared to other $LaCoO_3$-ss perovskites. Although it had small grain size, relatively moderate crystallite size, higher surface area compared to the others, and the oxidation state of +3 and +8/3, its relative density of 79.85% theoretical density indicated that there was high La_2O_3 content (density of 6.574 g/cm^3 from Appendix Figure B2) left in the $LaCoO_3$ phase and the perovskite was porous. The remaining La_2O_3 could be scattered on the surface of $LaCoO_3$-ss (high La) caused the incapability of the sensing characterize in the material.

3. CO responses of $LaCoO_3$-cp prepared by co-precipitation and modified wet powder dispersion method

3.1 The response of $LaCoO_3$-cp and $LaCoO_3$-wd in oxygen at 7.5 volts

Figure 45 showed the relation between the resistance and time of $LaCoO_3$-cp and $LaCoO_3$-wd in oxygen atmosphere at the calcination temperature of $700^{\circ}C$, the results showed that the resistance of $LaCoO_3$-cp was much lower than its of $LaCoO_3$-wd. The low resistance of $LaCoO_3$-cp was approximately 6000 Ω which closed to that of $LaCoO_3$-ss (high Co), whereas the low resistance of $LaCoO_3$-wd was

about 2 MΩ. XRD of both LaCoO$_3$-cp and LaCoO$_3$-ss (high Co) showed Co$_3$O$_4$ as the impurities left on the LaCoO$_3$ surface.
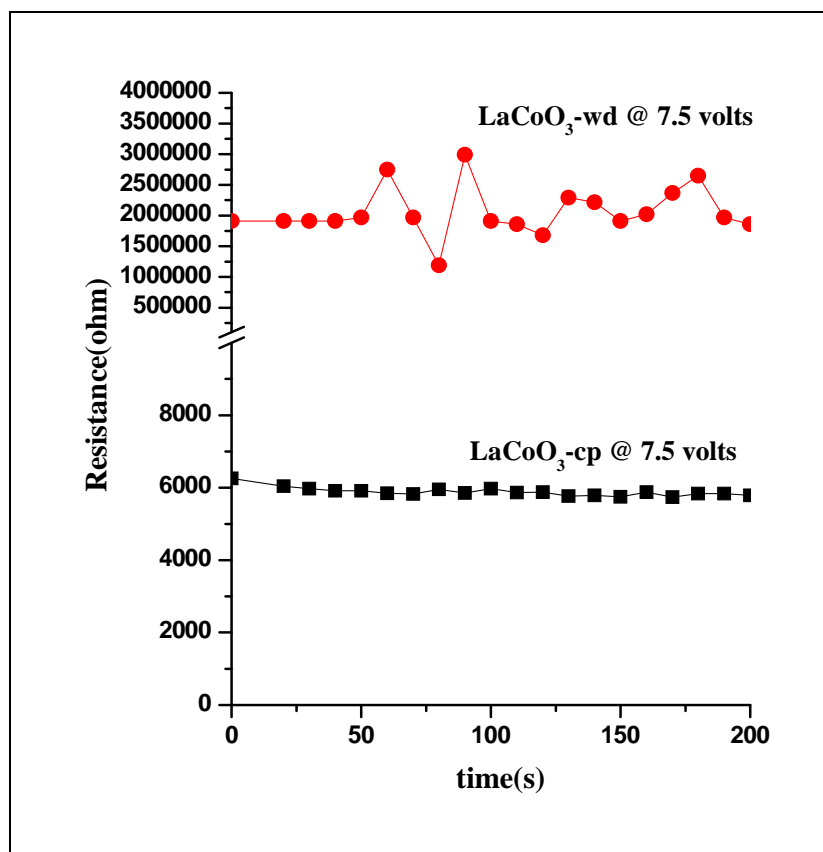
Figure 45 LaCoO$_3$-cp and LaCoO$_3$-wd resistance with time.

The low resistance LaCoO$_3$-cp could be resulted from the surface oxidation state of 2 and 8/3 as shown in the XRD results. From XRD pattern of LaCoO$_3$-cp, the peaks showed the presence of Co$_3$O$_4$ and the active LaCoO$_3$. For LaCoO$_3$-wd, the resistance was very high about 2 MΩ. This could be resulted from the small amount of Co^{3+} in LaCoO$_3$ and the presence of La(OH)$_3$ on surface as shown in the XRD patterns. The high resistance of LaCoO$_3$-wd indicated that LaCoO$_3$-wd might not be appropriate to use as CO gas sensor.

3.2 The response of LaCoO$_3$-cp to CO sensing
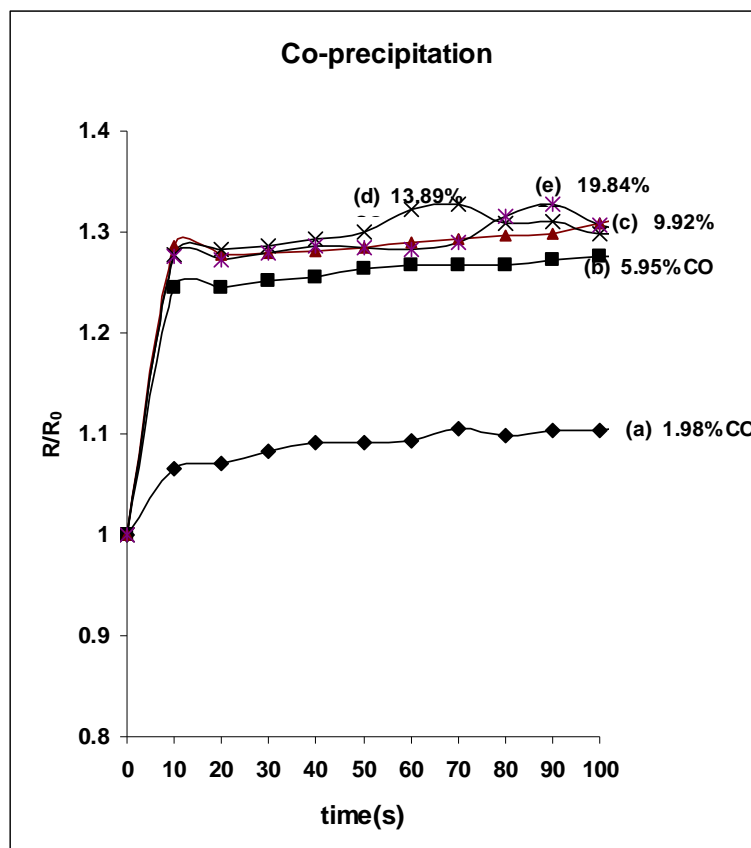
Figure 46 LaCoO$_3$-cp sensor response with time on exposing to CO concentrations
of 1.98-19.84% v/v.

To further study the CO sensing capability of LaCoO$_3$-cp, the experiments
were performed at various %CO concentration. Figure 46 represented the sensitivity
with time on exposing to CO concentration of 1.98-19.84%. The sensitivity increased
with the increase of CO concentrations. At 1.98% CO, the sensitivity was low. For
5.95-19.84% CO, the sensitivity was slightly increased. The interaction of CO on
active site (Co^{3+}) was less on surface LaCoO$_3$-cp compare to that of LaCoO$_3$-ss(1:1)
due to the Co$_3$O$_4$ impurity on the LaCoO$_3$-cp surface, leading to the slight increase in
R/R$_0$ sensing.

3.3 The CO quantitative range of $LaCoO_3$-cp sensor

For the studies of $LaCoO_3$-cp performance on CO sensing, Table 15 showed the sensitivity on exposing to 0.39-99.2%CO v/v. The sensitivity of $LaCoO_3$-cp was slightly fluctuation between 1.13-1.29 when CO concentrations of 0.39-38.63% were injected and the sensitivity was continued to increase as the CO concentration was increased to 99.20%.

Table 15 The sensitivity (R/R_0) of $LaCoO_3$-cp at 0.39-99.2% v/vCO.

CO (ml)	CO (%)	R/R_0
0.2	0.39	1.13
0.4	0.79	1.20
0.6	1.19	1.22
0.8	1.58	1.22
1	1.98	1.21
2	3.96	1.25
5	9.92	1.25
10	19.84	1.29
15	29.76	1.21
20	38.63	1.21
25	49.60	1.35
30	59.52	1.37
35	69.44	1.47
40	79.36	1.52
45	89.28	1.51
50	99.20	1.78

From Table 15, the relation between sensitivity and CO concentration could be presented in Figure 47. Figure 47 showed that the sensitivity (R/R_0) trended to increase up to 99.20% CO exposing. The fluctuated of R/R_0 might due to the incomplete reaction of $LaCoO_3$ with CO at some CO injection. Also, the incomplete desorption of CO_2 product from the surface could also be the reason of fluctuation.
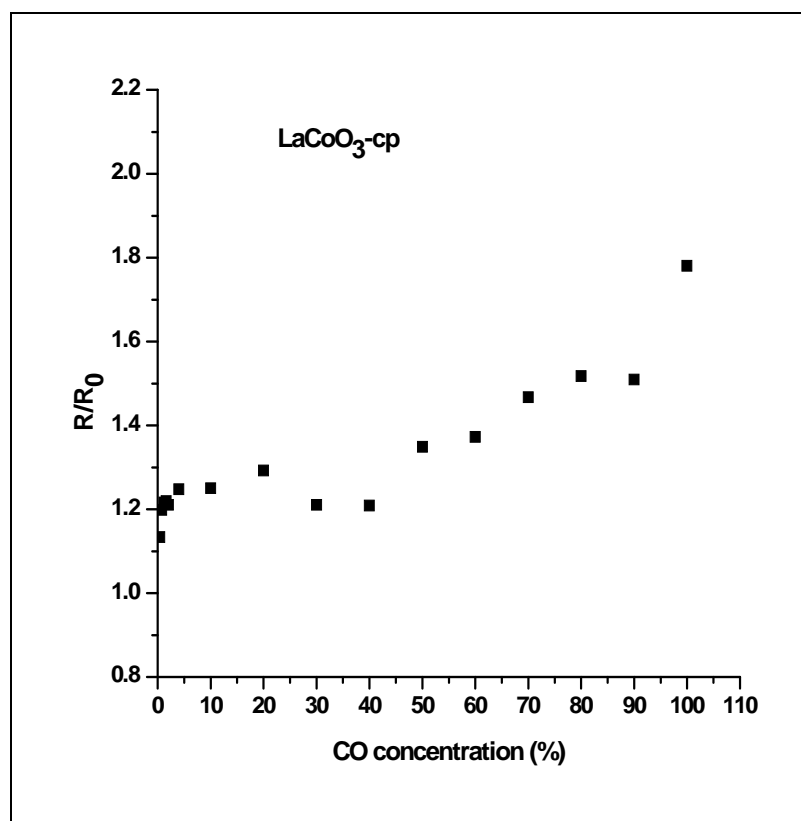
Figure 47 The sensitivity of $LaCoO_3$-cp on exposing to CO concentrations of 0.39-99.2% v/v at 20s.

Table 16 showed the sensitivity (R/R_0) of $LaCoO_3$-cp on exposing to low CO concentration of 0.004 to 0.039% v/v. $LaCoO_3$-cp had the detection limit of approximate 0.006% (60 ppm). The sensitivity was slowly increased from 0.996-1.046 as increasing CO concentration from 0.004% to 0.039%; but the relation

between the sensitivity and CO concentration was linear up to approximate 0.02% as shown in Figure 48.

With the high resistance (low conductivity) of $LaCoO_3$-wd, it could not be an appropriate material for CO sensor.

Table 16 The sensitivity (R/R_0) of $LaCoO_3$-cp at 0.004-0.039% v/v CO.

CO (ml)	CO (%)	R/R_0 (20s)	
(diluted 0.99% CO)		$LaCoO_3$-cp	$LaCoO_3$-wd
0.2	0.004	0.996	N/A[*]
0.3	0.006	1.013	N/A
0.4	0.008	1.015	N/A
0.6	0.012	1.038	N/A
0.8	0.016	1.028	N/A
1	0.019	1.033	N/A
2	0.039	1.046	N/A

[*]N/A – could not be measured
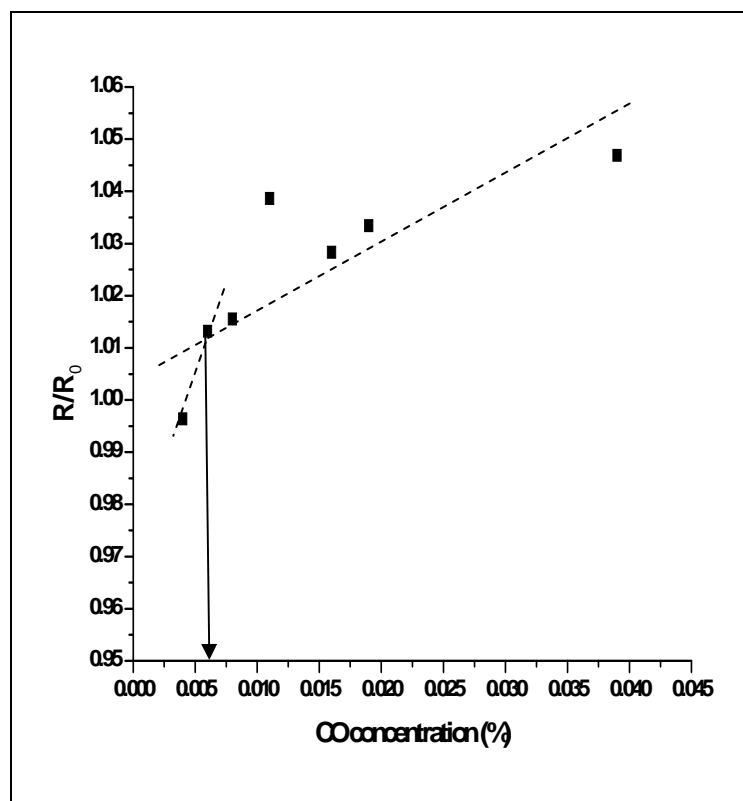
Figure 48 The sensitivity of LaCoO$_3$-cp on exposing to CO concentrations 0.004-
0.039% v/v at 20s.

From the experimental as results, both LaCoO$_3$-ss (1:1) and LaCoO$_3$-cp
had the detection limit of approximate 0.006% (60 ppm). Compared to commercial
ones, one from Futurlec ($ 8.90) (www.futurlec.com) could detect CO concentration
range of 10-1000 ppm, another from DEPOT-MQ7 ($ 7.95) (www.hwsensor.com)
could be used in the CO concentration range of 20-2000 ppm, and the other from
BRK-CO5120BN ($56.00) (www.brkeletronics.com) could be used in the range of
30-400 ppm. The prepared CO sensor from LaCoO$_3$-ss (1:1) and LaCoO$_3$-cp could go
to the lowest CO concentration of 60 ppm, which the value was higher than the
detection limit of other commercial ones. However, the 60 ppm detection limit of the
prepared sensor was still lower than 100 ppm (Ihokura., 1994), which was the toxic
CO concentration level for health and safety at 90 minutes exposure and the cost of
the fabricated one was less approximately $7.50.

CONCLUSION

LaCoO$_3$-ss (1:1, 1:5 (high Co) and 5:1(high La)) perovskites were prepared by the solid state reaction and calcined for 2 h at temperature of 700-900°C using lanthanum oxide (La$_2$O$_3$) and cobalt oxide (Co$_3$O$_4$) as starting materials. The XRD patterns of all LaCoO$_3$-ss corresponded to the perovskites with the rhombohedral geometry and with the impurity of Co$_3$O$_4$ for LaCoO$_3$-ss (high Co) and La$_2$O$_3$ for LaCoO$_3$-ss (high La). From other methods of co-precipitation and modified wet powder dispersion, the XRD patterns of LaCoO$_3$-wd and LaCoO$_3$-cp corresponded to the perovskite with the rhombohedral geometry with the impurity of La(OH)$_3$ for LaCoO$_3$-wd and Co$_3$O$_4$ for LaCoO$_3$-cp. The crystallite sizes of LaCoO$_3$-ss (1:1), LaCoO$_3$-ss (high Co), and LaCoO$_3$-ss (high La) at the calcination temperature of 850°C were calculated by Scherrer's equation giving the crystallite size of 122, 42, and 73 nm from solid state reaction method and of about 28 nm from both co-precipitation and modified wet powder dispersion methods. Both LaCoO$_3$-cp and LaCoO$_3$-wd methods gave the same order of crystallite size but having different morphology. For XANES spectra of the LaCoO$_3$-ss (1:1 and high La) having the edge position of approximate 7723 eV, the average Co oxidation state could be +3. The average oxidation state of LaCoO$_3$-ss (high Co) was in the range of 2 to 8/3. The peak edge energy for LaCoO$_3$-cp and LaCoO$_3$-wd were 7720.8 and 7722.0 eV, giving an average Co oxidation state closed to 2 and between 2 and 3, respectively. From BET surface area analysis, the surface area was 3.9, 5.2, 11.75, and 11.69 m^{2}g^{-1} for LaCoO$_3$-ss (high Co), LaCoO$_3$-ss (high La), modified wet powder dispersion, and co-precipitation methods, respectively. For LaCoO$_3$-ss (1:1), it gave rather low specific surface area of 1.6 m^{2}g^{-1}.

To study the CO sensing response, the resistance of LaCoO$_3$-ss (1:1, high Co, and high La), LaCoO$_3$-cp, and LaCoO$_3$-wd perovskites were measured. At the applied voltages of 7.5 volts, corresponded to temperature of 133°C measured at the LaCoO$_3$-ss (1:1) surface calcined at 850°C, the resistance was decreased to approximate 1000 Ω. At the same condition, the resistance of LaCoO$_3$-cp was

approximately 6000 Ω which closed to that of $LaCoO_3$-ss (high Co), whereas the resistance of $LaCoO_3$-ss (high La) and $LaCoO_3$-wd was about 2 MΩ. Due to the high resistance (low conductivity) of $LaCoO_3$-ss (high La) and $LaCoO_3$-wd, both perovskites were discontinued for the further studies.

From the sensitivity (R/R_0) of $LaCoO_3$-ss (1:1 and high Co) on exposing to the CO concentration of 1.98-19.84% v/v, the results found that the sensitivity (R/R_0) of $LaCoO_3$-ss (1:1) sensor was increased with increasing CO concentration and the sensitivity (R/R_0) of $LaCoO_3$-ss (high Co) was fluctuated with time after 20s. From the sensitivity (R/R_0) of $LaCoO_3$-ss (1:1) in the overall range of 0.39-99.2%v/v CO concentration, the sensitivity showed as high as 1.99. To study the detection limit of $LaCoO_3$-ss (1:1), the experiments were performed using the low CO concentration of 0.004-0.039%v/v and the result showed the sensitivity (R/R_0) of 0.9770-1.027 giving the detection limit of 0.006% (60ppm). From the sensitivity of $LaCoO_3$-cp on exposing to the CO concentration of 1.98-19.84%v/v, the result showed the increase of sensitivity with the increase of CO concentration. At 1.98%v/v CO, the sensitivity was low. For 5.95-19.84%v/v CO, the sensitivity was slightly increased. The sensitivity (R/R_0) of $LaCoO_3$-cp at 0.39-99.2%v/v CO concentration trended to increase up to 99.2%v/v. The fluctuated of R/R_0 might be due to the incomplete reaction of $LaCoO_3$ with CO at some CO injection. The sensitivity (R/R_0) of $LaCoO_3$-cp on exposing to low CO concentration of 0.004-0.039%v/v was slowly increased from 0.9960 to 1.046 giving the detection limit of 0.006% (60ppm). After CO sensor testing, the $LaCoO_3$-ss (1:1) gave better results than others followed by $LaCoO_3$-ss (high Co) and $LaCoO_3$-cp perovskites.

From the experiments, both $LaCoO_3$-ss (1:1) and $LaCoO_3$-cp exhibited the detection limit of approximate 0.006% (60 ppm). Compared to the commercial ones, the cost could be in ranged of $7.95-$56.00 with the detection limit of 10-30 ppm. The 60 ppm detection limit of the prepared CO sensor was higher than that of the commercial ones. However the value of 60 ppm was lower than 100 ppm, which was

the toxic CO concentration level for health and safety at 90 minutes exposure and the cost of the fabricated was less (approximately $7.50).

LITERATURE CITED

Ajami, S., Y. Mortazavi and S. Mohajerzadeh. 2006. Highly selective sensor to CH_4 in presence of CO and ethanol using $LaCoO_3$ perovskite filter with Pt/SnO_2. **Sens. Actuator. B.** 117: 420-425.

Alifanti, M., F. Mihaela and I. Vasile. 2007. Ceria-based oxides as supports for $LaCoO_3$ perovskite; catalysts for total oxidation of VOC. **Appl. Catal. B.** 70: 400-405.

Barbero, B.P., J.A. Ganboa and L.E. Cadús. 2006. Synthesis and characterization of $La_{1-x}Co_xFeO_3$ perovskite-type oxide catalysts for total oxidation of volatile organic compounds. **Appl. Catal. B**. 65: 21-30.

Borovskikh, L., G. Mazo and E. Kemnitz. 2003. Reactivity of oxygen of complex cobaltates $La_{1-x}Sr_xCoO_{3-\delta}$ and $LaSrCoO_4$. **Solid State Sciences.** 5: 409-417.

Brosha, E., R. Mukundon, and M. Lagothetis. 2000. CO/HC sensor based on thin film of $LaCoO_3$ and $La_{0.8}Sr_{0.2}LoO_{3-\delta}$ metal oxide. **Sens. Aatuator.** 69: 171-182.

Chen, C.H., H. Kruidhof, H.J.M. Bouwmeester and A.J. Burggraaf. 1997. Ionic conductivity of perovskite $LaCoO_3$ measured by oxygen permeation technique. **J. Appl. Electrochem.** 27: 71-75.

Chen, Y.C., T.H. Chang, G.J. Chen, Y.L. Chai and D.T. Ray. 2003. The sensing properties of hetero junction $SnO_2/La_{0.8}Sr_{0.2}Co_{0.5}Ni_{0.5}O_3$ thin-film CO sensor. **Sens. Actuators. B**. 96: 82-87.

Chu, X. 2003. High sensitivity chlorine gas sensors using $CdIn_2O_4$ thick film prepared by co-precipitation method. **Mat. Res. Bul.** 38: 1705-1711.

Cullity, B.D and S.R Stock. 2001. **Elements of X-ray Diffraction.** 3rd ed, Prentice Hall, New Jercy.

Elisabetta, D., E. Bartolomeo, and K. Vasant. 2000. Solid state ceramic gas sensors based on interfacing ionic conductors with semiconducting oxides**. J. Eur. Ceram. Soc.** 20: 2691 – 2699**.**

Ertl, G., H. Knozinger and J. Weitkamp. 1999. **Environmental catalysis.** Wiley – VCM, Mörlenbach.

Fergus, J. 2007. Perovskite for semiconductor-based gas sensors. **Sens. Actuators. B**. 123: 1169-1179.

Fernades, J.D.G., D.M.A. Melo, L.B. Zinner, C.M. Salustiano, Z.R. Silva, A.E. Martinelli, M. Cerqueira, C. A. Júnior, E. Longo and M.I.B. Bernardi. 2002. Low-temperature synthesis of single-phase crystalline $LaNiO_3$ perovskite via Pechini method. **Mater. Lett.** 53: 122-125.

Frackowiak, E. 2001. Carbon materials for electrochemical storage of energy in capacitors. **Carbon**. 39: 937-950.

Haas, O., R.P. Struis and J.M. McBreen. 2004. Synchotron X-ray absorption of $LaCoO_3$ perovskite. **J. Solid State Chemistry.** 177: 1000-1010.

Hackenberger, M., K. Stephan, D. Kiebling, W. Schmitzand and G. Wendt. 1997. Influence of the preparation conditions on the properties of perovskite-type oxide catalysts. **Solid state Ionics.** 101-103: 1195-1200.

Hooker, A. 2002. Nanotechnology advantage applied to gas sensor development.

Huang, L., M. Bassir and S. Kaliaguine. 2007. Characters of perovskite-type $LaCoO_3$ prepared by reactive grinding. **Mat. Chem. Phys.** 101: 259–263**.**

Ito, T., Q. Zhang and F. Saito. 2004. Synthesis of Perovskite-type lanthanum cobalt oxide nanoparticles by means of mechanochemical treatment. **Powder Technology.** 143-144: 170-173.

Ihokura, K. and J. Watson. 1994. **The stannic oxide gas sensor.** CRC Press, Inc. USA.

Ivanova, S., E. Zhecheva and R. Stoyanova. 2007. Microstructure of $LaCoO_3$ prepared by freeze-drying of metal-citrate precursors revealed by EPR. **J. Phys. Chem. Solids.** 68: 168-174.

Jadhav, A.D., A.B. Gaikwad, V. Samuel and V. Ravi. 2007. A low temperature route to prepare $LaFeO_3$ and $LaCoO_3$. **Materials Letters.** 61: 2030-2032.

Jinjun, S., Y. Ruoxue, Z. Younhfa and Z. Xinrong. 2003. Determination of NH_3 gas by combination of nanosized $LaCoO_3$ converter with chemiluminescence detector. **Talanta** 6: 157-164.

Kaliaguine, S., A. Van Neste and R. Muzychuka. 2001. Perovskite-type oxides synthesized by reactive grinding Part I. Preparation and characterization. **Appl. Catal. A.** 209: 345–358.

Kangvansura, P. 2007. **Effects of preparation: The pechini, Schiff base complex and coprecipitation, on structure and properties of $LaCoO_3$ perovskite oxidative catalyst.** M.S. Thesis. Kasetsart University.

Kao, C.F. and W.D. Yang. 1996. Preparation and electrical characterisation of strontium titanate ceramic from titanyl acylate precursor in strong alkaline solution. **Ceram. Int.** 22: 57-66.

Khalil, M.S. 2003. Synthesis, X-ray, infrared spectra and electrical conductivity of La/Ba-CoO$_3$ systems. **Mater. Sci. Eng.** A352: 64-70.

Kharton, V., E.N. Naumovich, A.V. Kovalevsky, A.P.Viskup, F.M. Figueiredo, I.A. Bashmakov and F.M.B. Marques. Mixed electronic and ionic conductivity of LaCo(M)O$_3$ (M= Ga,Cr, Fe or Ni) IV. Effect of preparation method on oxygen transport in LaCoO$_{3-\delta}$. **Solid State Ionics** 138: 135-148.

Kharton, V.V., F.M, Figueiredo, A.V, Kovalevsky and A.P, Viskup. 2001. Processing, microstructure and properties of LaCoO$_{3-\delta}$ ceramics. **J. Eur. Ceram. Soc.** 21: 2301-2309.

Kida, T., T. Kuroiwa, M. Yuasa, K. Shimanoe and N. Tamazoe. 2008. Study on the response and recovery properties of semiconductor gas sensors using a high-speed gas-switching system. **Sens. Actuators. B**. 134: 928-933.

Klung, H.P. and L.E. Alexander. 1954. **X-ray diffraction procedures: for polycrystalline and amorphous materials.** Jonh Wiley & Sons Inc., Canada.

Kocache, R. 1994. Gas sensors. **Sens. Review.** 14: 8-12.

Kong, L. and Y. Shen. 1996. Gas-sensing property and mechanism of Ca$_x$La$_{1-x}$FeO$_3$ ceramics. **Sens. Actuators. B**. 30: 217-221.

Krupicka, E., A. Reller and A. Weidenkaff. 2002. Morphology of nanoscaled LaMO$_3$-particles (M = Mn, Fe, Co, Ni) derived by citrate precursors in aqueous and alcoholic solvents. **Cryst. Eng.** 5: 195-202.

Li, N., B. Antoinette, D. Jean-Pierre and G.Francois. 2008. Catalytic combustion of toluene over a Sr and Fe substituted LaCoO$_3$ perovskite. **Solid State Ionics.** xx: xxx-xxx.

Ling, T-R., Z-B. Chen and M-D, Lee. 1996. Catalytic behavior and electrical conductivity of LaNiO$_3$ in ethanol oxidation. **Appl. Catal. A.** 136: 191-203.

_____, _____, and _____. 1995. Studies on catalytic and conductive properties of LaNiO$_3$ for oxidation of C$_2$H$_5$OH, CH$_3$OH, and CH$_4$. **Catal. Today.** 26: 79-86.

Ludmila, B., M. Galina and K. Erhard. 2003. Reactivity of oxygen of complex cobaltates La$_{1-x}$ Sr$_x$CoO$_{3-\delta}$ and LaSrCoO$_4$. **Solid State Sci.** 5: 409-417.

Makshina, E.V., S.V. Sirotin and B.V. Romanovsky. 2006. Characterization and catalytic properties of nanosized cobaltate particles prepared by in situ synthesis inside mesoporous molecular sieves. **Appl. Catal. A.** 312: 56-66.

Mawdsley, J. and T.R. Krause. 2008. Rare earth-first-row transition metal perovskites as catalysts for the autothermal reforming of hydrocarbon fuels to generate hydrogen. **Appl. Catal. A.** 334: 311-320.

Mei, Y., Z. Yu. and L. Zi-Kui. Defect analysis and thermodynamic modeling of LaCoO$_3$. **Solid State Ionics**. inpress.

Michel, C.R., E. Delgado, G. Santillan, A.H. Martinez and A. Chavez-Chavez. 2007. An alternative gas sensor material: Synthesis and electrical characterization of SmCoO$_3$. **Mat. Res. Bulle.** 42: 84-93.

Niemantsverdriet, J.W. 1995. **Spectroscopy in catalysis**. VCH., Weinheim

Natile, M., E. Ugel, C. Maccato and A. Glisenti. 2007. LaCoO$_3$: Effect of synthesis condition on properties and reactivity. **Appl. Catal. B.** 72: 351-362.

Orlovskaya, N., K. Kleveland, T. Grande and M-A. Einarsrud. 2000. Mechanical properties of LaCoO$_3$ based ceramics. **J. Eur. Ceram. Soc.** 20: 51-56.

Peña, M.A. and J.L.G. Fierro. 2001. Chemical structures and performance of perovskite oxides. **Chem. Rev.** 101:1981-2017.

Popa, M., L.V. Hong and M. Kakihana. 2003. Nanopowder of $LaMeO_3$ perovskites obtained by solution-based ceramic processing technique. **Physica. B.** 327: 233-236.

Pokhrel, S., L. Huo and H. Zhao. 2007. Thick film of $LaCr_{1-x}Ti_xO_3$ ($x \leq 0.4$) perovskite prepared by combustion technique for alcohol sensing application. **Sens. Actuators. B**. 122: 321-327.

Prangsri-aroon, S. 2008. **The partial oxidation of methane to syn gas by LaCoO₃ oxidative catalyst.** M.S. Thesis. Kasetsart University.

Read Mark, S.D., M.S. Islam, G.W. Watson, F. King and F.E. Hancock. 2000. Defect chemistry and surface properties of $LaCoO_3$. **J. Mater. Chem.** 10: 2298-2305

Rougier, A., S. Soiron, I. Haihal, L. Aymard, B. Taouk and J.M.Tarascon. 2002. Influence of grinding on the catalytic properties of oxides. Powder Technol. 128: 139-147.

Royer, S., D. Duprez. and S. Kaliaguine. 2005. Role of bulk and grain boundary oxygen mobility in catalytic oxidation activity of $LaCo_{1-x}Fe_xO_3$. **Catal. Today.** 112: 364-375.

_____, _____, and _____. 2006. Oxygen mobility in $LaCoO_3$ perovskites. **Catal. Today.** 112: 99-102.

_____, F. Berube and S. Kaliaguine. 2005. Effect of the synthesis conditions on the redox and catalytic properties in oxidation reaction of $LaCo_{1-x}Fe_xO_3$. **Appl. Catal. A.** 282: 273-284.

Salker, A.V., N. Choi and L. Duk-Dong. 2005. Thick films of In, Bi and Pd metal oxides impregnated in $LaCoO_3$ perovskite as carbon monoxide sensor. **Sens. Aatuator. B** 106: 461–467.

Satterfield, C.N. 1980. **Heterogeneous catalysis in practice.** McGraw-Hill book company, New York.

Shan, W., M. Fleys, F. Lapicque, D. Swierczynski, A. Kiennemann, Y. Simon and P.M. Marquaine. 2006. Syngas production from partial oxidation of methane over $Ce_{1-x}Ni_xO_y$ catalysts prepared by complexation-combustion method. **Appl. Catal. A.** 311:24-33.

Shinichi, S., M. Shinichi and Y. Hiroshi. **Process for preparing raw material powder of easily sinterable perovskite by wet powder dispersion process Japanese patent.** JP, 61-163118, A, 23 July 1986.

Shu, J., and S. Kaliaguine. 1998. Well-dispersed perovskite-type oxidation catalysts. **Appl. Catal. B.** 16: L303-L308.

Simonot, L., F. Garin and G. Maire. 1997. A comparative study of $LaCoO_3$, Co_3O_4 and $LaCoO_3$-Co_3O_4 I. Preparation, charactrisation and catalytic properties for the oxidation of CO. **Appl. Caltal. B.** 11: 167-179.

Smart, L and E. Moore. 1995. **Solid state chemistry an introduction.** Chatman & Hall, London.

Sonya, I., Z. Ekaterina and S. Radostina. 2007. Microstructure of $LaCoO_3$ prepared by freeze-drying of metal–citrate precursors revealed by EPR. **J. Phys. Chem. Solids.** 68: 168–174.

Sorita, R. and T. Kawano. 1997. A highly selective CO sensor using $LaMnO_3$ electrode-attached zirconia galvanic cell. **Sens. Actuators. B**. 40: 29-32.

Spinicci, R., A. Tofanari, M. Faticanti, I. Pettiti, and P. Porta. 2001. Hexane total oxidation on $LaMO_3$ (M = Mn, Co, Fe) perovskite-type oxides. **J. Mole. Catal. A.** 176: 247-252.

Srichaisiriwech, W. 2002. **Studies of perovskite-type oxides catalysts for oxidation of organic chemical wastes**. M.S. Thesis, Kasetsart University.

Suman, P., H. Lihua, Z. Hui and G. Shan. 2007. Thick film of $LaCr_{1-x}Ti_xO_3$ ($x \leq 0.4$). perovskites reparedby combustion technique for alcohol sensing application. **Sens. Aatuator. B.** 122: 321-327.

Szabo, V., M. Bassir, J.E. Gallot, A. Van Neste and S. Kaliaguine. 2003. Perovskite-type oxides synthesized by reactive grinding Part III. Kinetics of *n*-hexane oxidation over $LaCo_{(1-x)}Fe_xO_3$. **Appl. Catal. B.** 42: 265-277.

Taguchi, H., S. Yamada, M. Nagao, Y. Ichikawa and K. Tabata. 2002. Surface characterization of $LaCoO_3$ synthesized using citric acid. **Mater. Res. Bulle.** 37: 69-76.

Takeshi, Y., U. Yoshiharu and N. Yusuke. 2000. Synthesis of (La,Sr)MeO (Me_5Cr, Mn, Fe, Co) solid solutions from aqueous solutions. **Solid State Ionics.** 35: 359–364.

Tejuca, L.G. 1988. Properties of perovskite type oxides. II. Studies in catalysis. **J. Less. Common Met.** 146: 261.

Teng, F., S. Liang, B. Gaugeu, R. Zong, W. Yao and Y. Zhu. 2007. Carbon nanotube-templated of $LaCoO_3$ and its excellent catalytic properties for CO oxidation. **Catal. Comm.** 8: 1748-1754.

Tien-Thao, N., H. Alamdari, M.H. Zahedi-Niaki and S. Kaliaguine. 2006. $LaCo_{1-x}Cu_xO_{3-\delta}$ perovskite catalysts for higher alcohol synthesis. **Appl. Catal. A.** 311: 204-212.

_____, _____, _____, and _____. 2008. Characterization and reactivity of nanoscale $La(Co,Cu)O_3$ perovskite catalyst precursors for CO hydrogenation. **J. Solid State Chem.** 181: 2006-2019.

Toan, N.N., S. Saukko and V. Lantto. 2003. Gas sensing with semiconducting perovskite oxide $LaFeO_3$. **Phys. B.** 327: 279-282.

Varma, H., K.G. Warrier and A.D. Damodaran. 1990. Metal nitrate-urea decomposition route for Y-Ba-Cu-O powder. **J. Am. Ceram. Soc.** 73: 3103.

Viravathana, P. and S. Prangsri-aroon. 2009. **Preparation of rod perovskites.** Thailand Patent 0901000358.

Voorhoeve, R.J.H. 1977. **Advanced materials in catalysis**. Academic Press. New York.

Wang, Y., J. Zhu, L. Zhang, X. Yang, L. Lu and X. Wang. 2006. Preparation and characterization of perovskite $LaFeO_3$ nanocrystals. **Mater. Lett.** 60: 1767-1770.

Wells, A.F. 1995. **Structural inorganic chemistry**. 5th ed. Oxford Science Publication, Singapore.

William, F. 1990. **Principle of materials science and engineering.** 2nd ed.
    Mcgraw-hill Publ. Co. Inc., Singapore.

Yamazoe, N. 2005. Toward innovations of gas sensor technology. **Sens. Actuators.
    B**. 108: 2-14.

Yang, M., Y. Zhong and Z-K. Liu. 2007. Defect analysis and thermodynamic
    modeling of LaCoO$_{3-\delta}$. **Solid State Ionics.** xx: xxx-xxx.

Yang, W.D., Y.H. Chang and S.H. Huang. 2004. Influence of molar ratio citric acid
    to metal ions on preparation of La$_{0.67}$Sr$_{0.33}$MnO$_3$ materials via polymerizable
    complex process. **J. Eur. Ceram. Soc.** *Article in Press*.

Yang, X., L. Luo and H. Zhong. 2005. Preparation of LaSrCoO$_4$ mixed oxides and
    their catalytic properties in the oxidation of CO and C$_3$H$_8$. **Catal. Comm.** 6:
    13-17.

Yao, T., Y. Uchimoto, T. Sugiyama and Y. Nagai. 2000. Synthesis of (La,Sr)MeO$_3$
    (Me = Cr, Mn, Fe, Co) solid solutions from aqueous solutions from aqueous
    solutions. **Solid State Ionics.** 35: 359-364.

Yi Can, Z., H. Narita, J. Mizusaki and H. Tagawa. 1995. Detection of carbon
    monoxide by using zirconia oxygen sensor. **Solid State Ionics.** 7: 344-348.

Yongfa, Z., T. Ruiqin and C. Lili. 2001. The reaction and poisoning mechanism of
    SO$_2$ and perovskite LaCoO$_3$ film model catalysts. **Appl. Catal. A.** 209: 71-
    77**.**

Zhao, S., J.K.O. Sin, B. Xu, M. Zhao, Z. Peng and H. Cai. 2000. A high performance
    ethanol sensor based on field-effect transistor using a LaFeO$_3$ nano-crystalline
    thin-film as a gas electrode. **Sens. Actuators. B.** 64: 83-87.

Zhang, H.M., Y. Teraoka and N. Yamazoe. 1987. Preparation of perovskite-type oxides with large surface area by citrate process. **Chem. Lett.** 665.

Zhang, Q. and F. Saito., 2000. Mechanochemical synthesis of $LaMnO_3$ from La_2O_3 and Mn_2O_3 powders. **J. Alloys Comp.** 297: 99-103.

Zhang, R., A. Villanueva, H. Alamdari and S. Kaliaguine. 2006. Reduction of NO by CO over nanoscale $LaCo_{1-x}Cu_xO_3$ and $LaMn_{1-x}Cu_xO_3$ perovskites. **J. Mole. Catal. A**. 256: 22-34.

Zhang, Y., Y. Zhu, R. Tan, W, Yao and L. Cao. 2001. Influence of PEG additive and precursor concentration on the preparation of $LaCoO_3$ film with perovskites structure. **Thin Solid Films.** 388: 160-164.

Zhou, Z., Z-L. Tang and W. Wlodarski. 2001. Perovskite oxide of PTCR ceramics as chemical sensors. **Sens. Actuators. B**. 77: 22-26.

Zhou, Z-G., Z-L, Tang and Z-T, Zhang. 2003. Studies on grain-boundary chemistry of perovskite ceramics as CO gas sensors. **Sens. Actuators. B**. 93: 356-361.

APPENDICES

Appendix A

Apparent density measurement

Appendix Table A1 The results of apparent density of $LaCoO_3$-ss (1:1, 850°C).

Mass (g)	No. of experiments	Volume (cc)	Apparent density (g/cc)	SD
	1	0.1388	7.2107	
	2	0.1397	7.1656	
1.0010	3	0.1386	7.2214	0.0244
	4	0.1389	7.2064	
	5	0.1385	7.2280	
	Average	**0.1389**	**7.2068**	

Appendix Table A2 The results of apparent density of $LaCoO_3$-ss (high Co, 850°C).

Mass (g)	No. of experiments	Volume (cc)	Apparent density (g/cc)	SD
	1	0.1441	6.9552	
	2	0.1427	7.0269	
1.0025	3	0.1437	6.9749	0.0268
	4	0.1437	6.9759	
	5	0.1434	6.9911	
	Average	**0.1435**	**6.9848**	

Appendix Table A3 The results of apparent density of LaCoO$_3$-ss (high La, 850°C).

Mass (g)	No. of experiments	Volume (cc)	Apparent density (g/cc)	SD
	1	0.1715	5.8047	
	2	0.1727	5.7978	
1.0012	3	0.1734	5.7737	0.0198
	4	0.1719	5.8228	
	5	0.1720	5.8200	
	Average	**0.1725**	**5.8038**	

Appendix Table A4 The results of apparent density of LaCoO$_3$-cp.

Mass (g)	No. of experiments	Volume (cc)	Apparent density (g/cc)	SD
	1	0.0787	7.8697	
	2	0.0779	7.9434	
0.6191	3	0.0816	7.5858	0.2049
	4	0.0820	7.5530	
	5	0.0775	7.9905	
	Average	**0.0795**	**7.7885**	

Appendix Table A5 The results of apparent density of LaCoO$_3$-wd.

Mass (g)	No. of experiments	Volume (cc)	Apparent density (g/cc)	SD
	1	0.1626	6.6302	
	2	0.1637	6.5862	
1.0779	3	0.1639	6.5778	0.1793
	4	0.1701	6.3375	
	5	0.1732	6.6302	
	Average	**0.1667**	**6.4712**	

Appendix B

XRD reference

48-0123						Wavelength= 1.54184				
LaCoO3										
	2θ	Int	h	k	l	2θ	Int	h	k	l
Cobalt Lanthanum Oxide	23.245	20	0	1	2	97.294	10	3	2	4
	32.905	84	1	1	0	97.984	8	3	1	8
	33.324	100	1	0	4	99.123	8	1	1	12
	38.986	3	1	1	3	107.426	4	0	4	8
Rad.: CuKa1λ: 1.5406 Filter: Graph Mono d-sp: Diff.	40.690	28	2	0	2					
	41.374	12	0	0	6					
Cut off: 5.9 Int.: Diffract. I/Icor.:	47.538	61	0	2	4					
Ref: Closset, N et al., Powder Diffraction, 11, 31 (1996)	53.281	8	1	2	2					
	53.839	8	1	1	6					
	58.747	23	3	0	0					
	59.003	41	2	1	4					
Sys.: Rhombohedral S.G.: R3c (167)	59.814	19	0	1	8					
a: 5.4445(2) b: c: 13.0936(6) A: C: 2.4049	68.993	13	2	2	0					
	69.980	16	2	0	8					
α: β: γ: Z: 6 mp:	73.905	4	3	1	2					
	74.379	5	3	0	6					
Ref: Ibid.	75.333	3	1	0	10					
	78.813	11	1	3	4					
	79.509	15	1	2	8					
Dx: 7.287 Dm: 7.290 SS/FOM: F_{30} = 112(.0068, 39)	83.292	3	0	4	2					
	83.743	4	2	2	6					
Color: Black	84.680	3	0	2	10					
Prepared by thermal decomposition of an aqueous solution of	88.078	4	4	0	4					
the metal nitrates and EDTA followed by calcination at	89.900	3	0	0	12					
925 C for 10 hours in air and sintering at 1175-1225 C for 10	92.457	3	2	3	2					
hours in air. Rhombohedral cell: a=5.3787α=60.81. LaB6	93.884	3	2	1	10					
used as an internal stand. PSC: hR10. To replace 9-358 and	97.066	9	4	1	0					
25-1060. Mwt: 245.84, Volume[CD]: 336.13.										

Appendix Figure B1 XRD reference data of lanthanum cobalt oxide (48-0123).

05-0602						Wavelength= 1.54184				
La2O3										
	2θ	Int	h	k	l	2θ	Int	h	k	l
Lanthanum Oxide	26.132	34	1	0	0	137.096	2	2	2	4
	29.155	31	0	0	2	146.537	1	3	1	4
	29.986	100	1	0	1	148.649	2	2	1	6
	39.561	58	1	0	2					
Rad.: CuKa1λ: 1.5405 Filter: Ni Beta d-sp:	46.124	63	1	1	0					
	52.179	52	1	0	3					
Cut off: Int.: Diffract. I/Icor.:	53.764	4	2	0	0					
Ref: Swanson, Fuyat, Natl. Bur. Stand. (U.S.), Circ. 539, III,	55.489	24	1	1	2					
33 (1954)	56.004	17	2	0	1					
	60.425	3	0	0	4					
	62.316	5	2	0	2					
Sys.: Hexagonal S.G.: P3m1 (164)	66.932	2	1	0	4					
a: 3.9373 b: c: 6.1299 A: C: 1.5569	72.163	7	2	0	3					
	73.464	2	2	1	0					
α: β: γ: Z: 1 mp:	75.375	12	2	1	1					
	79.234	6	1	1	4					
Ref: Ibid.	80.929	4	2	1	2					
	83.850	4	1	0	5					
	85.139	2	2	0	4					
Dx: 6.574 Dm: SS/FOM: F_{30} = 47(.0160, 40)	85.408	4	3	0	0					
	90.015	7	2	1	3					
Color: Colorless	92.659	4	3	0	2					
Pattern taken at 26 C. Sample from Fairmount Chemical	97.933	<1	0	0	6					
Company. Sample was annealed at 1200 C for one hour and	101.545	3	2	0	5					
mounted in petrolatum to prevent reabsorption of C O2 + H2	103.156	3	2	2	0					
O. Spectroscopic analysis: <0.01% Ca, Mg, Si; <0.001%	103.942	1	1	0	6					
Al, Cu, Fe, Pb. Merck Index, 8th Ed., p. 608. Opaque mineral	109.177	<1	3	1	0					
optical data on specimen from Nanseke, Uganda:	110.687	3	2	2	2					
R3R%=14.2, Disp.=Std., VHN100=782-813, Ref.: IMA	111.168	5	3	1	1					
Commission on Ore Microscopy QDF. Pattern reviewed by	115.192	2	3	0	4					
Holzer, J., McCarthy, G., North Dakota State Univ., Fargo,	116.416	2	1	1	6					
ND, USA, ICDD Grant-in-Aid (1990. Validated by calculated	120.422	5	2	1	5					
pattern except for the following: 2.278 23 102; 1.968 28 110;	123.151	1	2	0	6					
1.753 23 103. Calculated pattern indicates that the following	127.843	4	3	1	3					
reflections might be observable: 6.130 <1 001; 2.043 <1 003;	130.764	2	1	0	7					
1.8744 <1 111; 1.4177 <1 113; 1.2260 <1 005: La2 O3 type.	131.871	1	4	0	1					
PSC: hP5. Mwt: 325.81. Volume[CD]: 82.30.										

Appendix Figure B2 XRD reference data of lanthanum oxide (05-0602).

42-1467   Wavelength= 1.54184

Co3O4

Cobalt Oxide

2_θ	Int	h	k	l
19.016	19	1	1	1
31.298	34	2	2	0
36.883	100	3	1	1
38.574	9	2	2	2
44.848	19	4	0	0
55.705	8	4	2	2
59.411	29	5	1	1
65.297	34	4	4	0
68.693	2	5	3	1
74.189	2	6	2	0
77.414	7	5	3	3
78.481	4	6	2	2
82.709	2	4	4	4
85.848	1	7	1	1
91.071	3	6	4	2
94.199	9	7	3	1
99.443	3	8	0	0
108.035	2	6	6	0
111.365	6	7	5	1
112.477	2	6	6	2
117.074	2	8	4	0

Rad.: CuKa1λ: 1.540598 Filter: Graph Mono d-sp: Diff.

Cut off: 15.0 Int.: Diffract. I/Icor.: 3.1

Ref: Martin, K., McCarthy, G., North Dakota State University, Fargo, North Dakota, USA, ICDD Grant-in-Aid, (1990)

Sys.: Cubic   S.G.: Fd3m (227)

a: 8.0837   b: c: A: C:

α: β: γ: Z: 8   mp:

Ref: Ibid.

Dx: 6.056   Dm: SS/FOM: F_{21} = 285(.0029 , 25)

Color: Black
Peak height intensity. Sample obtained from Fischer Scientific. Average relative standard deviation in intensity of the ten strongest reflections for three specimen mounts=4.0%. Validated by calculated pattern. Al2 Mg O4 type. Silicon used as an internal stand. Single-crystal data used. PSC: cF56. To replace 9-418. Mwt: 240.80. Volume[CD]: 528.24.

Appendix Figure B3 XRD reference data of cobalt oxide (42-1467).

83-2081   Wavelength= 1.54184

Al2O3

Aluminum Oxide

2_θ	Int	h	k	l
25.860	753	0	1	2
35.605	999*	1	0	4
38.149	503	1	1	0
42.306	2	0	0	6
43.839	936	1	1	3
46.665	17	2	0	2
53.169	473	0	2	4
58.267	935	1	1	6
60.371	23	2	1	1
61.792	35	1	2	2
62.238	60	0	1	8
67.303	351	2	1	4
68.948	514	3	0	0
71.292	10	1	2	5
75.392	11	2	0	8
78.150	151	1	0	10
78.439	110	1	1	9
81.627	63	2	2	0
84.331	13	0	3	6
85.383	38	2	2	3
86.148	2	1	3	1
87.393	34	3	1	2
87.788	22	1	2	8

Corundum - synthetic

Rad.: CuKa1λ: 1.54060 Filter: d-sp: Calculated

Cut off: 17.7 Int.: Calculated I/Icor.: 1.01
Ref: Calculated from ICSD using POWD-12++, (1997)
Ref: Finger, L.W., Hazen, R.M., Year Book Carnegie Inst. Washington, 76, 525 (1977)

Sys.: Rhombohedral   S.G.: R3c (167)

a: 4.718(4)   b: c: 12.818(1) A: C: 2.7168

α: β: γ: Z: 6   mp:

Ref: Ibid.

Dx: 4.111   Dm: ICSD # : 200141

Peak height intensity. R-factor: 0.055. PSC: hR10. Mwt: 101.96. Volume[CD]: 247.10.

Appendix Figure B4 XRD reference data of aluminum oxide (42-1467).

74-1657	Quality: C
CAS Number:	
Molecular Weight: 240.80	
Volume[CD]: 524.58	
Dx: 6.098 Dm:	
S.G.: Fd3m (227)	
Cell Parameters:	
a 8.065 b c	
α β γ	
I/Icor: 4.68	
Rad: CuKa1	
Lambda: 1.54060	
Filter:	
d-sp: calculated	
ICSD #: 027498	

Co3 O4
Cobalt Oxide
Ref: Calculated from ICSD using POWD-12++, (1997)
Ref: Roth, W.L., J. Phys. Chem. Solids, 25, 1 (1964)

d(A)	Int-f	h	k	l	d(A)	Int-f	h	k	l	d(A)	Int-f	h	k	l
4.6563	171	1	1	1	1.6462	81	4	2	2	1.2299	67	5	3	3
2.8514	323	2	2	0	1.5521	306	5	1	1	1.2158	34	6	2	2
2.4316	999	3	1	1	1.4257	345	4	4	0	1.1640	19	4	4	4
2.3281	89	2	2	2	1.3632	12	5	3	1	1.1293	7	5	5	1
2.0162	200	4	0	0	1.3441	1	4	4	2					
1.8502	1	3	3	1	1.2751	24	6	2	0					

Appendix Figure B5 XRD reference data of cobalt oxide d-spacing values.

48-0123	Quality: *
CAS Number:	
Molecular Weight: 245.84	
Volume[CD]: 336.13	
Dx: 7.287 Dm: 7.290	
S.G.: R3c (167)	
Cell Parameters:	
a 5.444 b c 13.09	
α β γ	
SS/FOM: F30=112(.0068, 39)	
I/Icor:	
Rad: CuKa1	
Lambda: 1.5406	
Filter: Graph	
d-sp: diffractometer	

La Co O3
Cobalt Lanthanum Oxide
Ref: Closset, N et al., Powder Diffraction, 11, 31 (1996)

d(A)	Int-f	h	k	l	d(A)	Int-f	h	k	l	d(A)	Int-f	h	k	l
3.8266	20	0	1	2	1.5462	19	0	1	8	1.1090	4	4	0	4
2.7220	84	1	1	0	1.3612	13	2	2	0	1.0912	3	0	0	12
2.6887	100	1	0	4	1.3444	16	2	0	8	1.0676	3	2	3	2
2.3103	3	1	1	3	1.2824	4	3	1	2	1.0551	3	2	1	10
2.2174	28	2	0	2	1.2754	5	3	0	6	1.0288	9	4	1	0
2.1823	12	0	0	6	1.2616	3	1	0	10	1.0270	10	3	2	4
1.9127	61	0	2	4	1.2144	11	1	3	4	1.0216	8	3	1	8
1.7193	8	1	2	2	1.2055	15	1	2	8	1.0129	8	1	1	12
1.7028	8	1	1	6	1.1601	3	0	4	2	.95640	4	0	4	8
1.5717	23	3	0	0	1.1550	4	2	2	6					
1.5655	41	2	1	4	1.1446	3	0	2	10					

Appendix Figure B6 XRD reference data of lanthanum cobalt oxide d-spacing
values.

Appendix C

K-edge XANES spectra
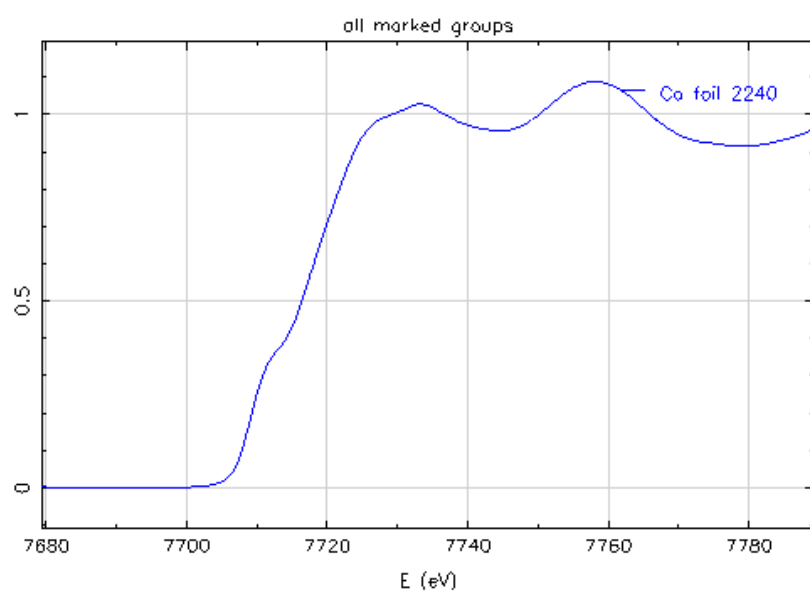
Appendix Figure C1 Co K-edge XANES spectra**.**
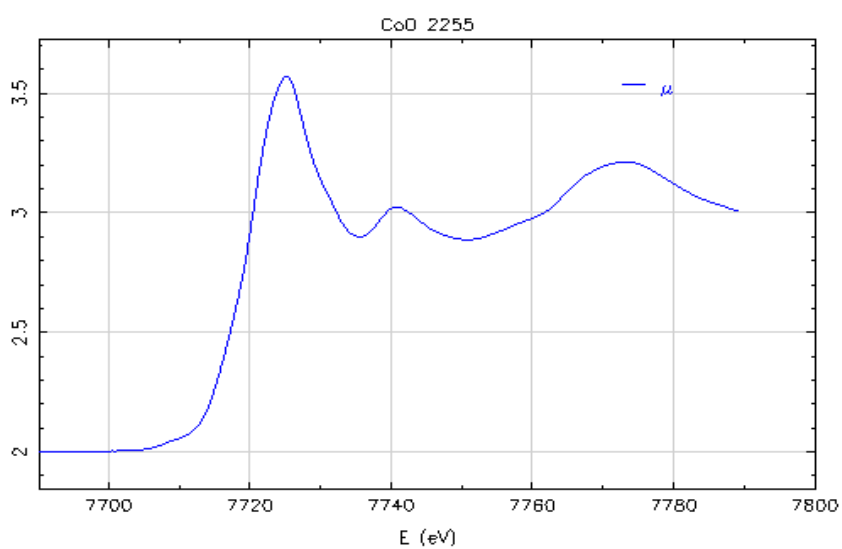
Appendix Figure C2 CoO K-edge XANES spectra.
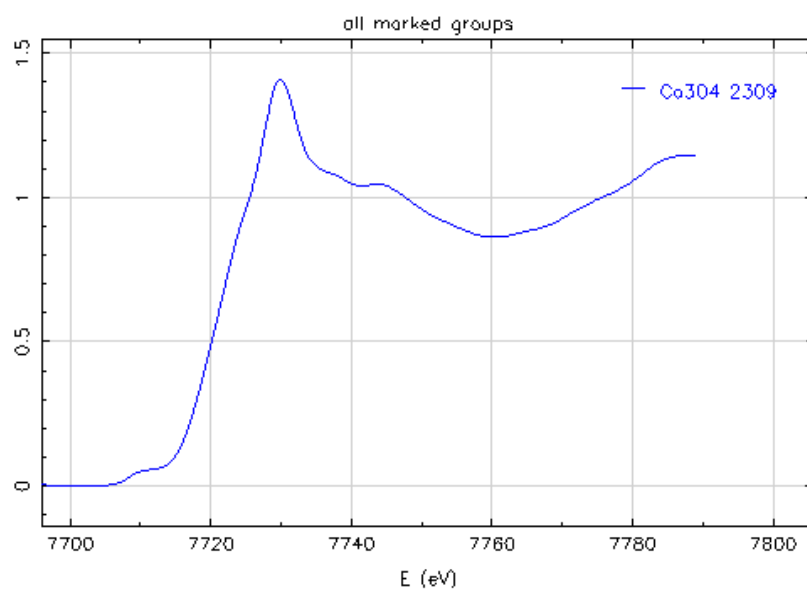
Appendix Figure C3 Co_3O_4 K-edge XANES spectra.

Appendix D

BET analysis

Quantachrome Corporation
Quantachrome Autosorb Automated Gas Sorption System Report
Autosorb for Windows®

Sample ID   LaCo 1:1 700 4 h
Description   TISTR
Comments
Sample Weight   0.0428 g
Adsorbate   NITROGEN   Outgas Temp   300.0 °C   Operator   Rungrueng
Cross-Sec Area   16.2 Å²/molecule   Outgas Time   3.0 hrs   Analysis Time 58.0 min
NonIdeality   6.580E-05   P/Po Toler   2   End of Run   01/03/1980
Molecular Wt   28.0134 g/mol   Equil Time   3   File Name   AS830511.RA
Station #   1   Bath Temp.   77.40

AREA-VOLUME-PORE SIZE SUMMARY

SURFACE AREA DATA

Multipoint BET... 1.413E+01 m²/g
Single Point BET.. 1.214E+01 m²/g
Langmuir Surface Area....................................... 3.307E+01 m²/g
t-Method External Surface Area.............................. 1.413E+01 m²/g
t-Method Micro Pore Surface Area............................ 0.000E+00 m²/g
DR Method Micro Pore Area................................... 1.236E+01 m²/g

PORE VOLUME DATA

t-Method Micro Pore Volume.................................. 0.000E+00 cc/g
DR Method Micro Pore Volume................................. 4.393E-03 cc/g
HK Method Cumulative Pore Volume............................ 3.232E-03 cc/g
SF Method Cumulative Pore Volume............................ 3.433E-03 cc/g

PORE SIZE DATA

DR Method Micro Pore Width   .... 1.586E+02 Å
DA Method Pore Diameter (Mode)............................. 1.920E+01 Å
HK Method Pore Width   (Mode)............................. 1.833E+01 Å
SF Method Pore Diameter (Mode)............................. 3.497E+01 Å

DATA REDUCTION PARAMETERS

Thermal Transpiration : ON
Effective Molecule Diameter (D) 3.5400 Å
Effective Cell Stem Inner Diameter (d) 4.0000 mm
Last Po Acquired 793.03 mm Hg
Additional Initialization Information Not Recorded.

BJH/DH Moving Average Size : 1

Interaction Constant (K) 2.9600 nm^3 x kJ/mol

Appendix Figure D1 BET analysis of LaCoO$_3$-ss (1:1, 700°C).

```
                          Quantachrome Corporation
          Quantachrome Autosorb Automated Gas Sorption System Report
                            Autosorb for Windows®

Sample ID        LaCo 1:1 800 4 h
Description      TISTR
Comments
Sample Weight    0.0428 g
Adsorbate        NITROGEN          Outgas Temp   300.0 °C   Operator        Rungrueng
Cross-Sec Area   16.2 Å²/molecule  Outgas Time   3.0 hrs    Analysis Time   56.3 min
NonIdeality      6.580E-05         P/Po Toler    2          End of Run      01/03/1980
Molecular Wt     28.0134 g/mol     Equil Time    3          File Name       AS830512.RA
Station #        1                 Bath Temp.    77.40


                      AREA-VOLUME-PORE SIZE SUMMARY

                            SURFACE AREA DATA

      Multipoint BET..............................................  4.024E+00  m²/g
      Single Point BET............................................  3.942E+00  m²/g
      Langmuir Surface Area.......................................  7.869E+00  m²/g
      t-Method External Surface Area..............................  4.024E+00  m²/g
      t-Method Micro Pore Surface Area............................  0.000E+00  m²/g
      DR Method Micro Pore Area...................................  3.942E+00  m²/g

                            PORE VOLUME DATA

      t-Method Micro Pore Volume..................................  0.000E+00  cc/g
      DR Method Micro Pore Volume.................................  1.401E-03  cc/g
      HK Method Cumulative Pore Volume............................  1.133E-03  cc/g
      SF Method Cumulative Pore Volume............................  1.190E-03  cc/g

                            PORE SIZE DATA

      DR  Method Micro Pore Width   ..............................  1.372E+02  Å
      DA  Method Pore Diameter (Mode).............................  1.920E+01  Å
      HK  Method Pore Width    (Mode).............................  1.808E+01  Å
      SF  Method Pore Diameter (Mode).............................  3.442E+01  Å

                        DATA REDUCTION PARAMETERS

                       Thermal Transpiration : ON
               Effective Molecule Diameter (D) 3.5400 Å
           Effective Cell Stem Inner Diameter (d) 4.0000 mm
                    Last Po Acquired 791.05 mm Hg
          Additional Initialization Information Not Recorded.

                     BJH/DH Moving Average Size : 1

            Interaction Constant (K) 2.9600 nm^3 x kJ/mol
```

Appendix Figure D2 BET analysis of $LaCoO_3$-ss (1:1, 800°C).

Quantachrome Corporation
Quantachrome Autosorb Automated Gas Sorption System Report
Autosorb for Windows®

Sample ID   LaCoO3 850
Description   TISTR
Comments
Sample Weight   0.1417 g
Adsorbate   NITROGEN   Outgas Temp   300.0 °C   Operator   Rungrueng
Cross-Sec Area   16.2 Å²/molecule   Outgas Time   3.0 hrs   Analysis Time   60.0 min
NonIdeality   6.580E-05   P/Po Toler   2   End of Run   01/05/1980 05
Molecular Wt   28.0134 g/mol   Equil Time   3   File Name   AS830524.RAW
Station #   1   Bath Temp.   77.40

AREA-VOLUME-PORE SIZE SUMMARY

SURFACE AREA DATA

Multipoint BET... 1.558E+00 m²/g
Single Point BET.. 1.809E+00 m²/g
Langmuir Surface Area..................................... 3.201E+00 m²/g
t-Method External Surface Area............................ 1.558E+00 m²/g
t-Method Micro Pore Surface Area.......................... 0.000E+00 m²/g
DR Method Micro Pore Area................................. 1.799E+00 m²/g

PORE VOLUME DATA

t-Method Micro Pore Volume................................ 0.000E+00 cc/g
DR Method Micro Pore Volume............................... 6.394E-04 cc/g
HK Method Cumulative Pore Volume.......................... 5.292E-04 cc/g
SF Method Cumulative Pore Volume.......................... 5.564E-04 cc/g

PORE SIZE DATA

DR Method Micro Pore Width   .... 1.244E+02 Å
DA Method Pore Diameter (Mode)......................... 1.840E+01 Å
HK Method Pore Width   (Mode)......................... 1.777E+01 Å
SF Method Pore Diameter (Mode)......................... 3.820E+01 Å

DATA REDUCTION PARAMETERS

Thermal Transpiration : ON
Effective Molecule Diameter (D) 3.5400 Å
Effective Cell Stem Inner Diameter (d) 4.0000 mm
Last Po Acquired 792.33 mm Hg
Additional Initialization Information Not Recorded.

BJH/DH Moving Average Size : 1

Interaction Constant (K) 2.9600 nm^3 x kJ/mol

Appendix Figure D3 BET analysis of LaCoO$_3$-ss (1:1, 850°C).

Quantachrome Corporation
Quantachrome Autosorb Automated Gas Sorption System Report
Autosorb for Windows®

```
Sample ID        LaCoO3 900
Description      TISTR
Comments
Sample Weight    0.1142 g
Adsorbate        NITROGEN          Outgas Temp   300.0 °C   Operator        Rungrueng
Cross-Sec Area   16.2 Å²/molecule  Outgas Time   3.0 hrs    Analysis Time   56.5 min
NonIdeality      6.580E-05         P/Po Toler    2          End of Run      05/13/2008 11
Molecular Wt     28.0134 g/mol     Equil Time    3          File Name       AS830527.RAW
Station #        1                 Bath Temp.    77.40
```

AREA-VOLUME-PORE SIZE SUMMARY

SURFACE AREA DATA

```
Multipoint BET............................................... 1.247E+00  m²/g
Single Point BET............................................. 1.138E+00  m²/g
Langmuir Surface Area........................................ 2.146E+00  m²/g
t-Method External Surface Area............................... 1.247E+00  m²/g
t-Method Micro Pore Surface Area............................. 0.000E+00  m²/g
DR Method Micro Pore Area.................................... 1.137E+00  m²/g
```

PORE VOLUME DATA

```
t-Method Micro Pore Volume................................... 0.000E+00  cc/g
DR Method Micro Pore Volume.................................. 4.041E-04  cc/g
HK Method Cumulative Pore Volume............................. 3.821E-04  cc/g
SF Method Cumulative Pore Volume............................. 4.176E-04  cc/g
```

PORE SIZE DATA

```
DR  Method Micro Pore Width    .............................. 6.173E+01  Å
DA  Method Pore Diameter (Mode)............................. 1.920E+01  Å
HK  Method Pore Width   (Mode)............................. 1.933E+01  Å
SF  Method Pore Diameter (Mode)............................. 3.866E+01  Å
```

DATA REDUCTION PARAMETERS

Thermal Transpiration : ON
Effective Molecule Diameter (D) 3.5400 Å
Effective Cell Stem Inner Diameter (d) 4.0000 mm
Last Po Acquired 798.44 mm Hg
Additional Initialization Information Not Recorded.

BJH/DH Moving Average Size : 1

Interaction Constant (K) 2.9600 nm^3 x kJ/mol

Appendix Figure D4 BET analysis of LaCoO$_3$-ss (1:1, 900°C).

```
                        Quantachrome Corporation
          Quantachrome Autosorb Automated Gas Sorption System Report
                          Autosorb for Windows®

Sample ID          highCo 700
Description
Comments
Sample Weight      0.0728 g
Adsorbate          NITROGEN          Outgas Temp    300.0 °C   Operator       Rungrueng
Cross-Sec Area     16.2 Å²/molecule  Outgas Time    1.0 hrs    Analysis Time  60.0 min
NonIdeality        6.580E-05         P/Po Toler     2          End of Run     01/04/1980 00
Molecular Wt       28.0134 g/mol     Equil Time     3          File Name      AS830551.RAW
Station #          1                 Bath Temp.     77.35


                        AREA-VOLUME-PORE SIZE SUMMARY

                             SURFACE AREA DATA

        Multipoint BET................................................ 8.238E+00  m²/g
        Single Point BET............................................. 8.615E+00  m²/g
        Langmuir Surface Area........................................ 2.302E+01  m²/g
        t-Method External Surface Area............................... 8.238E+00  m²/g
        t-Method Micro Pore Surface Area............................. 0.000E+00  m²/g
        DR Method Micro Pore Area.................................... 8.919E+00  m²/g

                             PORE VOLUME DATA

        t-Method Micro Pore Volume................................... 0.000E+00  cc/g
        DR Method Micro Pore Volume................................. 3.170E-03  cc/g
        HK Method Cumulative Pore Volume........................... 2.434E-03  cc/g
        SF Method Cumulative Pore Volume........................... 2.563E-03  cc/g

                              PORE SIZE DATA

DR  Method Micro Pore Width    .............................. 1.467E+02  Å
DA  Method Pore Diameter (Mode)............................. 1.920E+01  Å
HK  Method Pore Width    (Mode)............................. 1.767E+01  Å
SF  Method Pore Diameter (Mode)............................. 3.359E+01  Å

                         DATA REDUCTION PARAMETERS

                      Thermal Transpiration : ON
                 Effective Molecule Diameter (D) 3.5400 Å
            Effective Cell Stem Inner Diameter (d) 4.0000 mm
                      Last Po Acquired 787.25 mm Hg
           Additional Initialization Information Not Recorded.

                       BJH/DH Moving Average Size : 1

              Interaction Constant (K) 2.9600 nm^3 x kJ/mol
```

Appendix Figure D5 BET analysis of LaCoO$_3$-ss (high Co, 700°C).

Quantachrome Corporation
Quantachrome Autosorb Automated Gas Sorption System Report
Autosorb for Windows®

Sample ID   High Co 800
Description
Comments
Sample Weight   0.2010 g
Adsorbate   NITROGEN   Outgas Temp   300.0 °C   Operator   Rungrueang
Cross-Sec Area   16.2 Å²/molecule   Outgas Time   1.0 hrs   Analysis Time 60.1 min
NonIdeality   6.580E-05   P/Po Toler   0   End of Run   09/25/2008 17
Molecular Wt   28.0134 g/mol   Equil Time   3   File Name   AS830565.RAW
Station #   1   Bath Temp.   77.35

AREA-VOLUME-PORE SIZE SUMMARY

SURFACE AREA DATA

Multipoint BET... 3.014E+00 m²/g
Single Point BET.. 2.772E+00 m²/g
Langmuir Surface Area... 5.303E+00 m²/g
t-Method External Surface Area................................ 3.014E+00 m²/g
t-Method Micro Pore Surface Area.............................. 0.000E+00 m²/g
DR Method Micro Pore Area..................................... 3.202E+00 m²/g

PORE VOLUME DATA

t-Method Micro Pore Volume.................................... 0.000E+00 cc/g
DR Method Micro Pore Volume................................... 1.138E-03 cc/g
HK Method Cumulative Pore Volume.............................. 9.430E-04 cc/g
SF Method Cumulative Pore Volume.............................. 9.809E-04 cc/g

PORE SIZE DATA

DR Method Micro Pore Width   .... 1.225E+02 Å
DA Method Pore Diameter (Mode).............................. 1.840E+01 Å
HK Method Pore Width   (Mode).............................. 1.712E+01 Å
SF Method Pore Diameter (Mode).............................. 3.248E+01 Å

DATA REDUCTION PARAMETERS

Thermal Transpiration : ON
Effective Molecule Diameter (D) 3.5400 Å
Effective Cell Stem Inner Diameter (d) 4.0000 mm
Last Po Acquired 793.02 mm Hg
Additional Initialization Information Not Recorded.

BJH/DH Moving Average Size : 1

Interaction Constant (K) 2.9600 nm^3 x kJ/mol

Appendix Figure D6 BET analysis of $LaCoO_3$-ss (high Co, $800^{\circ}C$).

Quantachrome Corporation
Quantachrome Autosorb Automated Gas Sorption System Report
Autosorb for Windows®

Sample ID   High Co 850
Description
Comments
Sample Weight   0.2240 g
Adsorbate   NITROGEN   Outgas Temp   300.0 °C   Operator   Rungrueang
Cross-Sec Area   16.2 Å²/molecule Outgas Time   1.0 hrs   Analysis Time   60.3 min
NonIdeality   6.580E-05   P/Po Toler   0   End of Run   09/26/2008 14
Molecular Wt   28.0134 g/mol   Equil Time   3   File Name   AS830566.RAW
Station #   1   Bath Temp.   77.35

AREA-VOLUME-PORE SIZE SUMMARY

SURFACE AREA DATA

Multipoint BET.. 3.980E+00 m²/g
Single Point BET... 3.144E+00 m²/g
Langmuir Surface Area.. 9.014E+00 m²/g
t-Method External Surface Area............................... 3.980E+00 m²/g
t-Method Micro Pore Surface Area............................. 0.000E+00 m²/g
DR Method Micro Pore Area.................................... 3.363E+00 m²/g

PORE VOLUME DATA

t-Method Micro Pore Volume................................... 0.000E+00 cc/g
DR Method Micro Pore Volume.................................. 1.195E-03 cc/g
HK Method Cumulative Pore Volume............................. 9.010E-04 cc/g
SF Method Cumulative Pore Volume............................. 9.490E-04 cc/g

PORE SIZE DATA

DR Method Micro Pore Width   .... 1.533E+02 Å
DA Method Pore Diameter (Mode).............................. 1.920E+01 Å
HK Method Pore Width   (Mode).............................. 1.783E+01 Å
SF Method Pore Diameter (Mode).............................. 3.396E+01 Å

DATA REDUCTION PARAMETERS

Thermal Transpiration : ON
Effective Molecule Diameter (D) 3.5400 Å
Effective Cell Stem Inner Diameter (d) 4.0000 mm
Last Po Acquired 787.73 mm Hg
Additional Initialization Information Not Recorded.

BJH/DH Moving Average Size : 1

Interaction Constant (K) 2.9600 nm^3 x kJ/mol

Appendix Figure D7 BET analysis of $LaCoO_3$-ss (high Co, 850°C).

```
                        Quantachrome Corporation
        Quantachrome Autosorb Automated Gas Sorption System Report
                        Autosorb for Windows®

Sample ID         High Co 900
Description
Comments
Sample Weight     0.3457 g
Adsorbate         NITROGEN          Outgas Temp   300.0 °C   Operator       Rungrueang
Cross-Sec Area    16.2 Å²/molecule  Outgas Time   1.0 hrs    Analysis Time  60.1 min
NonIdeality       6.580E-05         P/Po Toler    0          End of Run     09/26/2008 16
Molecular Wt      28.0134 g/mol     Equil Time    3          File Name      AS830567.RAW
Station #         1                 Bath Temp.    77.35


                      AREA-VOLUME-PORE SIZE SUMMARY

                           SURFACE AREA DATA

        Multipoint BET............................................. 1.741E+00  m²/g
        Single Point BET.......................................... 1.633E+00  m²/g
        Langmuir Surface Area..................................... 2.875E+00  m²/g
        t-Method External Surface Area............................ 1.741E+00  m²/g
        t-Method Micro Pore Surface Area.......................... 0.000E+00  m²/g
        DR Method Micro Pore Area................................. 2.121E+00  m²/g

                           PORE VOLUME DATA

        t-Method Micro Pore Volume................................ 0.000E+00  cc/g
        DR Method Micro Pore Volume............................... 7.538E-04  cc/g
        HK Method Cumulative Pore Volume.......................... 6.368E-04  cc/g
        SF Method Cumulative Pore Volume.......................... 6.586E-04  cc/g

                            PORE SIZE DATA

        DR  Method Micro Pore Width    ........................... 1.167E+02  Å
        DA  Method Pore Diameter (Mode)........................... 1.840E+01  Å
        HK  Method Pore Width    (Mode).......................... 1.723E+01  Å
        SF  Method Pore Diameter (Mode).......................... 3.276E+01  Å

                        DATA REDUCTION PARAMETERS

                        Thermal Transpiration : ON
                 Effective Molecule Diameter (D) 3.5400 Å
               Effective Cell Stem Inner Diameter (d) 4.0000 mm
                        Last Po Acquired 786.60 mm Hg
               Additional Initialization Information Not Recorded.

                        BJH/DH Moving Average Size : 1

               Interaction Constant (K) 2.9600 nm^3 x kJ/mol
```

Appendix Figure D8 BET analysis of LaCoO$_3$-ss (high Co, 900$°$C).

Quantachrome Corporation
Quantachrome Autosorb Automated Gas Sorption System Report
Autosorb for Windows®

Sample ID	high La 800					
Description						
Comments						
Sample Weight	0.0329 g					
Adsorbate	NITROGEN	Outgas Temp	300.0 °C	Operator	Rungrueng	
Cross-Sec Area	16.2 Å²/molecule	Outgas Time	1.0 hrs	Analysis Time	60.2 min	
NonIdeality	6.580E-05	P/Po Toler	2	End of Run	01/03/1980 00	
Molecular Wt	28.0134 g/mol	Equil Time	3	File Name	AS830545.RAW	
Station #	1	Bath Temp.	77.35			

AREA-VOLUME-PORE SIZE SUMMARY

SURFACE AREA DATA

Multipoint BET...	4.953E+00	m²/g
Single Point BET..	4.690E+00	m²/g
Langmuir Surface Area...	7.962E+00	m²/g
t-Method External Surface Area................................	4.841E+00	m²/g
t-Method Micro Pore Surface Area..............................	1.112E-01	m²/g
DR Method Micro Pore Area.....................................	6.604E+00	m²/g

PORE VOLUME DATA

t-Method Micro Pore Volume....................................	5.228E-05	cc/g
DR Method Micro Pore Volume...................................	2.347E-03	cc/g
HK Method Cumulative Pore Volume..............................	2.049E-03	cc/g
SF Method Cumulative Pore Volume..............................	2.099E-03	cc/g

PORE SIZE DATA

DR	Method Micro Pore Width	1.066E+02	Å
DA	Method Pore Diameter (Mode)............................	1.820E+01	Å
HK	Method Pore Width (Mode)..............................	1.767E+01	Å
SF	Method Pore Diameter (Mode)............................	3.368E+01	Å

DATA REDUCTION PARAMETERS

Thermal Transpiration : ON
Effective Molecule Diameter (D) 3.5400 Å
Effective Cell Stem Inner Diameter (d) 4.0000 mm
Last Po Acquired 786.33 mm Hg
Additional Initialization Information Not Recorded.

BJH/DH Moving Average Size : 1

Interaction Constant (K) 2.9600 nm^3 x kJ/mol

Appendix Figure D9 BET analysis of LaCoO$_3$-ss (high La, 800°C).

Quantachrome Corporation
Quantachrome Autosorb Automated Gas Sorption System Report
Autosorb for Windows®

Sample ID   high La 900
Description
Comments
Sample Weight   0.0620 g
Adsorbate   NITROGEN   Outgas Temp   300.0 °C   Operator   Rungrueng
Cross-Sec Area   16.2 Å²/molecule   Outgas Time   1.0 hrs   Analysis Time   58.2 min
NonIdeality   6.580E-05   P/Po Toler   2   End of Run   01/03/1980 00
Molecular Wt   28.0134 g/mol   Equil Time   3   File Name   AS830550.RAW
Station #   1   Bath Temp.   77.35

AREA-VOLUME-PORE SIZE SUMMARY

SURFACE AREA DATA

Multipoint BET... 4.457E+00 m²/g
Single Point BET.. 4.279E+00 m²/g
Langmuir Surface Area... 7.286E+00 m²/g
t-Method External Surface Area................................ 4.457E+00 m²/g
t-Method Micro Pore Surface Area............................. 0.000E+00 m²/g
DR Method Micro Pore Area.................................... 5.199E+00 m²/g

PORE VOLUME DATA

t-Method Micro Pore Volume................................... 0.000E+00 cc/g
DR Method Micro Pore Volume.................................. 1.848E-03 cc/g
HK Method Cumulative Pore Volume............................ 1.684E-03 cc/g
SF Method Cumulative Pore Volume............................ 1.697E-03 cc/g

PORE SIZE DATA

DR Method Micro Pore Width   .... 8.708E+01 Å
DA Method Pore Diameter (Mode)............................... 1.880E+01 Å
HK Method Pore Width   (Mode)............................... 1.777E+01 Å
SF Method Pore Diameter (Mode)............................... 3.386E+01 Å

DATA REDUCTION PARAMETERS

Thermal Transpiration : ON
Effective Molecule Diameter (D) 3.5400 Å
Effective Cell Stem Inner Diameter (d) 4.0000 mm
Last Po Acquired 783.10 mm Hg
Additional Initialization Information Not Recorded.

BJH/DH Moving Average Size : 1

Interaction Constant (K) 2.9600 nm^3 x kJ/mol

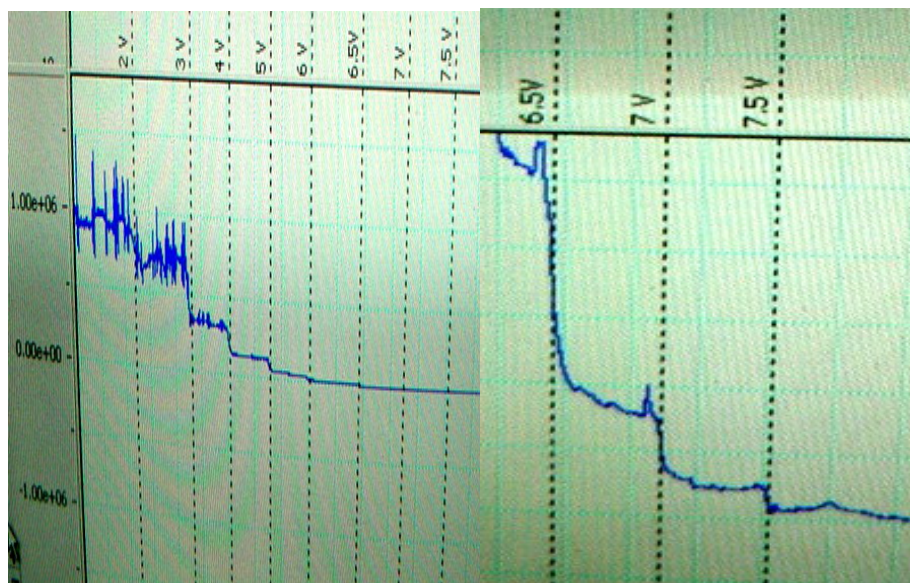**Appendix Figure D10** BET analysis of LaCoO$_3$-ss (high La, 900°C).

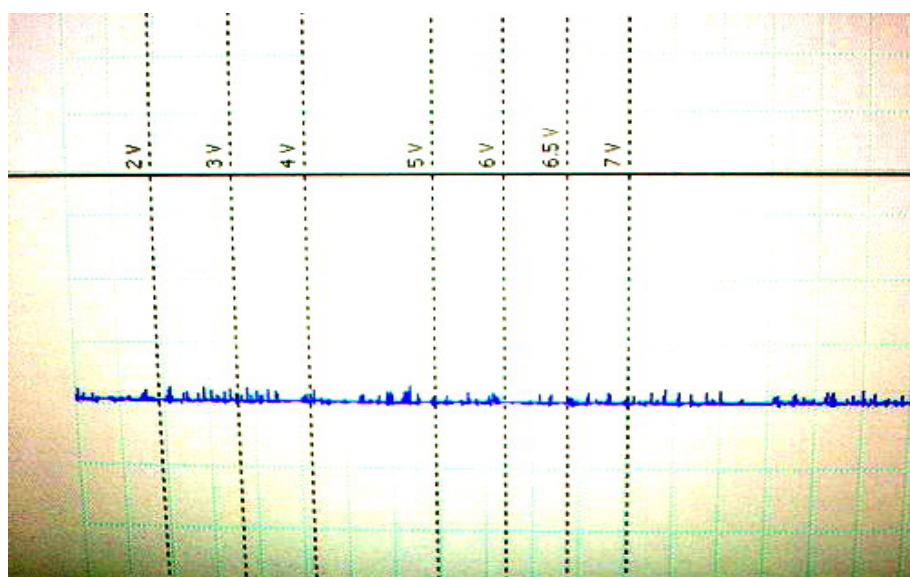**Appendix E**

The resistance from e-corder
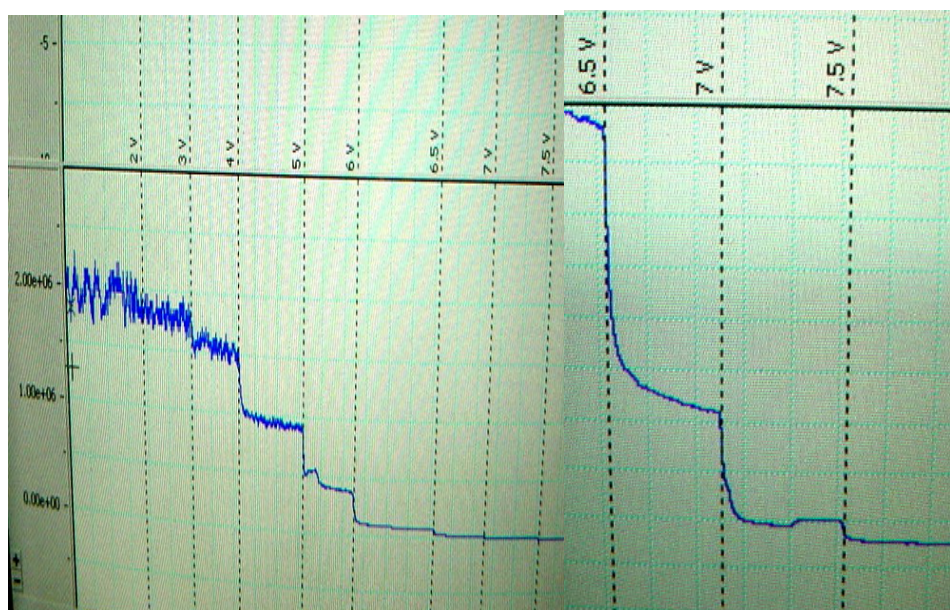
Appendix Figure E1 The LaCoO$_3$-ss (1:1 and high Co) resistance from e-corder.
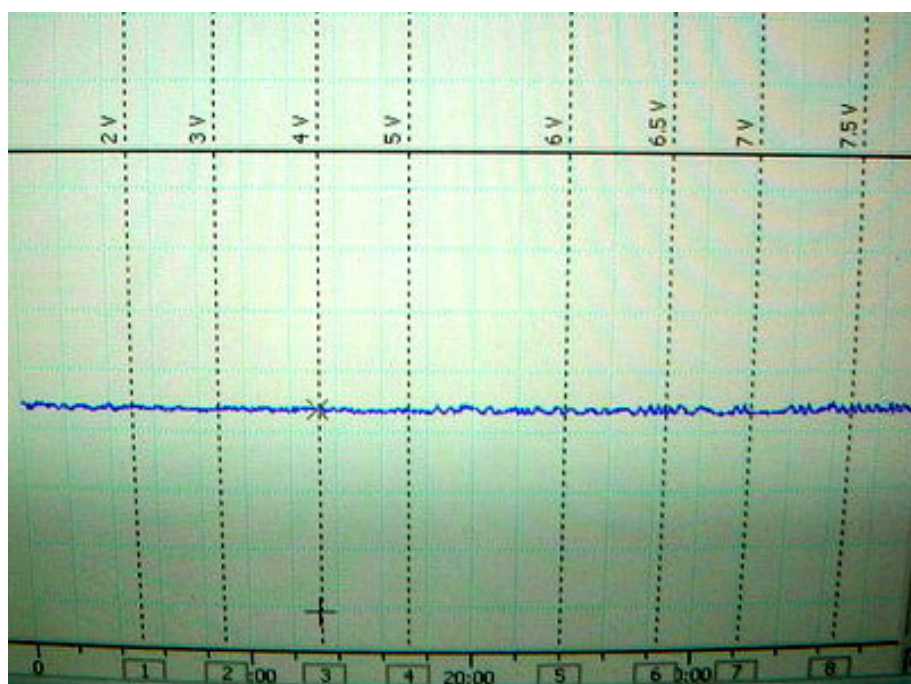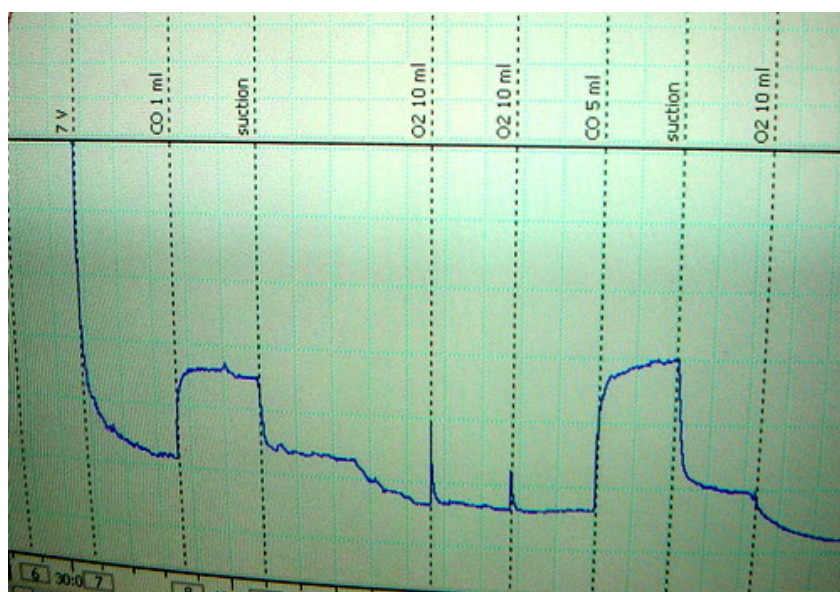

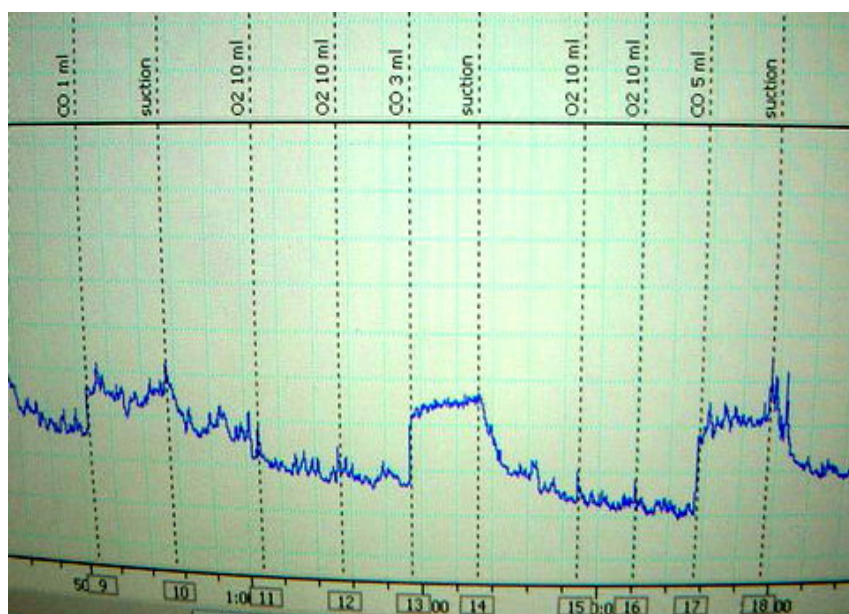**Appendix Figure E2** The LaCoO$_3$-ss (high La) resistance from e-corder**.**

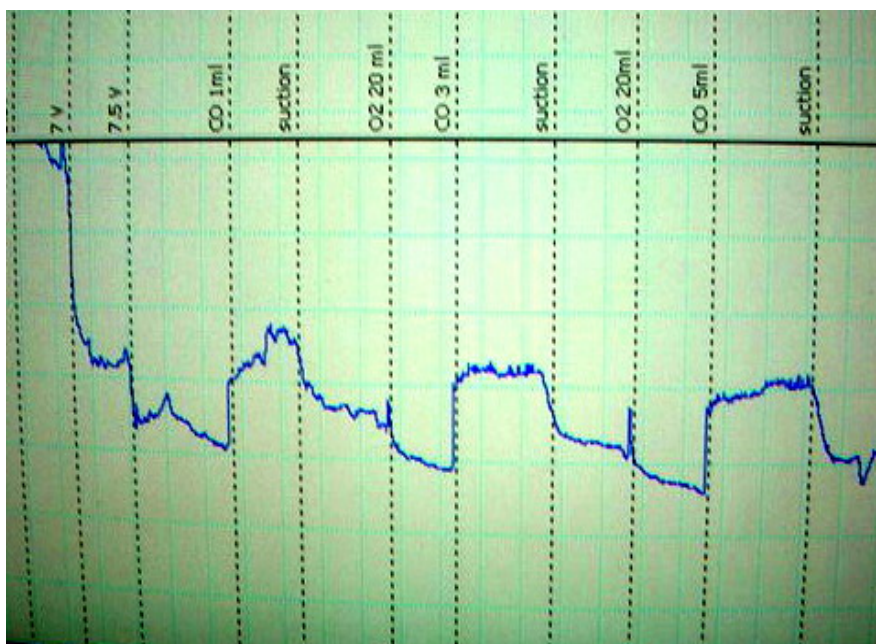**Appendix Figure E3** The LaCoO$_3$-cp resistance from e-corder.

Appendix Figure E4 The LaCoO$_3$-wd resistance from e-corder.

Appendix Figure E5 The LaCoO$_3$-ss (1:1) resistance for CO sensor from e-corder.

Appendix Figure E6 The LaCoO$_3$-ss (high Co) resistance for CO sensor from
e-corder.

Appendix Figure E7 The LaCoO$_3$-cp resistance for CO sensor from e-corder.

Appendix F

The calculation of LaCoO$_3$-ss preparation

1. The calculation of $LaCoO_3$-ss (1:1) preparation

La   M.W = 138.91 g

Co   M.W = 58.93   g

O   M.W = 15.99 g

$LaCoO_3$ M.W = 245.84 g = 1 mole

Amount of mole 1:1 $LaCoO_3$ onto 20 g $= \dfrac{1mole \times 20g}{245.84g}$

          $=$ 0.0813 mole

La_2O_3 M.W = 325.82 g

Amount of gram La_2O_3 onto 0.0813 mole $= \dfrac{325.82g \times 0.08132mole}{2}$

          $=$ 13.2478 g

Co_3O_4 M.W = 240.78 g

Amount of gram Co_3O_4 onto 0.0813 mole $= \dfrac{240.78g \times 0.08132mole}{3}$

          $=$ 6.5267 g

2. The calculation of $LaCoO_3$-ss (1:5 high Co) preparation

La   M.W = 138.91 g

Co   M.W = 58.93 g

O   M.W = 15.99 g

$La_{0.2}CoO_3$ M.W = 134.66 g = 1 mole

Amount of mole $LaCoO_3$-ss (high Co) onto 20 g   = $\dfrac{1 mole \times 20 g}{134.66 g}$

                                                  =   0.1485 mole

La_2O_3 M.W = 325.82 g

Amount of gram La_2O_3 onto 0.1485 mole   = $\dfrac{325.82 g \times 0.1485 mole}{2}$

                                             =   24.1953 g

Co_3O_4 M.W = 240.78 g

Amount of gram Co_3O_4 onto 0.1485 mole   = $\dfrac{240.78 g \times 0.1485 mole}{3}$

                                             =   11.9186 g

3. The calculation of $LaCoO_3$-ss (5:1 high La) preparation

La   M.W = 138.91 g

Co   M.W = 58.93 g

O   M.W = 15.99 g

$LaCo_{0.2}O_3$ M.W = 198.66 g = 1 mole

Amount of mole $LaCoO_3$(high La) onto 20 g $=$ $\dfrac{1\,mole \times 20\,g}{198.66\,g}$

                  $=$ 0.1006 mole

La_2O_3 M.W = 325.82 g

Amount of gram La_2O_3 onto 0.1006 mole $=$ $\dfrac{325.82\,g \times 0.1006\,mole}{2}$

                  $=$ 16.4007 g

Co_3O_4 M.W = 240.78 g

Amount of gram Co_3O_4 onto 0.1006 mole $=$ $\dfrac{240.78\,g \times 0.1006\,mole}{3}$

                  $=$ 8.0741 g

Appendix G

The calculation of the carbon monoxide (CO)

1. The calculation of the carbon monoxide (CO) percentage.

   The percentage of the carbon monoxide was calculated by using Equation 1.

$$C_1V_1 = C_2V_2 \qquad\qquad \text{Equation 1}$$

$$C_2 = \frac{C_1V_1}{V_2}$$

Where C_1 is the concentration of the carbon monoxide in stock (%).

V₁ is volume of the carbon monoxide inject in the flask (ml).

V_1 is volume of the carbon monoxide inject in the flask (ml).

V_2 is volume in the flask 50 ml.

C_2 is the concentration of the carbon monoxide in the flask 50 ml (%).

Example   Stock CO 99.2%

$$C_2 = \frac{(99.2\%)\ (CO\ 1ml)}{(50ml)}$$

$$C_2 = 1.98\%$$

2. The calculation of the carbon monoxide (CO) ppm

   Stock CO 99.2% by volume

$$ppm = \frac{\mu L}{L} = \frac{10^{-6}L}{L} \qquad\qquad \text{Equation 2}$$

$$\frac{\mu L}{L} = \frac{99.2ml}{100ml} \times \frac{1000ml}{1L} \times \frac{1000\mu L}{1ml}$$

$$\frac{\mu L}{L} = 99.2 \times 10^4 \frac{\mu L}{L}$$

$$ppm = 99.2 \times 10^4 \frac{\mu L}{L}$$

CIRRICULUM VITAE

NAME	:	Ms. Saengdoen Daungdaw
BIRTH DATE	:	August 20, 1970
BIRTH PLACE	:	Phare, Thailand

EDUCATION : **YEAR INSITUTION   DEGREE/DIPLOMA**

1994 Ramkhamhaeng Univ.   B.S. (Chemistry)

POSITION : Researcher 7

WORK PLACE : Material Innovation Department,
Thailand Institute of Scientific
and Technological Research (TISTR)

SCHOLARSHIP : Research assistantship from Kasetsart University
Research and Development Institute
: Research assistantship from Thailand Institute of
Scientific and Technological Research (TISTR)